◢ESARDA

The International Journal of Nuclear Safeguards and Non-Proliferation

ESARDA is an association formed to advance and harmonize research and development for safeguards. More information can be found at the following address:

https://esarda.jrc.ec.europa.eu/

Papers submitted for publication are reviewed by independent authors including members of the Editorial Board.

Manuscripts have to be sent to the Editor (EC-ESARDA-BULLETIN@ec.europa.eu) following the paper guidelines available in the ESARDA Bulletin section of the ESARDA website (https://esarda.jrc.ec.europa.eu/) where the bulletins can also be viewed and downloaded.

Accepted manuscripts are published free of charge.

N.B. Articles and other material in the ESARDA Bulletin do not necessarily present the views or policies of neither ESARDA nor the European Commission.

ESARDA Bulletin is published jointly by ESARDA and the Joint Research Centre of the European Commission and distributed free of charge to over 700 registered members, libraries and institutions Worldwide.

The publication is authorized by ESARDA.

Cover designed by Christopher Craig Havenga, (EC, JRC, G.II.7, Italy)

Printed by
IMPRIMERIE CENTRALE, Luxembourg

ESARDA
European Safeguards Research and Development Association

Bulletin

Contents Issue n° 60

Editorial
Elena Stringa

Dear readers,

I hope that this issue of the ESARDA Bulletin finds you well.

During the last months we were suddenly forced to change our daily routines due to the dramatic expansion of the Covid-19 virus and all of us had to revise the way of working and living to adapt to the new situation. Access to laboratories and facilities have been limited for many of us, making the preparation of research articles more challenging.

The 42th ESARDA annual meeting planned for May 2020 has been postponed because of the crisis, but the latest news from the ESARDA working groups and about relevant past and future events can be found in the Connector newsletter n. 2, that is being published when I'm writing this editorial. I am inviting you to read our newsletter and if you have news or technical contribution that you would like to have published in the next ESARDA Connector, please send an e-mail to EC-ESARDA-CONNECTOR@ec.europa.eu.

I am very proud to present to you Issue 60 of the ESARDA Bulletin that has been released regularly despite the adverse situation. The publication of the journal has been made possible thanks to the dedication of authors and reviewers, who dedicated part of their time in writing and reviewing contributions allowing the ESARDA Community to benefit of the latest research developments in the field of Nuclear Safeguards. Thank you very much for your dedication.

Should you have an academic contribution that you want to submit to the ESARDA Bulletin, please send it to EC-ESARDA-BULLETIN@ec.europa.eu together with the signed paper submission form that you can find in the ESARDA Bulletin web page (from https://esarda.jrc.ec.europa.eu/ click the tab 'Publications' and then select 'Bulletin' from the menu).

Thanks also to Christopher Havenga who designed and realized the cover of the last ESARDA Bulletin issues with great enthusiasm.

Last but not least, special thanks to Andrea De Luca, the ESARDA publication assistant editor: his support together with ideas for improvements are always very appreciated. Andrea, thank you so much!

I wish you a pleasant reading.

Dr. Elena Stringa
Editor of the ESARDA Bulletin - The International Journal
of Nuclear Safeguards and Non-proliferation
https://esarda.jrc.ec.europa.eu/
EC-ESARDA-BULLETIN@ec.europa.eu
Elena.Stringa@.ec.europa.eu

Performance of FRAM isotopic analysis of shielded plutonium with an electrically cooled coaxial gamma-spectrometer

Jozsef Zsigrai[1], Andrey Berlizov[2], Darcy van Eerten[1,3], Janos Bagi[1], Artur Muehleisen[1]

[1]European Commission, Joint Research Centre, Directorate G, Karlsruhe, Germany
[2]International Atomic Energy Agency, Vienna, Austria
[3]Durham University, Durham, United Kingdom

Abstract:

The capability of the FRAM software to accurately determine the isotopic composition of shielded plutonium was tested by the Joint Research Centre in Karlsruhe to support the use of FRAM for the verification of plutonium-bearing items by safeguards inspectors in the field. More than ten thousand spectra of eight certified reference-material items were analysed using different FRAM parameter sets. The spectra were recorded by the "ORTEC microDetective" portable electrically cooled coaxial gamma spectrometer. The performance of FRAM was evaluated as a function of shielding thickness, measurement time, sample composition and "spectrum quality". The spectrum quality was quantified using a numerical figure of merit that included the uncertainties of the peak areas relevant for the isotopic analysis. Thereby, it combined the effects of shielding, measurement time and sample isotopic composition into a single indicator. It was confirmed that using FRAM's automatic analysis option improves the isotopic results, especially in the case of lower quality spectra. The results of this work will help safeguards inspectors to optimize the use of electrically cooled gamma-spectrometers and to improve the accuracy of plutonium isotopic composition measurements in the field.

Keywords: gamma spectrometry, electrically cooled gamma spectrometer, plutonium isotopic composition, FRAM

1. Introduction

The purpose of this work was to study and possibly improve the capability of the FRAM software to determine the isotopic composition of shielded plutonium by portable electrically cooled HPGe detectors. This work, focused on plutonium, is a follow-up of previous work [1] that was focused on uranium. Both tasks were carried out within the European Commission's support programme to the International Atomic Energy Agency (IAEA). For the sake of completeness, some introductory remarks about the task and about FRAM are repeated here.

FRAM is software that calculates uranium and plutonium isotopic composition from the gamma spectra of these materials [2], [3]. It has been developed at Los Alamos

National Laboratory (USA) and it has been commercialized by ORTEC and Canberra. The version used in this study was 5.2, which has minor changes compared to version 5.1 [4], which was used in the study on uranium [1].

The so-called parameter sets determine what FRAM exactly does. They define the type of material (U, Pu, MOX) and the type of detector. They also contain information about the isotopes and gamma peaks to be analysed, peak fitting parameters, energy calibration, relative efficiency constraints, etc. FRAM contains a number of default parameter sets built into the software, which cover a large number of typical measurement configurations. However, users can also prepare modified or new parameter sets to suit their specific measurement configuration. In this work we focused on parameter sets for plutonium.

More than 7000 high-resolution gamma spectra of various certified reference materials were taken by the ORTEC microDetective electrically cooled spectrometer under well-defined measurement conditions with different steel, cadmium and lead screens. These spectra were used to check the performance of FRAM v5.2 for determining the isotopic composition of shielded plutonium. In this paper the results calculated using different parameter sets are compared to each other and the influence of shielding thickness, measurement time and plutonium burn-up is discussed. This way the capabilities and limitations of FRAM became better understood.

2. Method and equipment

The ORTEC microDetective electrically cooled spectrometer [5] was used to record the gamma spectra. It has a high-purity coaxial germanium (HPGe) crystal of 50 mm diameter and 30 mm depth (length). The conversion gain of its amplifier was set to 0.125 keV/channel, to match the gain in the default FRAM parameter sets. The amplifier rise time was set to 3.4 µs, and flattop to 0.8 µs. (Note that for the uranium study [1] an older version of the ORTEC detective was used, having fixed settings, set in the factory.) The measured peak resolution (full with at half-maximum) was approximately 1.5 keV at 122 keV and 2.0 keV at 1001 keV.

A total of 8 Pu reference items from the "CBNM" [6] and "PI-DIE" [7], [8], [9] sets were used in this study. Their isotopic

Reference sample		Isotope					
		[238]Pu	[239]Pu	[240]Pu	[241]Pu	[242]Pu	[241]Am
CBNM Pu93	weight %	0.0117	93.4123	6.3131	0.2235	0.0395	0.1047
	2s	0.00003	0.004	0.0039	0.0004	0.0003	0.0021
CBNM Pu84	weight %	0.0703	84.3377	14.2069	1.0275	0.3576	0.2173
	2s	0.0006	0.0084	0.0085	0.0018	0.001	0.0022
CBNM Pu70	weight %	0.8458	73.3191	18.2945	5.4634	2.0772	1.1705
	2s	0.0018	0.0098	0.0087	0.0034	0.0023	0.0117
CBNM Pu61	weight %	1.1969	62.5255	25.4058	6.6793	4.1925	1.4452
	2s	0.0025	0.0283	0.0241	0.0087	0.0064	0.0144

Table 1: Isotopic composition of the "CBNM" reference samples in weight % with 2s absolute uncertainty for reference date 20.6.1986.

Reference sample		Isotope					
		[238]Pu	[239]Pu	[240]Pu	[241]Pu	[242]Pu	[241]Am
PIDIE 1	weight %	0.01101	93.7650	5.99025	0.19920	0.0346	0.2304
	2s	0.00033	0.0065	0.0052	0.00255	0.0015	0.0060
PIDIE 3	weight %	0.04716	84.5795	14.1442	0.9953	0.2338	0.6282
	2s	0.00038	0.0094	0.0052	0.0036	0.0075	0.0151
PIDIE 5	weight %	0.1314	75.8862	21.2169	2.0638	0.7017	1.7488
	2s	0.0011	0.0147	0.0115	0.0042	0.0015	0.0387
PIDIE 7	weight %	1.253	61.9848	25.5941	6.4919	4.6763	3.5287
	2s	0.016	0.0420	0.0195	0.0132	0.0081	0.1111

Table 2: Isotopic composition of PIDIE reference samples in weight % (normalized to sum of Pu isotopes) with 2s absolute uncertainty for reference date 1.1.1988.
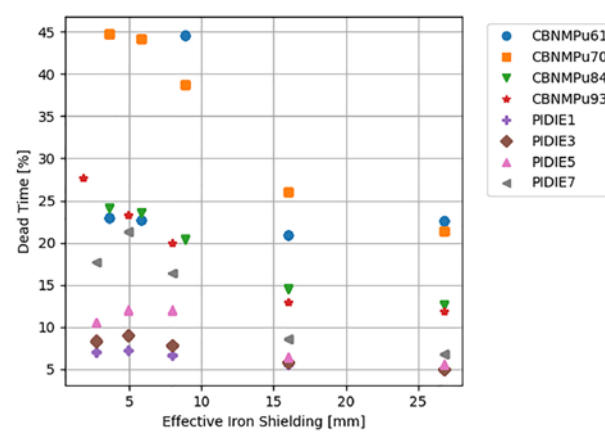
composition is shown in Table 1 and Table 2. The CBNM set consists of four sintered plutonium oxide pellets encased in stainless steel and protected by a plastic cap. Each pellet in the CBNM set contains 6.65±0.06 g of PuO_2. The items in the PIDIE set contain ca. 0.425g Pu in the form of a pressed PuO_2 pellet in a welded steel container.

The spectra of each item were recorded using a tungsten collimator and combinations of Fe screens of up to 16 mm thickness, Cd screens up to 2 mm thickness and a Pb screen of 4 mm thickness. This means 5 shielding configurations for each sample (Table 3). The sample to detector distance was 10 cm. There were two exceptions measured at 20 cm. These were the configurations with the CBNM Pu61 source and low shielding (2 mm Cd with no Fe and 1 mm Cd with 4 mm Fe). These two configurations could not be measured at 10cm because the count rate was too high and it saturated the spectrometer.

CBNM				PIDIE			
Fe	Cd	Pb	Effective Fe	Fe	Cd	Pb	Effective Fe
0	2	0	4	0	1.5	0	3
4	1	0	6	4	0.5	0	5
8	0.5	0	9	8	0	0	8
16	0	0	16	16	0	0	16
0	0	4	27	0	0	4	27

Table 3: Shielding thicknesses in mm. ("Effective Fe" is defined below.)

In Figure 1 the dependence of the dead time on the effective iron shielding thickness is shown for each sample. The total count rate ranged from about 200 cps (e.g. for PIDIE1 with 4 mm Pb) to about 6000 (e.g. for CBNM 61 with 2 mm Cd).

Figure 1: Dead time as a function of effective iron shielding. The two first points for CBNMPu61 have lower dead time than the third point in this series, because they were measured at a 20 cm distance, instead of 10 cm, to avoid saturating the detector.

In each of the 5 shielding configurations, for each sample 192 spectra of 5 minutes real time were recorded (that is 5x8x192=7680 spectra). Sum spectra of 15 minutes, 90 minutes, 2 hours, 4 hours, 6 hours and 16 hours real

time were prepared from the 5-minute spectra. This gives a total of 11240 spectra, distributed into 7 sets according to their real time.

The spectra within each set are independent from each other. The sets are not independent from each other, because each set was prepared from the same base set of 5-minute spectra. Therefore, comparing FRAM results obtained with different sets shows the dependence of the results on the measurement time, without interference of other factors.

All spectra were analysed with 3 parameter sets, with and without the "autoanalysis" option:

- Pu_Cx_120-460, no autoanalysis
- Pu_Cx_180-1010, no autoanalysis
- Pu_Cx_120-460, with autoanalysis
- Pu_Cx_180-1010, with autoanalysis
- det_coax_120_800_1_ecgs, no autoanalysis

The parameter sets Pu_Cx_120-460 and Pu_Cx_180-1010 are defaults in FRAM v5.2, while det_coax_120_800_1_ecgs

was provided to us by the IAEA. For the parameter set det_coax_120_800_1_ecgs the auto analysis option is not applicable. The numbers in the names of the parameter sets indicate the energy range in keV used in the analysis. With the auto analysis option the analysis is repeated with another parameter set if during the first analysis certain criteria are met (e.g. ratio of selected peaks). This makes it possible, for example, to automatically reanalyse spectra of shielded samples with a parameter set that uses the higher energy range.

Scripts written in the Python 3.6 programming language were used for

- adding the spectra,
- running FRAM on 11240 spectra with different parameter sets,
- extracting the results of interest from the FRAM result files,
- calculating performance indicators, such as relative bias, "MARD" and "CBD", defined below,
- visualizing the performance of FRAM through the use of various graphs. The FRAM results plotter received a graphical user interface shown in Figure 2.
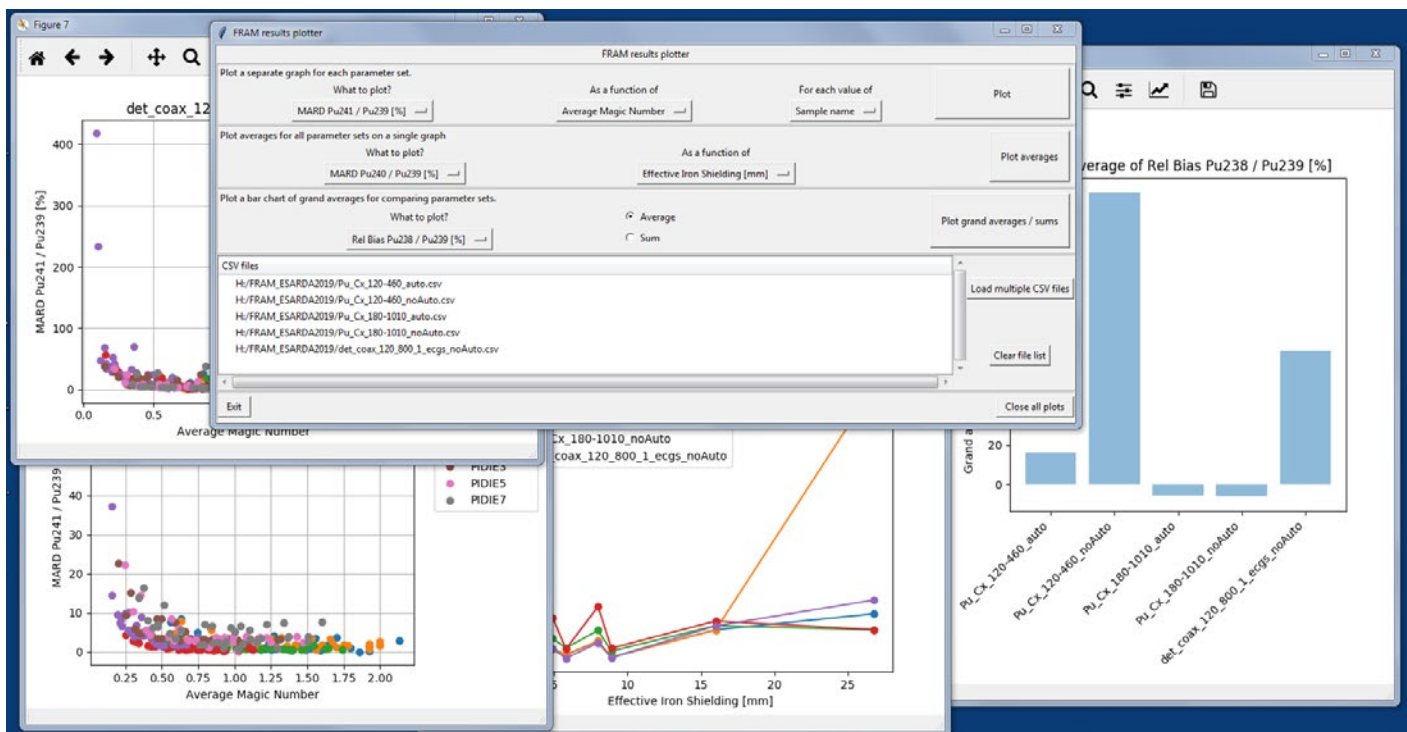

Figure 2: Screenshot of the FRAM results plotter

Several quantities were calculated for the statistical interpretation of the results.

- Average relative bias (ARB):
  - o The systematic component of FRAM's bias, or the expected accuracy of many (*n*) measurements. It can be either positive or negative.

- Relative standard deviation (RSD):
  - o The random component of FRAM's bias.

- Combined average relative bias and relative standard deviation (CBD):
  - o The overall performance of FRAM, or the expected accuracy of a single measurement.

- Mean absolute value of the relative difference (MARD):
  - o Similar to, but different from CBD. It also describes overall performance of FRAM, or the expected accuracy of a single measurement, but using it in error propagation is not straightforward. Here it is only used for comparison with previous work on uranium [1].

All these quantities are calculated for each sample, for each shielding configuration for each measurement time. They are defined as follows:

$$Average\ Relative\ Bias = ARB = \frac{\sum_{i=1}^{n} \frac{x_i - x_{Ref}}{x_{Ref}}}{n},$$

$$Relative\ Standard\ Deviation =$$

$$= RSD = \frac{1}{x_{Avg}} \sqrt{\frac{\sum_{i=1}^{n} \left(x_i - x_{Avg} \right)^2}{n-1}},$$

$$Combined\ Bias\ and\ standard\ Deviation =$$

$$= CBD = \sqrt{ARB^2 + RSD^2},$$

$$Mean\ Absolute\ value\ of\ Relative$$

$$Difference = MARD = \frac{\sum_{i=1}^{n} \frac{|x_i - x_{Ref}|}{x_{Ref}}}{n}, \quad (1)$$

where *n* is the number of spectra analysed (e.g. *n*=192 for the 5-minute spectra), x_i is the value calculated by FRAM, x_{Ref} is the certified reference value and x_{Avg} is the average of the FRAM results for the given measurement time and

shielding configuration. For the 16 h spectra n=1, so RSD is not calculated for the 16 h spectra.

In this work all isotopic data (declared data and FRAM results) were decay-corrected to 1st January 2019 and all quantities were calculated for this reference date.

Two especially important variables used for plotting were the effective iron shielding and the statistical quality indicator of the spectra. The effective iron shielding is the equivalent shielding based on thickness of the shielding screens used and the mean values of the linear attenuation coefficients in the energy range 180-433 keV. It is calculated as:

$$Effective\ iron\ shielding = d_{Fe} + \frac{\overline{\mu}_{Cd}}{\overline{\mu}_{Fe}} d_{Cd} + + \frac{\overline{\mu}_{Pb}}{\overline{\mu}_{Fe}} d_{Pb}, \quad (2)$$

where d_x, is the thickness of the Fe, Cd or Pb screens used and $\overline{x}_x$ is the average of 14 equidistant values of the linear attenuation coefficient of these materials in the energy range 180-433 keV. The values for linear attenuation coefficients were taken from the online NIST database [10].

For example, 4 mm of Pb corresponds to 26.8 mm effective iron shielding, while 2 mm of Cd corresponds to 3.6 mm effective iron shielding, according to the above definition.

The indicator of the statistical quality of the spectra ("magic number") is the inverse of the combined relative uncertainty of the "magic peaks":

$$statistical\ indicator\ \left("magic\ number" \right) = \frac{1}{\sqrt{\sum_i \delta_i^2}}, \quad (3)$$

where δ_i is the relative uncertainty of the ith peak and the sum goes over all magic peaks. The "magic peaks" are those peaks which are used in all parameter sets investigated in this study. In particular, they were the peaks of ^{239}Pu, ^{241}Pu and ^{241}Am at 413.712, 208.000 and 335.432 keV, respectively.

The statistical indicator depends on the following:

- measurement time,
- shielding,
- sample activity
- and isotopic composition.

Figure 3 shows the dependence of the statistical indicator (averaged over all shieldings and samples) on the measurement time, for all investigated parameter sets.
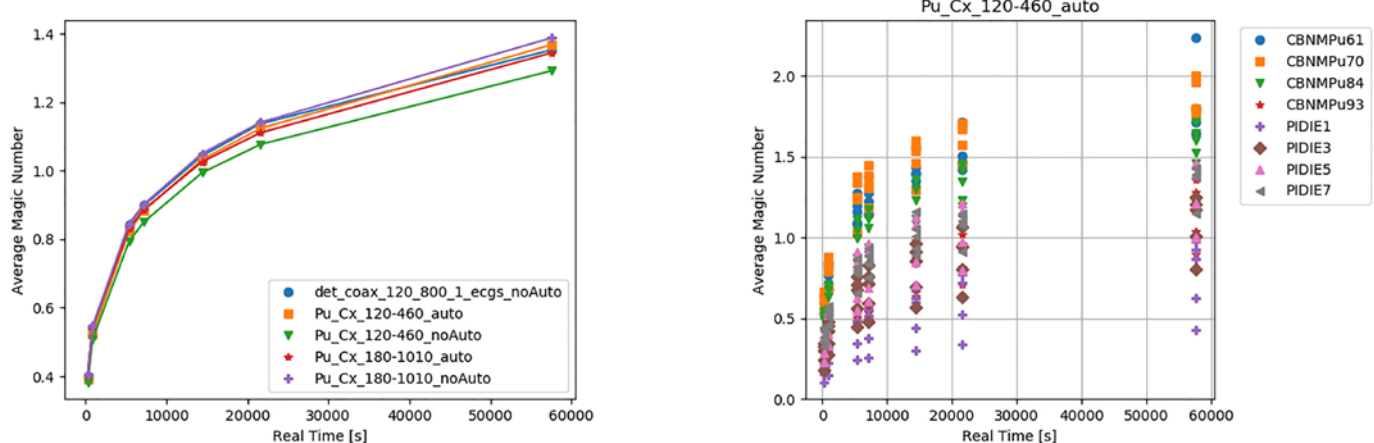
Figure 3: Left: statistical quality of the spectra ("magic number") averaged over all shieldings and samples as a function of real measurement time, for all investigated parameter sets. Right: statistical quality of the spectra ("magic number") as a function of real measurement time for all samples calculated using the parameter set Pu_Cx_120-460 with auto analysis turned on.

The statistical indicator also slightly depends on the parameter set, due to small differences in peak fitting. It increases with measurement time, but for some samples (e.g. PIDIE1, which has low activity) its stays quite low even for long measurement times, especially in the case of thick shielding. As it will be seen later, "good" spectrum quality means that the value of this indicator is around 1 or above 1. Note that, although the isotopic composition of, e.g., CBNMPu61 and PIDIE7 is very similar, their activity is very different. Therefore, their statistical indicators are very different.

Three different types of plots were prepared from the calculated statistical quantitates:

1. *"Category plots":* The performance indicators (average relative bias, RSD, CBD and MARD) of the isotope ratios relative to ^{239}Pu and of the ^{239}Pu isotope fraction were calculated for each configuration, each measurement time, each sample and each parameter set. These values were plotted as a function of various variables for all values of a selected category on a separate graph for each parameter set. For example, the dependence of ^{239}Pu CBD on spectrum quality for each value of the declared ^{239}Pu fraction is plotted on a separate graph for a given parameter set (Figure 14). This gives (5 configurations) x (7 different measurement times) x (8 samples) = 280 points on each "category plot".

2. *"Average plots"*: To visualize FRAM's performance in a more compact form, the average of the above quantities was calculated as a function of selected variables and all parameter sets were plotted on the same graph. For example, the ^{239}Pu average CBD as a function of statistical quality of the spectra (Figure 13) plotted on the same graph for all parameter sets. In this case the number of points on the graph depends on the number of different values that the independent parameter may take.

3. *"Grand average plots" (bar charts)*: To have an even more compact comparison of the parameter sets, the grand averages of all the values of selected quantities calculated by a given parameter set were plotted on a bar chart. An example is the bar chart showing the grand average of the ^{241}Pu CBD for all parameter sets (Figure 6).

These plots demonstrate the performance of the different FRAM parameter sets for different situations and might be used for improving the parameter sets.

3. Results

3.1 General comments on the results

The presentation of the results starts by comparing the parameter sets using the grand average plots for each investigated quantity, and then goes into more detail using the average plots. There is no separate section for category plots, but category plots are present in Figure 14 and Figure 16, to better illustrate some conclusions from the average plots.

The results for ^{242}Pu were not investigated in this work, because ^{242}Pu cannot be directly obtained from the gamma spectrum and empirical correlations have to be used. The discussion of these empirical correlations will be the subject of further work. That is why only isotope ratios to ^{239}Pu are studied in this work, and not the ratios to total Pu, because the ratios to total Pu are affected by the calculation of ^{242}Pu. Nevertheless, due to its importance for safeguards, the ratio of ^{239}Pu to total Pu is also presented in this work. The ^{239}Pu results obtained in two different ways are shown: using the default ^{242}Pu correlation in the FRAM parameter set, and also by using the declared ^{242}Pu content.
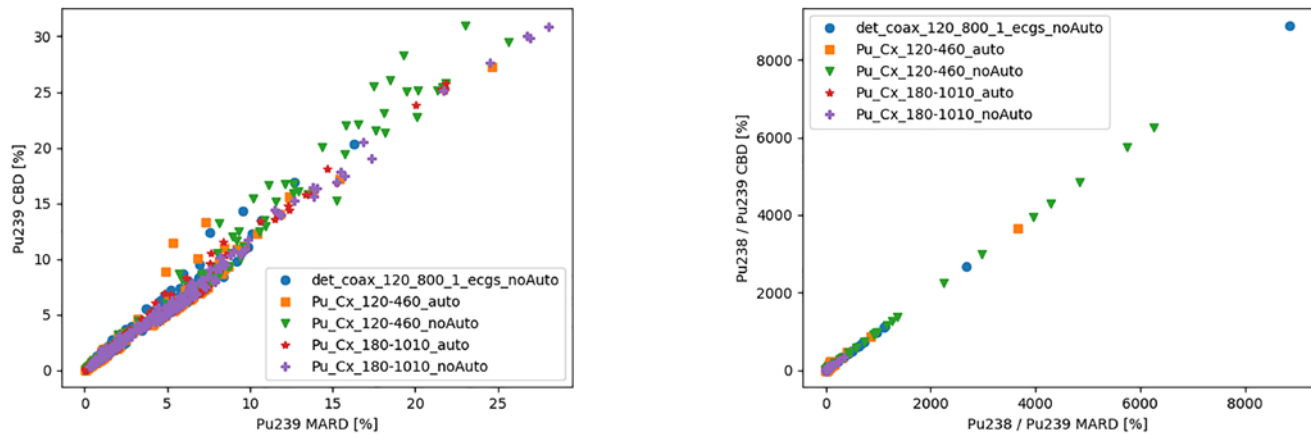
**Figure 4:** The CBD as a function of MARD for ^{239}Pu (left) and for the ^{238}Pu/^{239}Pu ratio right, for all investigates parameter sets.
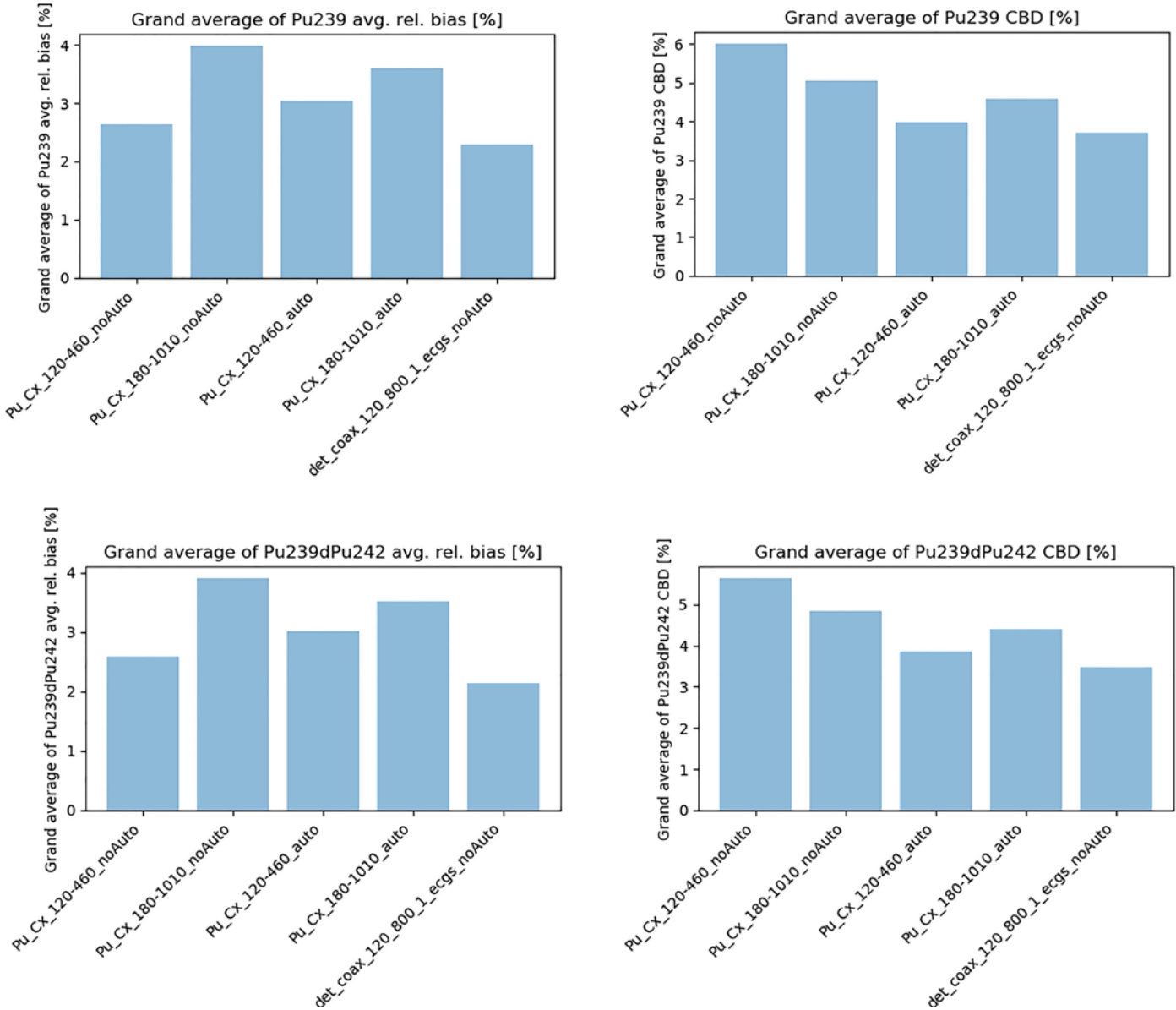
**Figure 5:** The grand average of ^{239}Pu/Pu mass fraction relative bias and CBD for all parameter sets, The upper plots show the results using the algorithm for ^{242}Pu calculation built in into the parameter sets, while the lower plots show the results using the (decay-corrected) declared ^{242}Pu.

In certain situations FRAM reports zero for some isotope ratios. Those results are removed from the averages presented in the graphs.

As the MARD used in previous work is no longer used here for the presentation of the results, it is worth to compare it to the CBD, which is used instead of it. The MARD and the CBD are mathematically NOT equivalent, but if all the biases are positive, then for large n (number of spectra) the values of the MARD and CBD are very close to each other. This is demonstrated in Figure 4, where the CBD for ^{239}Pu and for the ^{238}Pu/^{239}Pu ratio are plotted as a function of MARD.

3.2 Overall FRAM performance

To investigate overall FRAM performance, the grand average plots are best suited. They are supplemented with some average plots to explain in more detail the conclusions drawn from the grand average plots.

For the ^{239}Pu fraction the lowest grand average bias and the lowest grand average CBD are achieved using the parameter set det_coax_120_800_1_ecgs (Figure 5). This is true regardless of whether the built-in ^{242}Pu correlation or the declared ^{242}Pu values are used in the calculation. For mass ratios the best results are achieved with the two default parameter sets used in "autoanalysis" mode, and not with the det_coax_120_800_1_ecgs (Figure 6). These two observations seem to contradict each other. To resolve this seeming contradiction one has to notice two things:

- The ^{239}Pu biases with the parameter set det_coax_120_800_1_ecgs are both positive and negative, while with the default parameter sets they are mostly positive (except a few points) as seen on Figure 7. This way the individual ^{239}Pu biases for det_coax_120_800_1_ecgs cancel out, while for the other parameter set they do not, so the grand average is the lowest for det_coax_120_800_1_ecgs.

- From Figure 7 one can also see that the ^{239}Pu bias is correlated to the ^{240}Pu/^{239}Pu bias. For other mass ratios there is no such evident correlation. This is understandable, as ^{240}Pu is the second most abundant isotope after ^{239}Pu in all samples. This means that parameter sets which have lower absolute bias for ^{240}Pu/^{239}Pu will also have lower bias for ^{239}Pu. The correlation between the ^{239}Pu bias and ^{240}Pu/^{239}Pu bias is not linear: even a small negative bias of ^{240}Pu/^{239}Pu leads to a high ^{239}Pu bias, while relatively large positive ^{240}Pu/^{239}Pu biases lead to relatively low ^{239}Pu biases. For the parameter set det_coax_120_800_1_ecgs the ^{240}Pu/^{239}Pu biases are mostly positive, leading to small ^{239}Pu bias.

Therefore, the above points explain why from all investigated parameter sets the set det_coax_120_800_1_ecgs gives the lowest bias for the ^{239}Pu fraction, despite not giving the best results for the isotope ratios.

The above points also show that, to improve the results for ^{239}Pu, one should concentrate on improving the results for ^{240}Pu/^{239}Pu.

The grand average relative bias and CBD of the mass ratios relative to ^{239}Pu are shown for all parameter sets in Figure 6.
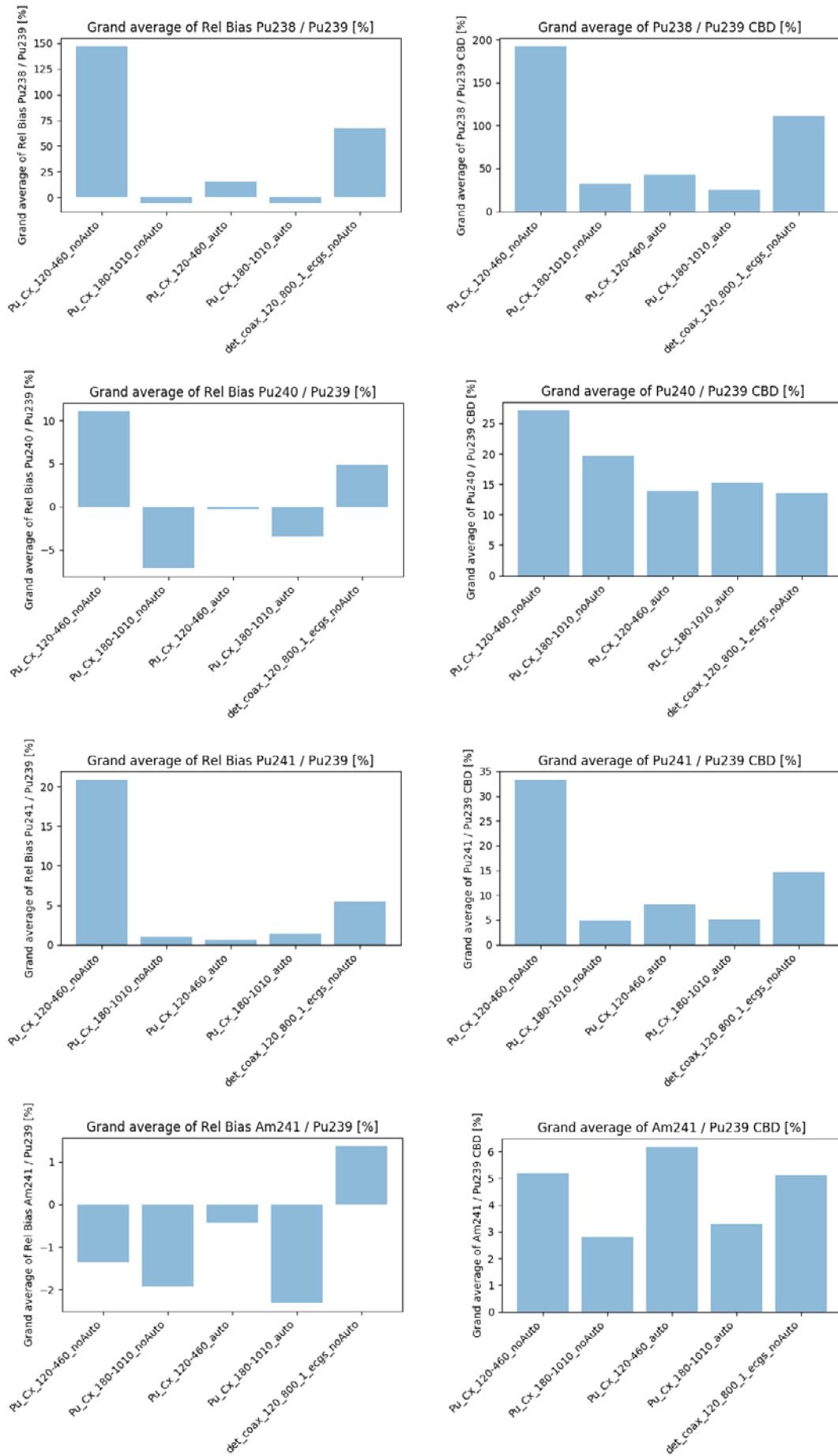
Figure 6: The grand average of the relative bias and CBD of the mass ratios for all parameter sets
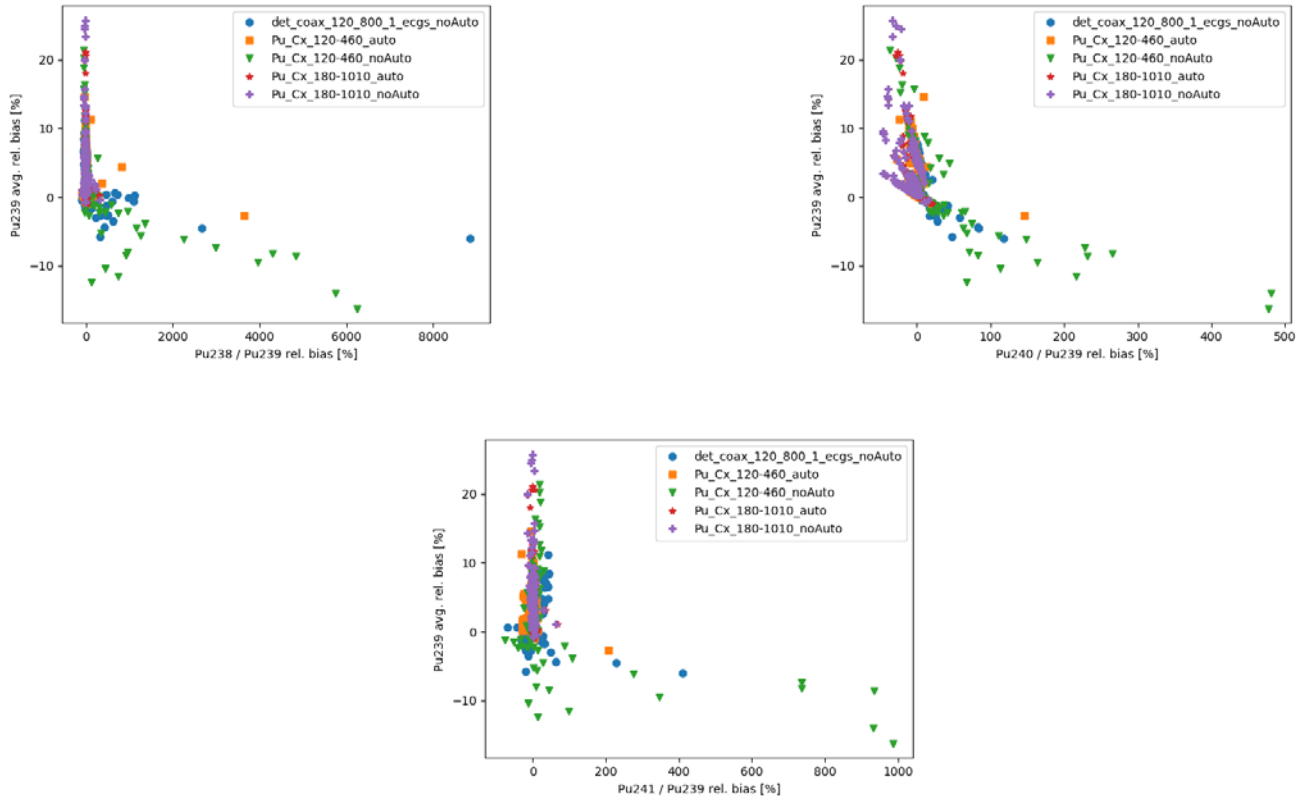
Figure 7: The average relative bias of the ^{239}Pu fraction as a function of the bias of the individual mass ratios, calculated using the ^{242}Pu correlation built in into the parameter sets. The plots calculated using the declared ^{232}Pu value are very similar.

3.3 FRAM performance in more detail

The "average plots" show the dependence of a selected quantity as a function of a measurement parameter, averaged over all identical values of that parameter in all spectra for which the selected parameter has the same value. For example, one of the points on an average plot can be the average of all spectra for which the effective shielding thickness is 16 mm, for all measurement times, for a given parameter set. The average depends on the grouping: e.g. grouping according to shielding, grouping according to spectrum quality, or grouping according to any other quantity. The parameters (groupings) investigated here are the shielding thickness and spectrum statistical quality.

3.3.1 Dependence of FRAM performance on spectrum statistical quality

The dependence of the CBD of the mass ratios on spectrum quality is shown in Figure 8. The relationship between FRAM's reported uncertainty and spectrum quality is

demonstrated in Figure 9 to Figure 12. The CBD of ^{239}Pu/ Pu mass fraction is shown in Figure 13 and Figure 14.

The measurement uncertainty is related to the spectrum quality. The counting uncertainties reported by FRAM for the mass ratios are shown in Figure 9 as a function of spectrum statistical quality. To illustrate how the CBD and RSD are related to the counting uncertainty Figure 10 to Figure 12 show the RSD, CBD and average bias for the ^{240}Pu/Pu mass ratio, as a function of the reported counting uncertainty. These figures confirm that the counting uncertainty reported by FRAM mostly covers the calculated RSD, as long as one considers "reasonable" measurements, with good spectrum quality leading to uncertainties below approximately 60%. The CBD is slightly higher than the reported counting uncertainty, due to the bias of the results. The bias can be accounted for in the FRAM parameter sets by adding a constant systematic uncertainty term. Unfortunately, the bias is not constant and depends on the measurement uncertainty (that is, on spectrum quality), as illustrated in Figure 11.
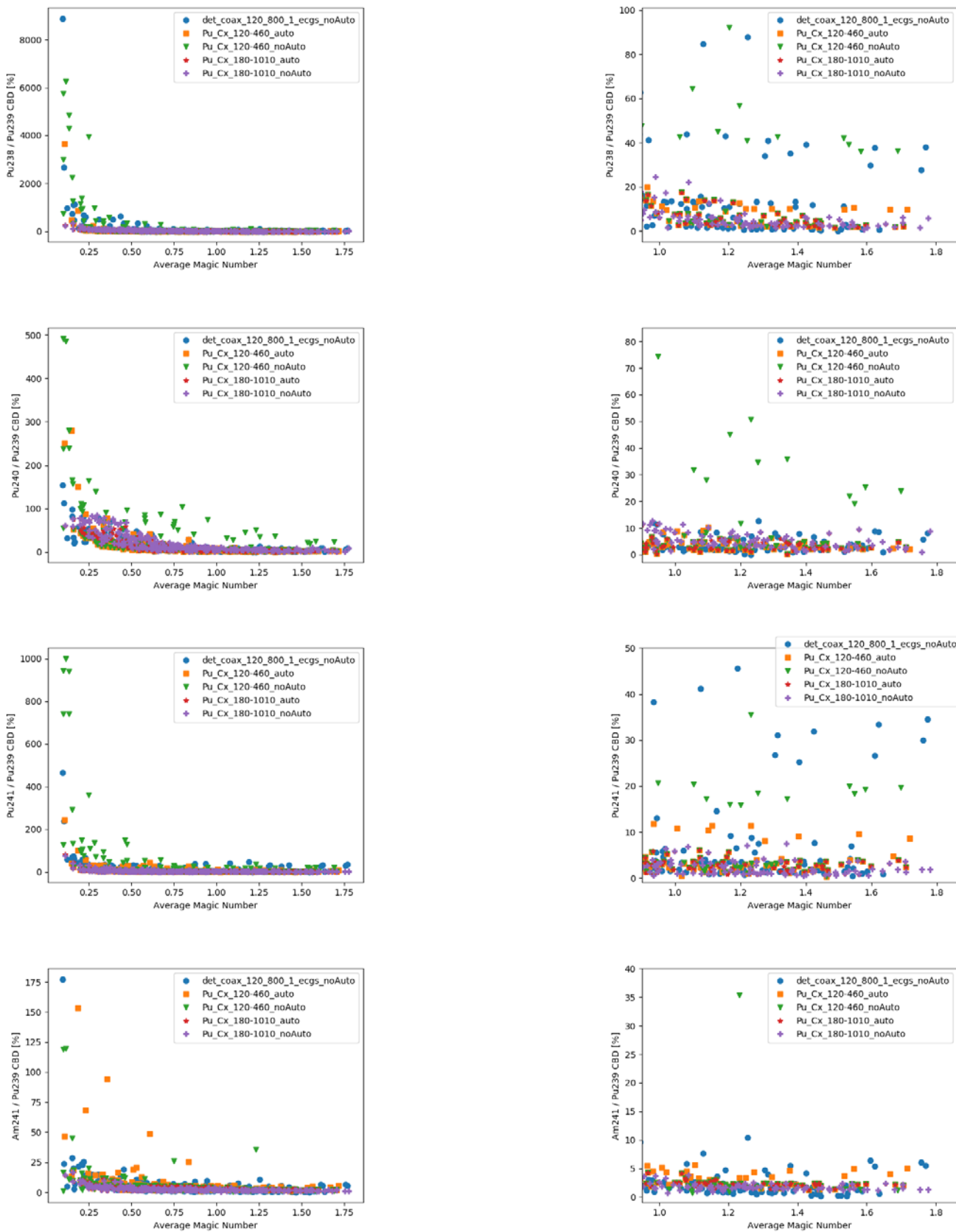
Figure 8: Average-plots of the CBD of the mass ratios as a function of statistical quality of the spectra. Left: entire range. Right: zoomed-in to higher spectrum quality.
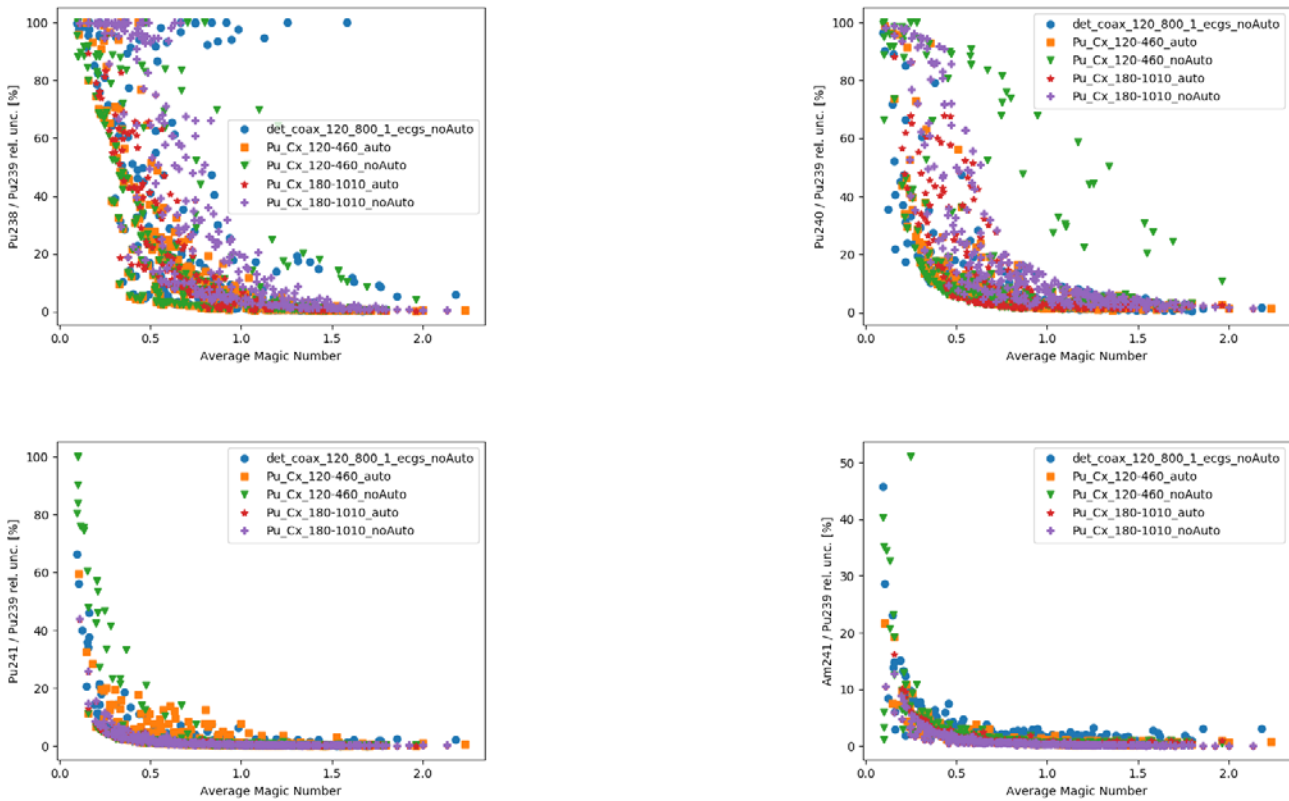
Figure 9: Average uncertainty of the mass ratios reported by FRAM, as a function of spectrum statistical quality
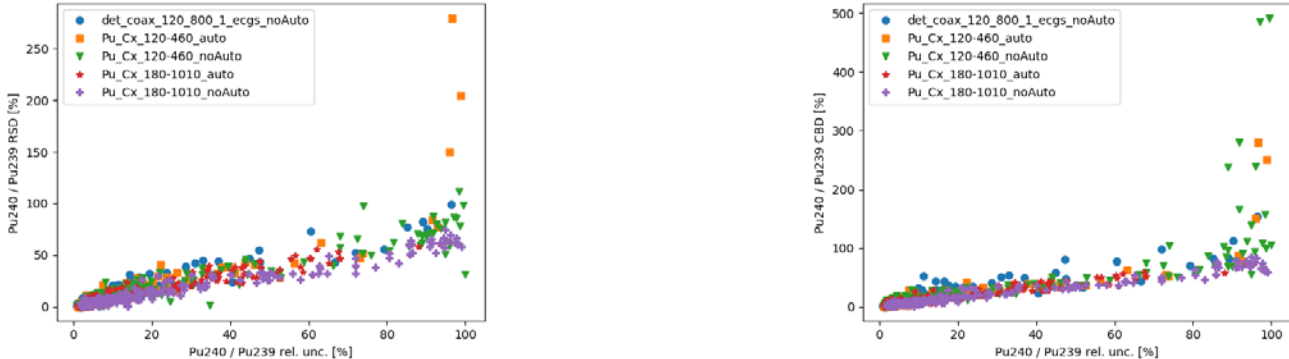
**Figure 10:** RSD and CBD of the ^{240}Pu/Pu ratio as a function of the reported counting uncertainty
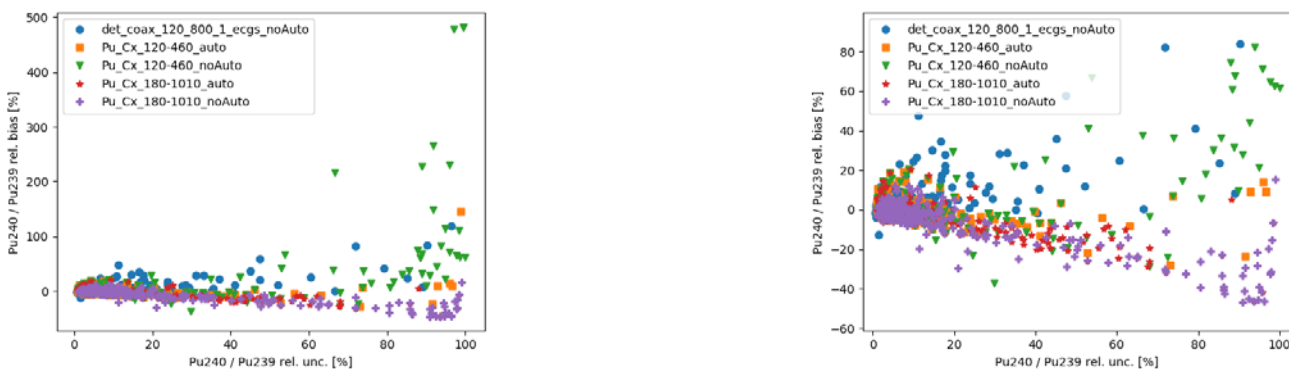
**Figure 11:** Average relative bias of the ^{240}Pu/Pu ratio as a function of the reported counting uncertainty. Left: entire plot. Right: zoomed-in to lower biases.
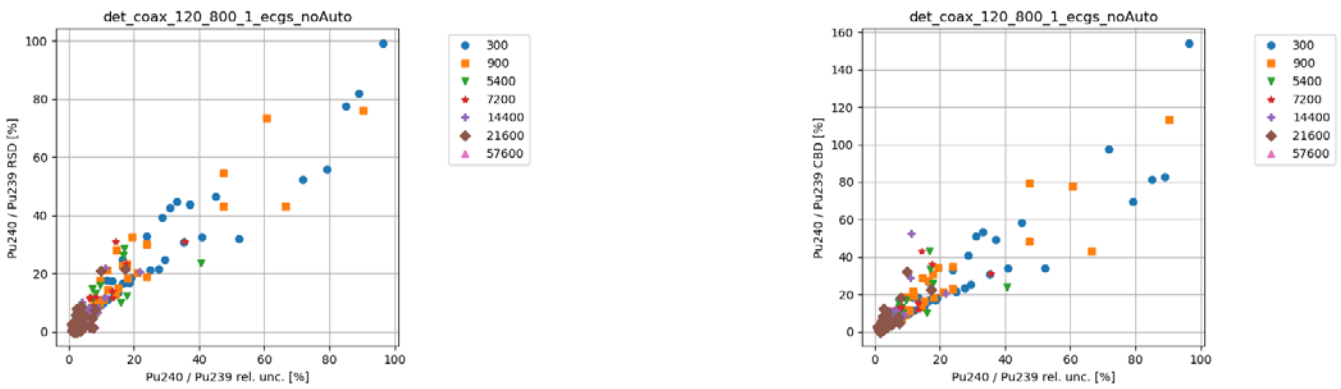
Figure 12: RSD and CBD of the ^{240}Pu/Pu ratio calculated using the parameter set det_coax_120_800_1_ecgs_noAuto, as a function of the reported counting uncertainty, for each value of the real time
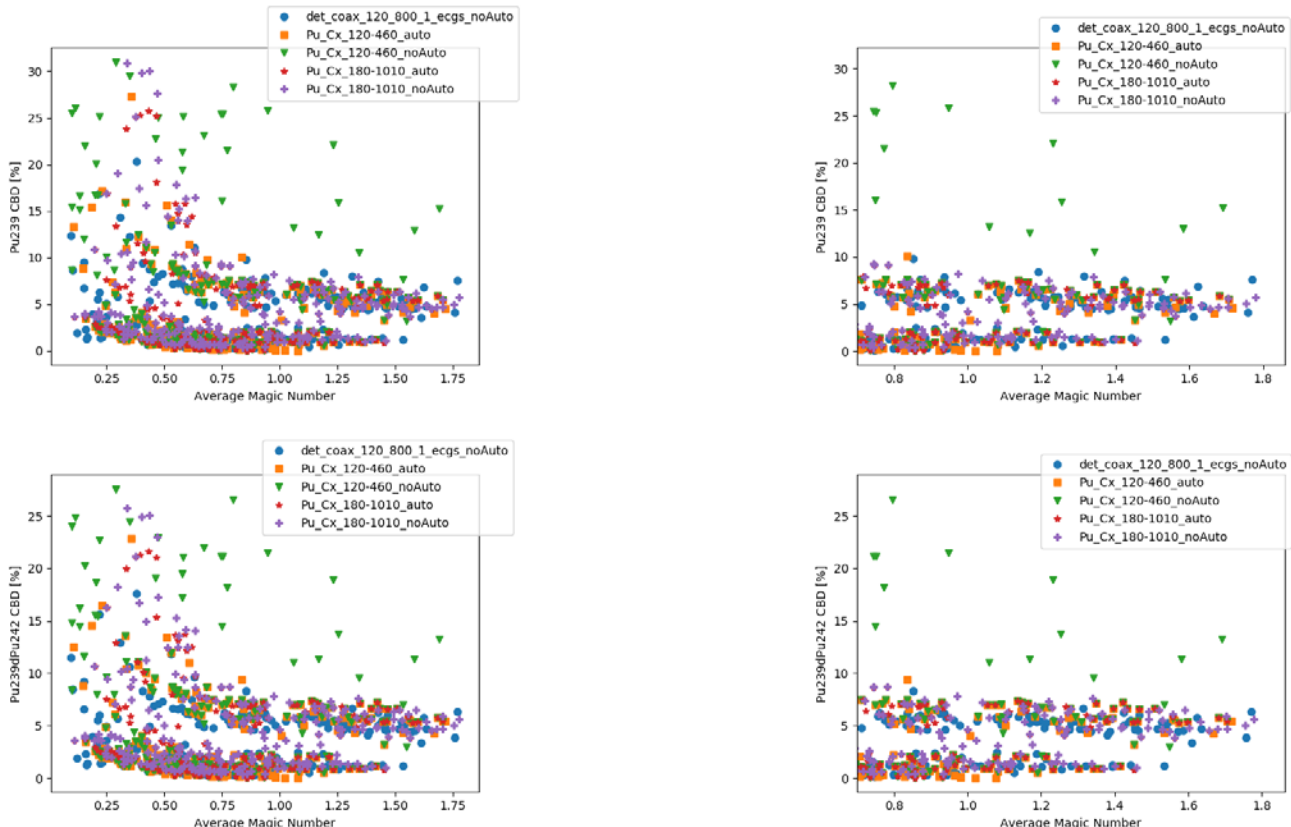

Figure 13: Average plot of the CBD of ^{239}Pu fraction as a function of statistical quality of the spectra: entire range (left) and zoomed-in to higher spectrum quality (right). The upper plots show the results using the algorithm for ^{242}Pu calculation built in into the parameter sets, while the lower plots show the results using the (decay-corrected) declared ^{242}Pu.

The average plots of the CBD of the mass ratios relative to ^{239}Pu as a function of statistical quality of the spectra show that all parameter sets give very bad results for low spectrum quality (meaning short measurement time and/or low sample activity and/or thick shielding). If the statistical indicator is above 1, then for most parameter sets the average CBD of ^{238}Pu/^{239}Pu becomes lower than 20%, the CBD of ^{240}Pu/^{239}Pu lower than 15%, the CBD of ^{241}Pu/^{239}Pu lower than 10 % and the CBD of ^{241}Am/^{239}Pu lower than 5 %. The CBD for Pu_Cx_120-460_noAuto and sometimes for det_coax_120_800_1_ecgs_noAuto is relatively high even for good spectrum quality. The reason is that these two parameter sets make use of the lower energy lines, which for shielded samples have high uncertainties even if the overall spectrum quality is relatively good.

The CBD of the ^{239}Pu/Pu fraction for good quality spectra is lower than 10 % for most parameter sets. However, Figure 13 shows two distinct groups of points: the points denoting higher CBD belong to high-burnup Pu (lower ^{239}Pu fraction), while the lower CBD belongs to low-burnup Pu. This is confirmed by Figure 14, showing the dependence of ^{239}Pu CBD on spectrum quality for each value of the declared ^{239}Pu fraction (a "category plot") for the parameter set det_coax_120_800_1_ecgs.
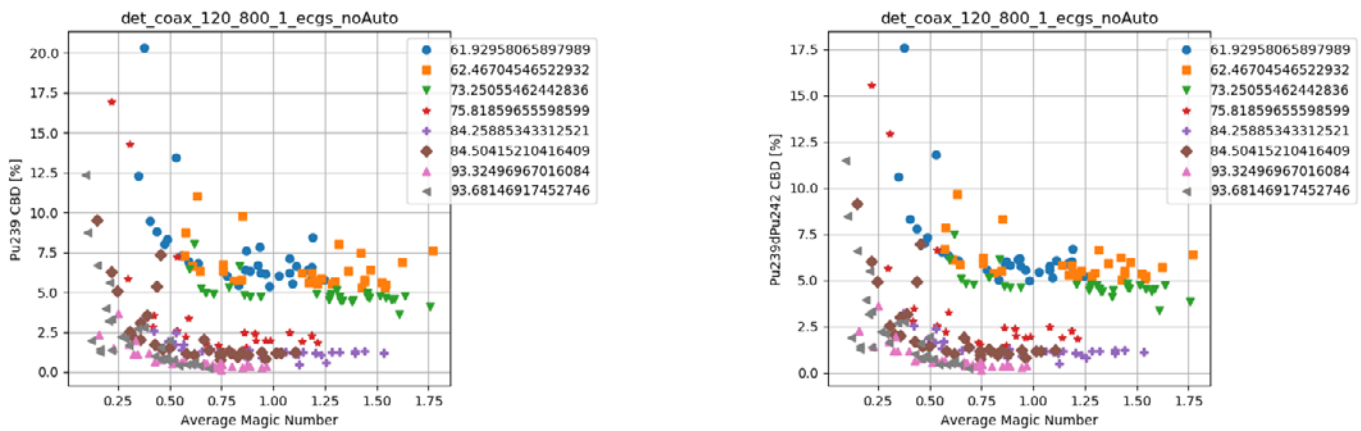
Figure 14: Dependence of ^{239}Pu CBD on spectrum quality for each value of the declared ^{239}Pu fraction (a "category plot") for the parameter set det_coax_120_800_1_ecgs. The left plot shows the results using the algorithm for ^{242}Pu calculation built in into the parameter sets, while the right plot shows the results using the (decay-corrected) declared ^{242}Pu.

3.3.2 Dependence of FRAM performance on shielding

The best results for the mass ratios are mostly obtained between 4-10 mm of effective iron (Figure 15). For effective iron shielding of 27 mm (i.e. a 4 mm sheet of Pb), the mass ratios calculated by the parameter sets that rely on lower energy peaks are biased by a few orders of magnitude, because in this case the low energy peaks cannot be reasonably analysed.

Contrary to the mass ratios, the results for the ^{239}Pu fraction are the best for the lowest shielding thickness (Figure 16). For all other shielding thicknesses the ^{239}Pu results are biased between about 2 and 5 % for all parameter sets. The ^{239}Pu fraction is calculated from the mass ratios, so why are the ^{239}Pu results best for the lowest shielding, when for the mass ratios the best results are obtained between 4-10 mm shielding? This is explained in the next paragraph.

Notice that ^{240}Pu/Pu, which has the strongest influence on ^{239}Pu, has a small positive bias for the lowest shielding. As discussed in section 3.2 about grand average plots, a positive bias in ^{240}Pu/Pu leads to a small bias in ^{239}Pu, while a negative bias in ^{240}Pu/Pu leads to a large ^{239}Pu bias. Therefore, out of the available results, the best ^{239}Pu results are those for which ^{240}Pu/Pu has a small positive bias.

In Figure 16 there are two distinct sets of points for each parameter set, just like in Figure 13 and Figure 14. The explanation for having these two groups is given by the "category plot" on the right of Figure 16 showing the ^{239}Pu relative bias as a function of effective iron shielding, for all values of the declared ^{239}Pu for the parameter set Pu_Cx_180-1010 with auto analysis turned on. On the right we see that the points with higher burnup (lower ^{239}Pu) have higher bias, resulting in the distinct groups on the left.
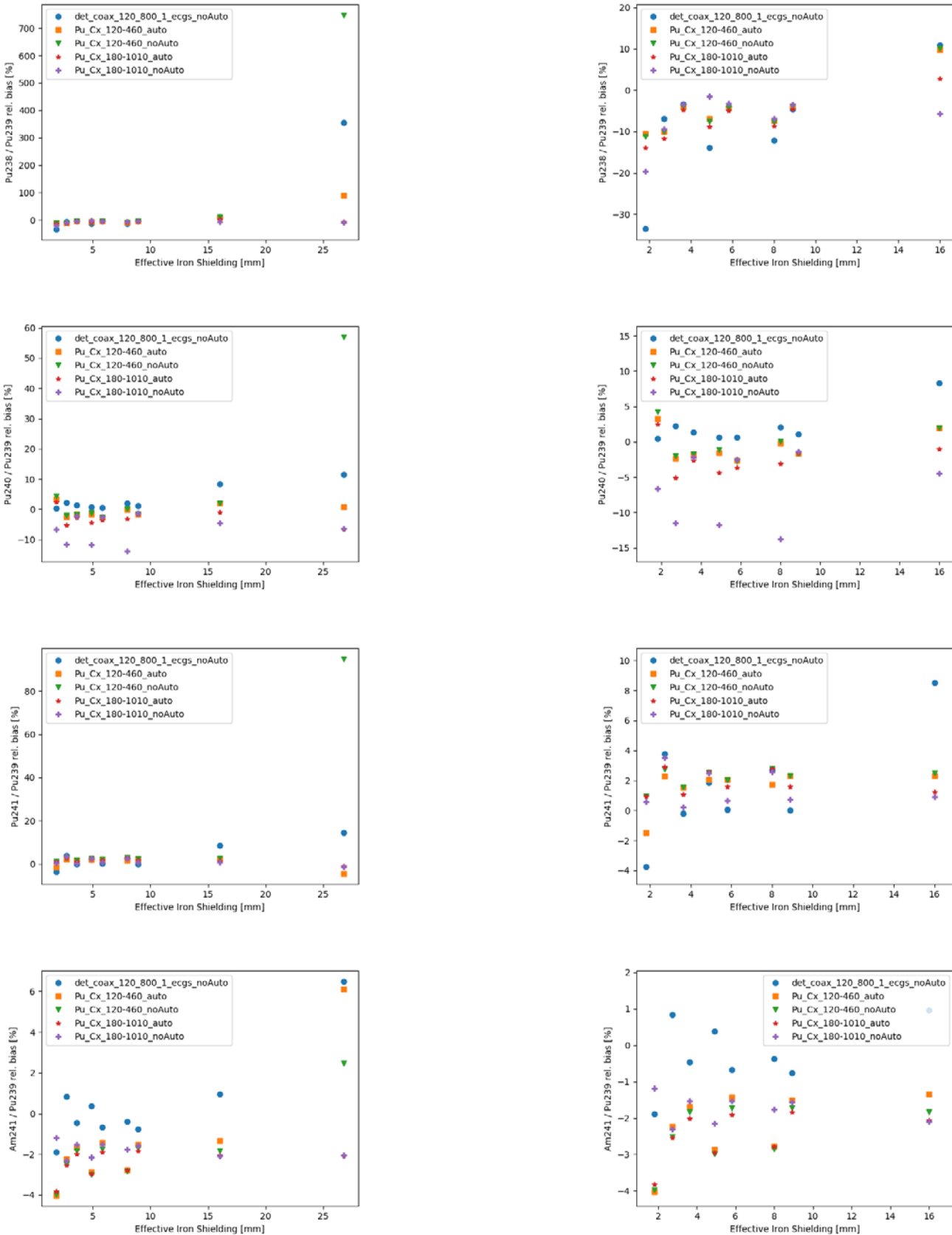
Figure 15: The average relative bias of the mass ratios as a function of effective iron shielding thickness: entire range (left) and zoomed-in to lower shielding values (right). Some points overlap, and that is why for some shieldings less than 5 points are visible. For example, Pu_Cx_180-1010 and Pu_Cx_180-1010_auto overlap for the highest shielding, because auto analysis always gives the final result using Pu_Cx_180-1010 in case of such thick shielding.
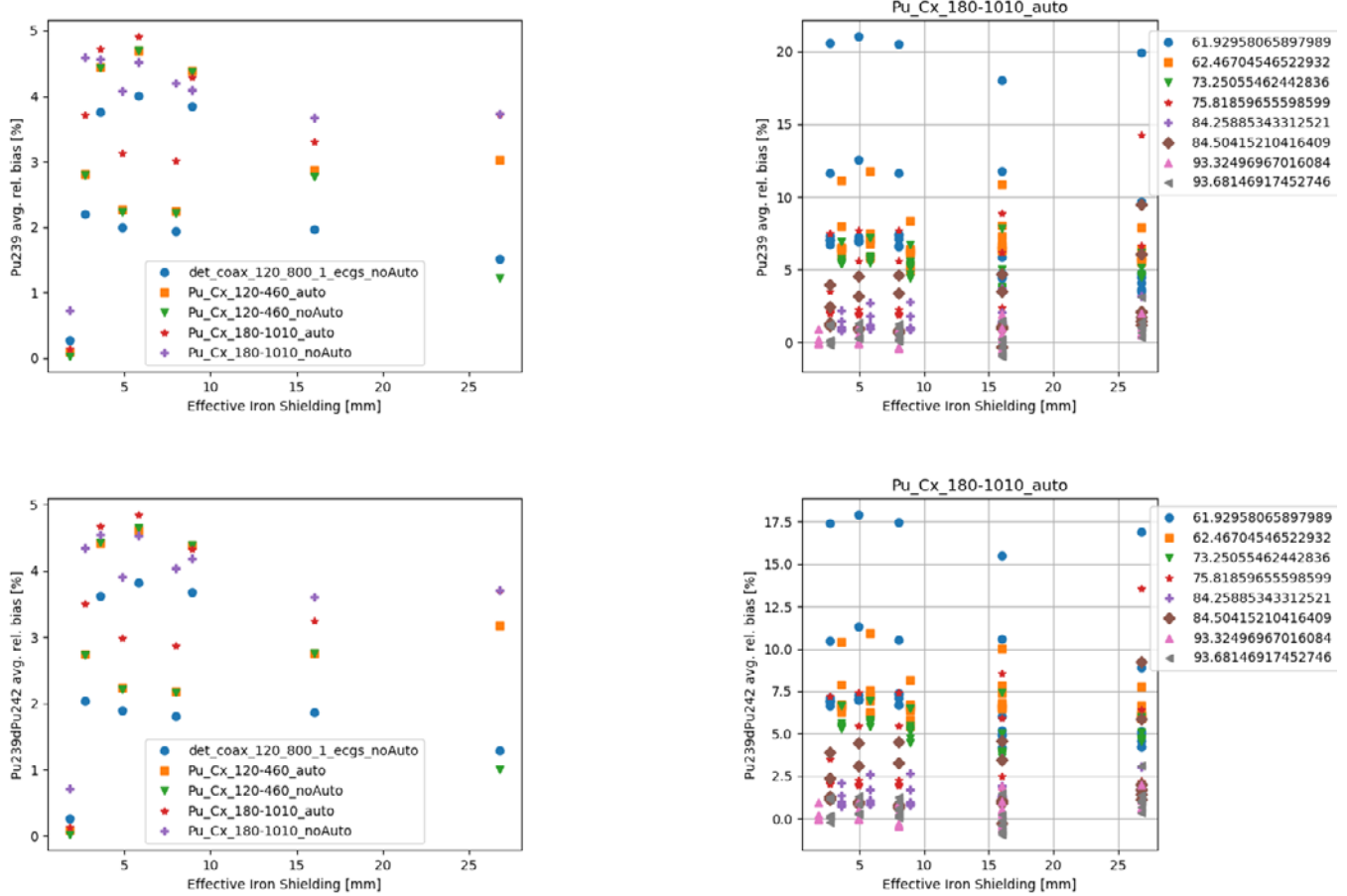
Figure 16: *Top left:* Average relative bias of the [239]Pu fraction as a function of effective iron shielding thickness for all parameter sets. *Top right:* Average relative bias of the [239]Pu fraction as a function of effective iron shielding, calculated using the parameter set Pu_Cx_180-1010 with auto analysis turned on, categorized according to the value of the declared [239]Pu. *Bottom left and bottom right*: the same as above, but using declared [242]Pu values.

3.4 When FRAM analysis fails

In some situations, especially for low quality spectra and for thick shielding, FRAM is not able to calculate one or more mass ratios and reports a zero for that mass ratio. The spectra for which FRAM gives a zero result were not included in the averages. Figure 17 shows the number of spectra for which a given parameter set failed to calculate a given mass ratio, that is, reported a zero result. Figure 18 shows the average number of zeros as a function of statistical quality.

From Figure 6 to Figure 16 one can see that for good quality spectra the best results for the various mass ratios are reported by the one of the two default parameter

sets Pu_Cx_120-460 and Pu_Cx_180-1010 with auto analysis turned on. However, in case of low spectrum quality the default parameter sets often fail (i.e., report zero mass ratio) and in that case the parameter set det_coax_120_800_1_ecgs, which uses simultaneously the high and low energy region, provides the optimum results, as seen on Figure 17 and Figure 18.

As mentioned above, and as shown in Figure 18, FRAM failures happen with low quality spectra. Most FRAM failures happen with the 5 minute spectra and PIDIE samples as illustrated in Figure 19, showing, as an example, the average number of zeros for the [238]Pu/[239]Pu ratio.
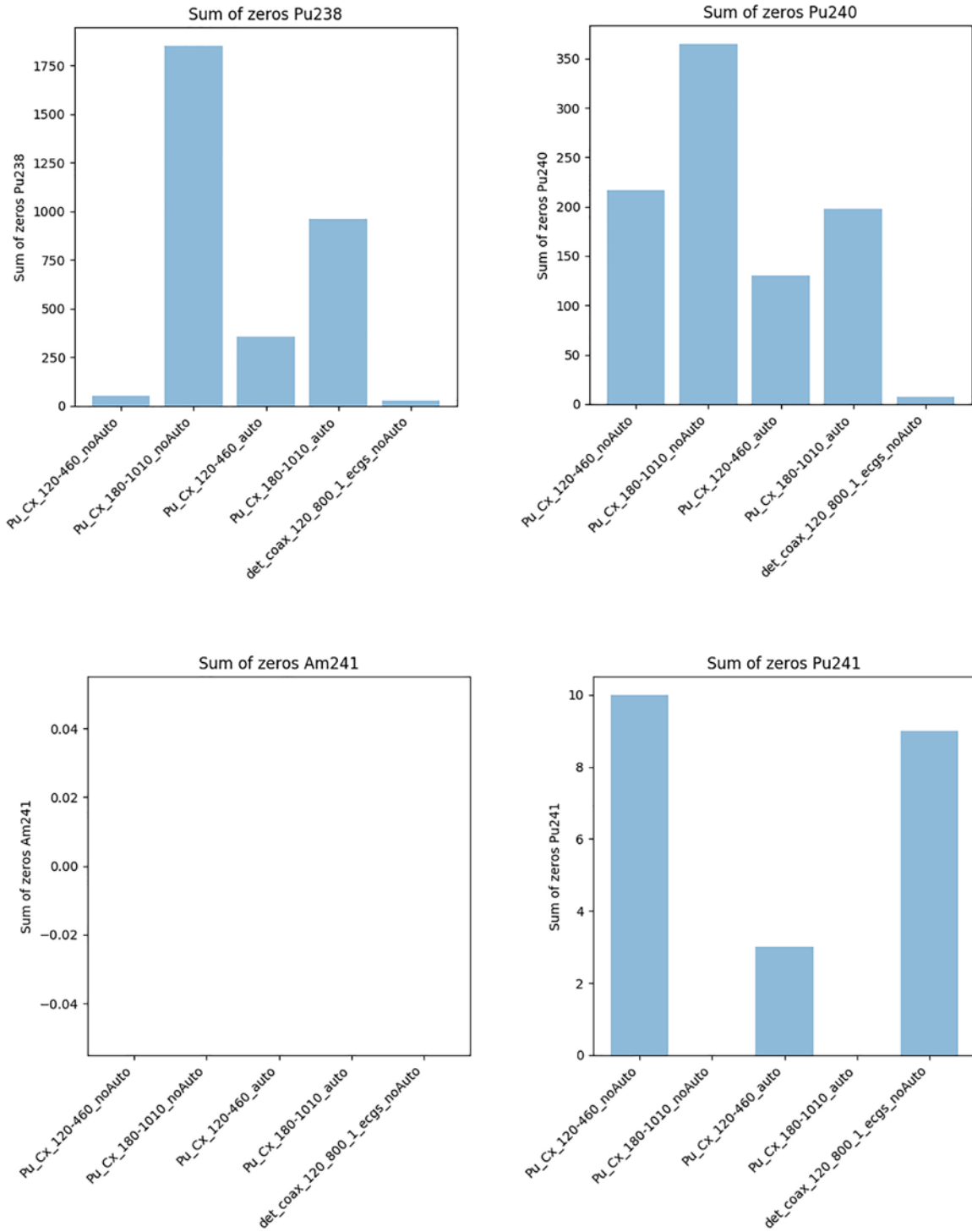
Figure 17: The sum of zeros (failures), out of 11240 analysed spectra, for the various mass ratios for different parameter sets. For ^{241}Am FRAM never fails with zero results.
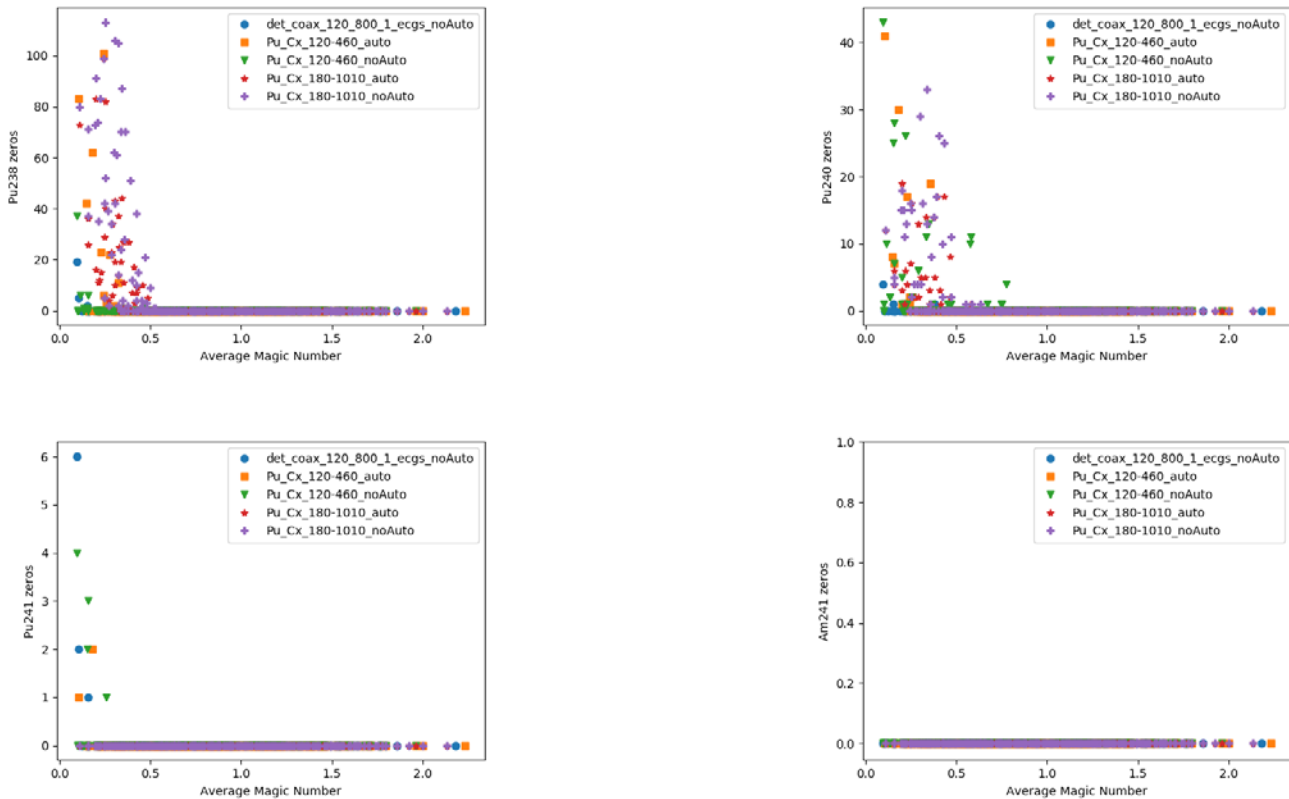
Figure 18: The average number of zeros of the various mass ratios as a function of statistical quality of the spectra, for all parameter sets
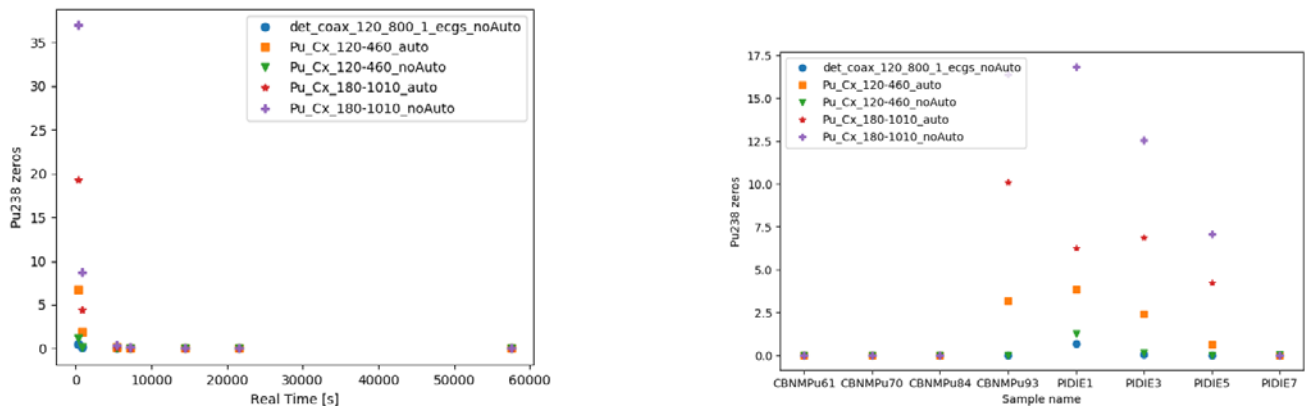
Figure 19: Average number of zeros for the ^{238}Pu/^{239}Pu ratio, as a function of real time (left) and sample name (right).

4. Conclusion

The auto analysis option significantly improves the performance of the default parameter sets Pu_Cx_120-460 and Pu_Cx_180-1010, especially in the case of lower quality spectra. This option enables FRAM to distinguish, e.g., shielded and unshielded samples and automatically re-analyse the spectrum using a parameter set that is better suited for the particular setup.

For the mass ratios relative to ^{239}Pu the default parameter sets (with auto analysis on) provide similar results, better than the set det_coax_120_800_1_ecgs. However, for the ^{239}Pu fraction the set det_coax_120_800_1_ecgs is superior to both default sets.

FRAM results heavily depend on the statistical quality of the spectra, as expected. A statistical indicator, called the "magic number", was used in this work to measure the statistical quality of the spectra. If this number is below 1, then the bias of the results can go up several orders of magnitude, especially for the ^{238}Pu/^{239}Pu mass ratio. For some of the measured samples the "magic number" does not go above 1, even for long measurement times and thin shielding, due to their low activity.

To improve the results for the ^{239}Pu fraction, it would be essential to improve the calculation of the ^{240}Pu/^{239}Pu ratio. Another step forward could be to create parameter sets accompanying the set det_coax_120_800_1_ecgs, in order to benefit from the possibilities offered by auto analysis.

These conclusions are valid for very old (>20 years), pure Pu samples. The extension of the studies to 1-2 years old MOX samples is planned.

5. References

[1] J. Zsigrai, A. Frigerio, J. Bagi, A. Mühleisen, and A. Berlizov, "Using FRAM to determine enrichment of shielded uranium by portable electrically cooled HPGe detectors," in *Proceeidings of the 39th ESARDA Annual Meeting - Symposium, 16-18 May 2017, Düsseldorf, Germany*, 2017, pp. 80–86.

[2] T. E. Sampson and T. A. Kelley, "PC/FRAM: A code for the non-destructive measurement of the isotopic composition of actinides for safeguards applications, LA-UR-96-3543," 1996.

[3] T. E. Sampson, T. A. Kelley, and D. T. Vo, "Application Guide to Gamma-Ray Isotopic Analysis Using the FRAM Software, LA-14018," 2003.

[4] D. T. Vo, "Operation and Performance of FRAM Version 5.1 Proceeding of the 52nd Annual Meeting of The Institute of Nuclear Materials Management, Palm Desert, CA, USA, July 17-21, 2011, LA-UR-11-03016," 2011.

[5] "Micro-Detective Ultra light, Portable Hand Held Radioisotope Identifier." https://www.ortec-online.com/products/nuclear-security-and-safeguards/hand-held-radioisotope-identifiers-riids/micro-detective (accessed Mar. 29, 2020).

[6] "CBNM Nuclear Reference Material 271, Certificate of Analysis, Commission of the European Communities, Joint Research Centre, Central Bureau for Nuclear Measurements, Geel," Geel, 1989.

[7] R.J.S. Harry, "PIDIE, plutonium isotopic determination inter-comparison exercise, ECN-RX--90-044," in *Annual Meeting of the Institute of Nuclear Materials Management*, 1990, no. July, pp. 15–18.

[8] J. Morel and B. Chauvenet, "Intercomparaison des mesures de composition isotopique du plutonium par spectrometrie X et gamma. Resultats de l'action 'Pidie', rapport final, CEA Centre d'Etudes de Saclay, Gif-sur-Yvette (France). Dept. des Applications et de la Metrologie des Rayonnem."

[9] J. Morel, B. Chauvenet, and M. Etcheverry, "Final results of the PIDIE intercomparison exercise for the plutonium isotopis determination by gamma spectrometry," in *Proceedings of the 13th ESARDA Symposium, Avignon, France*, 1991, pp. 251–257.

[10] C. T. Chantler *et al.*, "Detailed Tabulation of Atomic Form Factors, Photoelectric Absorption and Scattering Cross Section, and Mass Attenuation Coefficients for Z = 1-92 from E = 1-10 eV to E = 0.4-1.0 MeV," 2005. https://www.nist.gov/pml/x-ray-form-factor-attenuation-and-scattering-tables (accessed Aug. 01, 2018).

Antineutrino Detection Techniques for Monitoring Long-Term Geological Repositories

Madalina Wittel and Malte Göttsche

Nuclear Verification and Disarmament Group
Physics Institute III B & AICES Graduate School – RWTH Aachen University
Schinkelstraße 2, 52062 Aachen, Germany
E-mail: wittel@aices.rwth-aachen.de, goettsche@aices.rwth-aachen.de

Abstract:

The radioactive nuclear waste produced in the past decades contains many significant quantities of plutonium, one of the key ingredients for manufacturing nuclear weapons. For the first few hundreds of years after discharge, the dominant radioactivity of the waste comes from long-lived beta-decaying elements, in particular ^{90}Sr and ^{137}Cs. In this paper, we discuss the prospects of safeguarding long-term geological nuclear waste repositories by detecting the low-energy antineutrinos emitted via beta-decays. We investigate whether these antineutrino measurements could be carried out with time projection chambers, for example using liquid argon. In contrast to the typical scintillation or water-Cherenkov detectors, this emerging technology could detect antineutrinos even below the inverse beta decay kinematic threshold, i.e. the typical energy range for radioactive waste emissions. Furthermore, due to their imaging properties, time projection chambers could also provide directionality information which may be used for background rejection and potentially also for indicating if and where a certain amount of nuclear waste has been diverted. We present a first feasibility study for employing liquid-argon detectors for safeguarding geological repositories. We consider a realistic repository layout as a study case and evaluate the detector performance in this context, from first principles.

Keywords: radioactive waste; geological repositories; safeguards; antineutrino detection

1. Introduction

As nuclear programmes become older, safeguarding the radioactive waste becomes more important.

The International Atomic Energy Agency (IAEA) evaluated that the global cumulative amount of spent fuel (SNF) was approximately 380,500 tonnes heavy metal at the end of 2014 [1]. Furthermore, based on the output of the 438 reactors in operation in 2014, the IAEA estimated that about 10,000 tonnes of spent fuel are discharged every year. This implies that, presently, more than 430,000 tonnes spent fuel are stored around the world.

The typical spent nuclear fuel composition depends on the reactor burnup. Table 1 shows the evaluated composition of SNF extracted from a light-water reactor considering a burnup of 50GWd/t [2]:

Material	Relative amount
Uranium (< 1% ^{235}U, mostly ^{238}U)	93.4%
Fission products (^{129}I, ^{90}Sr, ^{135}Cs, etc.)	5.2%
Plutonium	1.2%
Minor actinides (^{237}Np, ^{241}Am, ^{243}Cm, etc.)	0.2%

Table 1: Typical isotopic composition of spent nuclear fuel [2]

The Institute for Science and International Security estimated that, at the end of 2014, the amount of civilian irradiated (i.e. present in spent fuel) and unirradiated (directly usable for nuclear weapons) plutonium was approximately 2,400 tonnes, increasing by approximately 50 tonnes per year [3]. A breakdown of the civil plutonium stocks per country at the end of 2014 is given in Fig. 1. The amount of irradiated plutonium is several factors larger than the unirradiated quantity. While the unirradiated plutonium is more susceptible for proliferation, also spent fuel could in principle be diverted to separate the plutonium.
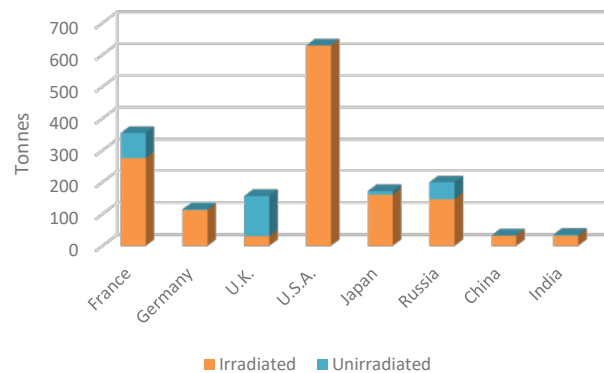
Figure 1: The amounts of irradiated and unirradiated plutonium held per country at the end of 2014. [3]

The spent fuel will eventually need to be stored in permanent geological repositories, which require safeguards to prevent diversion. In conceptualizing safeguards options, the IAEA currently focuses on the "early detection of unauthorized

movement of fissile material" [4] which could occur in the form of e.g. unexpected excavations. Thus, the envisioned monitoring techniques include: (*i*) site inspections, (*ii*) aerial photography, (*iii*) satellite imagery and (*iv*) microseismic surveys [4].

A different approach that should be examined is the potential use of antineutrino monitoring in this context. If operated continuously, it could be a new tool for Continuity of Knowledge, providing redundancy to the foreseen containment and surveillance measures. A change in the antineutrino flux, once detected, serves as clear, difficult to fake evidence of clandestine material diversion. Furthermore, it could be used in a re-verification context, by comparing the detected antineutrino rate and spectra to what would be expected, either from measurements before the loss of Continuity of Knowledge, or from results of a repository simulation model built from information provided in the inventory declaration. Even a rough estimate of the potential diversion region may be possible.

In this paper, we discuss the potential use of antineutrino monitoring by presenting first results of a feasibility study that focuses on imaging detectors, which may provide significant advantages compared to other detector types. The paper is organized as follows: in section 2, we discuss the main properties of the antineutrinos emitted by the radioactive waste and the need for new detection techniques. The potential way forward, i.e. time projection chamber detectors, is presented in section 3 with a focus on liquid-argon-filled detectors. The first results of our feasibility study are summarised in section 4.

2. Antineutrinos for Monitoring Geological Repositories

The concept of antineutrino monitoring of spent nuclear fuel has been proposed by Brdar et al. [5]. In the first few hundreds of years, the dominant radioactivity of the waste stems from the beta-decaying fission products. While many isotopes have rather short half-lives (in the order of several hours or a few days), in particular ^{90}Sr ($T_{1/2} = 28.78$ years) and ^{137}Cs ($T_{1/2} = 30.17$ years) contribute also decades later.

Due to their weakly interacting nature, with cross-sections lower than 10^{-38} cm^2, the antineutrinos escape even large amounts of shielding and can propagate through the geological structures surrounding the repository. There is no means to deflect the antineutrinos' trajectories. At the same time, the prospects of using antineutrino measurements in a safeguards context will be analysed here in view of the potentially long measuring times due to their low cross-sections.

2.1 Properties of Antineutrino Emissions from Radioactive Waste

To evaluate the antineutrino emissions from radioactive waste, the operation of a pressurized water reactor (PWR) was simulated with SERPENT 2 [6], a Monte Carlo neutron transport and burnup calculation code. The reactor model was based on the description given in [7] and it was implemented with an enrichment of 4% and burnup of 33 MWd/kg.

Antineutrino emission spectra (Fig. 2) were computed at seven different time steps between 100 and 500 years from the considered moment of discharge by summing over the spectra for each beta-decaying nuclide.

As can be seen, the antineutrino emissions have a low energy range, i.e. from a few eV up to approximately 4.3 MeV. This constitutes a challenge for the antineutrino detection, since typical reaction cross-sections decrease at lower energies. However, it can also be observed that, even after more than 200 years since discharge, a significant number of antineutrinos, i.e. $\mathcal{O}(10^{12})$ for energies integrated below 2.3 MeV, are still emitted.
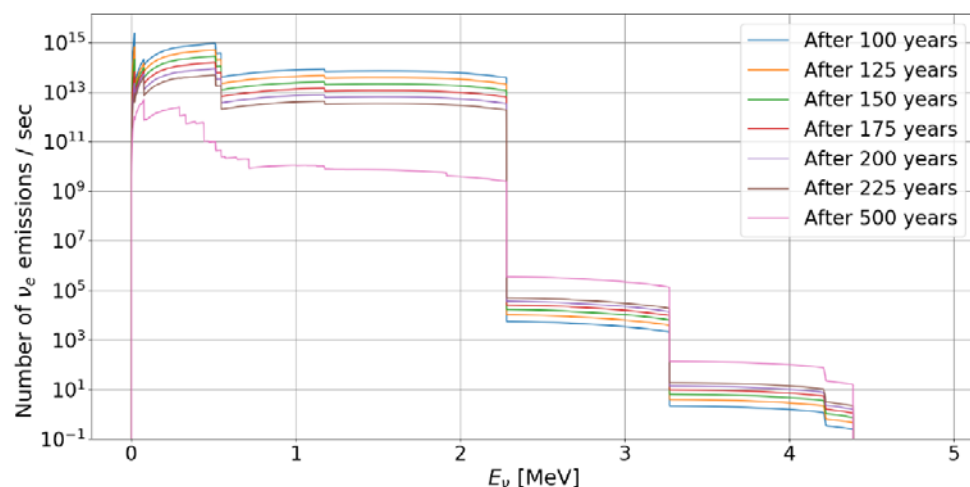
Figure 2: Antineutrino emission spectra from one fuel assembly of a simulated PWR reactor with a burnup of 33 MWd/kg and enrichment of 4% computed at seven different time intervals from the simulated discharge [8].

2.2 Motivation for New Antineutrino Detection Methods in the Safeguards Context

The use of antineutrino measurements for monitoring purposes has already been considered in the case of nuclear reactors, i.e. for determining reactor shut-down periods or estimating the plutonium content in the core. Since antineutrinos interact only weakly, the detector must provide a large mass and a high target density to achieve a reasonable detection time. Two research projects in this context are WATCHMAN [9] and CHANDLER [10].

In both the WATCHMAN and CHANDLER detectors (a water-Cherenkov and scintillation detector, respectively), the anti-neutrinos interact with the sensitive material by means of the inverse beta decay (IBD) reaction: $\bar{\nu}_e + p \rightarrow e^+ + n$, which is characterised by a kinematic threshold: it can only occur for antineutrino energies E_ν larger than 1.8 MeV. As can be seen from Fig. 2, relying exclusively on the IBD reaction, one could detect less than 20% of the antineutrinos coming from the described radioactive waste. Consequently, a sensitive material which would enable antineutrino reactions without an intrinsic energetic threshold would be desirable.

Furthermore, for safeguards purposes, a directionality capability would be helpful, especially since the antineutrino emission rate decreases with time: reconstructing the incoming direction of the antineutrino emissions could be used for background rejection and potentially also for indicating where a certain amount of nuclear waste has been diverted. While not impossible, it is very challenging to obtain directionality information from the IBD reaction – a large number of detected events ($\mathcal{O}(10^3)$) is required to locate the source with an angular resolution of a few degrees [11].

Recently, as the interest in the field of fundamental neutrino research is gradually encompassing the lower energy range of solar and supernova antineutrinos, new detection methods are proposed and/or prototyped. Antineutrino detectors based on time projection chambers filled with liquefied noble gases or organic-liquid scintillators seem to be particularly promising.

3. Time Projection Chambers for Antineutrino Detection

The idea of using time projection chambers (TPCs) with noble gases for neutrino detection was first proposed by Carlo Rubbia in 1977 [12]. It is only in the last decade that TPC prototypes have been realised and tested in the field of fundamental neutrino physics and dark matter detection.

3.1 Fundamentals of TPCs

The TPCs considered for antineutrino detection typically consist of a large volume of liquefied noble gas like argon or xenon. Argon constitutes approximately 1% of Earth's atmosphere, especially the ^{40}Ar isotope with an abundance of 99.6%, it is usually cheap to produce (and to liquify) and it is commercially available. The volume is encompassed by a high-voltage cathode on one side and an anode on the opposite surface which also contains several read-out wire planes. The uniform electric field realised between the cathode and the anode planes typically has a strength of 500 V/cm. To be liquid, the noble gas must be cooled to a very low temperature, e.g. 87K (-186.15° C) in the case of argon. More recently, organic-liquid scintillating materials like tetramethylsilane appear to be very promising, especially since they can operate at room temperature.

When an (anti-)neutrino interacts via charged or neutral current exchange with an atom in the sensitive material, i.e. either with the electrons or the nucleus itself, the emergent particles ionise and excite further atoms along their trajectory. The emitted free electrons drift in the liquid, under the force of the electric field, until they reach the read-out wires, in which they generate small currents. The wires are placed at very close distance to each-other, e.g. 3-5 mm, and constitute a very dense net. To obtain multi-dimensional information about the charged particles' tracks, several wire planes can be used, placed under different angles with respect to each other. In addition, the excited atoms also emit scintillation light which can be measured with photosensors (PMTs). The light signal can be used to trigger the signal acquisition. Liquid argon is an excellent scintillator, providing approximately 4×10^4 photons per MeV [13].

Thus, one of the main benefits of using time projection chambers stems directly from their mode of operation: unlike water or scintillator detectors, they are *imaging* detectors – providing a three-dimensional reconstruction of the tracks left by the charged particles emerging from an antineutrino interaction. It enables a reconstruction of the antineutrino energy and its incoming direction on an event-by-event basis, which is helpful for background rejection.

TPCs filled with an organic-liquid scintillator that can operate at 15-20°C would be well suited for monitoring geological repositories since they require no additional cryogenic infrastructure. However, more research and development work are required to demonstrate the feasibility and performance of these proposed sensitive materials.

In contrast, liquid-argon-based detectors (LArTPCs) require cooling but have already been built and tested in fundamental physics experiments like, e.g. ArgoNeuT [14] and MicroBoone [15]. Furthermore, they are considered for large-scale neutrino fundamental research experiments like DUNE [16]. Consequently, we will focus on liquid-argon TPCs in the rest of this paper.

3.2 Antineutrino Interactions in Liquid-Argon

In the standard water-Cherenkov or organic-scintillator-based detectors, antineutrinos mostly interact by means of the inverse beta decay process: $\bar{\nu}_e + p \rightarrow e^+ + n$. However, since there are no free protons available in liquid argon, this reaction cannot take place. The analogous reaction in liquid argon is the charged current absorption: $\bar{\nu}_e + {}^{40}\text{Ar} \rightarrow e^+ + {}^{40}\text{Cl}^*$. However, its energy threshold in the case of antineutrinos is even higher: $E_\nu > 7.5$ MeV, which makes it unfeasible for the antineutrino energy range relevant for safeguarding geological repositories (cf. Fig. 2).

In the elastic scattering reaction, the anti-neutrino scatters off electrons of the argon atoms: $\bar{\nu}_e + e^- \rightarrow \bar{\nu}_e + e^-$. This reaction is very important since, unlike IBD, it can provide the desired directionality information directly: the energy of the incoming antineutrino is usually larger than the rest mass of the electron, therefore, the latter carries away most of the antineutrino momentum and its direction is correlated to that of the incoming antineutrino.
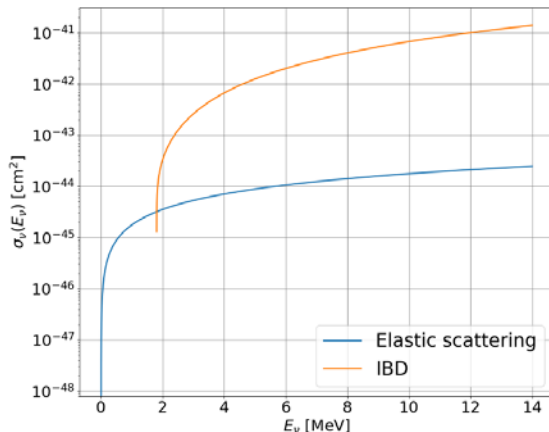
Figure 3: The energy-dependent antineutrino cross-sections for the elastic scattering and IBD reactions, based on the analytical calculations described in [17] and [18], respectively.

However, the cross-section of the elastic scattering reaction is about two orders of magnitude lower than the one of IBD, as can be seen from Fig. 3. This clearly poses a detection challenge and is somewhat compensated by the higher target density provided by the liquid-argon. Nevertheless, it can also be seen that the reaction is kinematically allowed for the entire energy range relevant for the antineutrino emissions from radioactive waste.

A second reaction that can occur in liquid argon is the coherent elastic neutrino-nucleus scattering (CEνS). It occurs via weak neutral current and essentially refers to antineutrinos being scattered off entire argon nuclei. The cross-section of this reaction in liquid argon is expected to be approximately of the order of $\mathcal{O}(10^{-38})$ cm^2, i.e. about three orders of magnitude higher than the IBD cross-section.

The CEνS cross-section is presently being measured by experiments such as e.g. COHERENT [19]. Despite the high cross-section, the recoil energy of the nucleus is very low, in the order of a few tens of keV, and it remains to be seen whether this reaction is detectable at all in a LArTPC. Consequently, the CEνS interaction is not taken into account in the present study. Thus, the antineutrino elastic scattering off the electrons in the argon atoms is the interaction considered in the following.

Liquid argon (^{40}Ar) provides a target density comparable to water and scintillator materials, e.g. like the one used for the KamLAND neutrino detector [20]. Table 2 shows a comparison of several sensitive materials in terms of the number of expected events in 80 tonnes of material. For this comparison 500 tonnes of spent nuclear fuel (SNF) with a cooling time of 100 years have been considered and treated as a point source for the antineutrino emissions. A distance of 50 m between the detector and the emissions' source was assumed. Furthermore, only two signal interactions were considered: the elastic scattering off electrons in liquid argon and the inverse beta decay reaction for water and the scintillator materials, respectively. The reaction cross-sections and the expected number of targets in the sensitive material volume have been computed accordingly. For each material, a detection time of 100 days was assumed.

Detector type	Nr. Events in 80 t and 100 days
LArTPC	128
Water-Cherenkov	93
Scintillator (KamLAND [20])	204

Table 2: Comparison between liquid argon and other typical antineutrino sensitive materials in terms of the expected number of SNF antineutrino events in 80 tonnes of material. The computation assumes the SNF is 100 years old. The relatively high target density of liquid argon compensates the lower elastic scattering cross-section. The main advantage of the LArTPC technology, however, remains its directionality capability.

4. Prospects for Safeguarding Geological Repositories with Liquid-Argon Detectors

To evaluate the feasibility of monitoring or re-verifying long-term geological repositories by measuring antineutrino emissions with liquid-argon detectors, a study case was defined. Four storage areas in the eastern region ("Ost 5", "Ost 6", "Ost 7" and "Ost 8") of the proposed "B1" layout for the planned repository in Gorleben, Germany were considered [21]. Presently, Gorleben is no longer regarded as a potential location for a long-term geological repository and the scientific investigations were stopped in 2012. Nevertheless, the initial studies were detailed enough to form the basis for a simulation of the repository.

The study case repository comprises 1120 containers with 10 fuel assemblies each. While the different ages of the fuel

assemblies were correctly taken into account, we assumed that only fuel assemblies from pressurised water reactors with 55 MWd/kg burnup are stored. This is a simplification, as a detailed model is beyond this paper's scope. The B1 repository layout foresaw that the storage caverns would be located at a depth of 870 m [21]. In the study case, it was envisaged that the antineutrino detector would be placed at the same depth as the repository, but 100 m away from the nearest containers and completely decoupled from the rest of the repository, i.e. in a cavern of its own. In view of the transport and deployment requirements, it was considered that the antineutrino detector would have the dimensions of a regular shipping container. 80 tonnes of liquid-argon constitute about 70% of the volume, while the remaining 30% are necessary for the thermal insulation which enables the argon to be maintained in a liquid form. For the preliminary evaluation discussed here, it was assumed that the entire sensitive volume is fully instrumented and that the detection efficiency is 100%.

4.1 Expected Detection Rate

The detection rate in the liquid-argon detector considered for the study case was calculated according to: $N_v(E_v) = \Phi_v(E_v) \cdot T \cdot \sigma(E_v)$, where Φ_v is the energy-dependent antineutrino flux at the location of the detector, T is the number of targets in the detector active volume and σ is the differential cross-section for elastic scattering shown in Fig. 3. The antineutrino flux is expressed as the number of emissions per second and per cm^2 and it takes into account the distance between the detector and the emissions' source. The number of targets T was computed based on the target density expressed in number of electrons per cm^3. The detection rate was then scaled up to the detector size.

Table 3 shows the antineutrino detection rate for different times after 2020. For this study, an optimistic detection efficiency of 100% has been assumed since the efficiency of the LArTPC technology in the low energy range is presently being investigated.

Time elapsed since 2020 [years]	Number of antineutrino events detected within 3 months
100	1116
125	615
150	339
175	187
200	103
225	57
500	< 1

Table 3: Total detection rates of the antineutrino emissions (without background), based on a study-case layout of a geological repository comprising 11200 fuel assemblies of different ages and with a burnup of 55 MWd/kg. [8]

It can be seen from Table 3 that the expected detection rate diminishes significantly with time, as the amount of beta-decaying isotopes present in the radioactive waste decreases. Nevertheless, the number of observed antineutrinos is above 100 even after year 2220.

The background reduction efficiency was optimistically assumed to be 100% in this preliminary study. The largest background contributions stem from the solar neutrinos (120 counts per day in an 80 t LArTPC) and the cosmogenics, i.e. beta-decaying elements produced in detector materials via spallation induced by high-energetic cosmic muons (39 counts per day). This estimation is based on [22], [23] and it assumes an overhead of 4300 meters water equivalent. The expected number of background events will vary based on the depth and the geology of the specific repository location.

In this preliminary evaluation, the expected number of background events is almost a factor 10 larger than the number of signal events. To obtain a signal-to-noise ratio larger than 1, we estimate that the background reduction should have an efficiency of at least 92%. Methods of background reduction like e.g. using the directionality information to eliminate solar neutrinos and using a muon veto to reduce the cosmogenic background form the subject of our future research.

To understand the significance of the obtained detection rates, potential diversion scenarios were analysed.

4.2 Diversion Scenario

We assume that x % of the amount of radioactive waste was covertly diverted from the repository. At the same time, different data-taking times up to 24 months of continuous measurements were considered. The time required to detect a diversion of x % from the amount of radioactive waste with a certain confidence level was evaluated by hypothesis testing (the detection rate follows a Gaussian distribution, with a known standard deviation due to Poisson statistics).

The scenario was evaluated for two different times: year 2120 (Fig. 4) and year 2220 (Fig. 5).

It can be seen from Fig. 4 that, in year 2120, a 4% diversion can be detected with 95% confidence after about 12 months of data-taking. As expected, after another 100 years, the antineutrino detection rates decrease such that approximately a 14-15% diversion can be detected at a 95% confidence level.
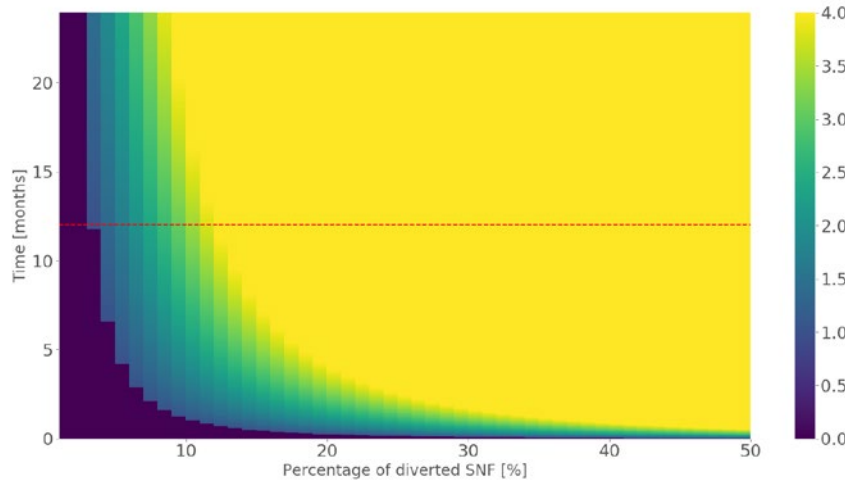
Figure 4: Results of the diversion hypothesis testing assuming that data-taking occurs in year 2120. The colour code shows the confidence level of the detection expressed in standard deviations. The dotted red line marks the detection time of 12 months.
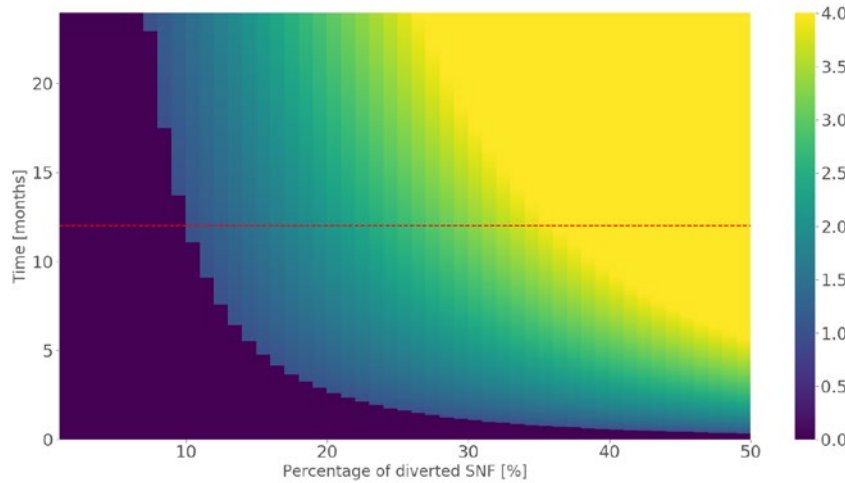
Figure 5: Results of the diversion hypothesis testing assuming the data-taking occurs in year 2220. The colour code shows the confidence level of the detection expressed in standard deviations. The dotted red line marks the detection time of 12 months.

The detection times can be reduced by choosing a larger detector volume. However, from layout considerations, detection times can be further reduced by deploying several - perhaps even smaller detectors - at different locations in the repository's proximity.

5. Conclusions and Outlook

As the quantity of radioactive waste increases worldwide, the potential risk of diversions in the context of unforeseeable societal and political events informs the necessity of safeguarding long-term geological repositories. The only messenger particles that could escape the confinement of the repository are the antineutrinos emitted decades later through the beta decays of isotopes like ^{90}Sr and ^{137}Cs still present in the waste. Presently, measuring the antineutrino emissions is the only approach that can offer direct information about the amount of radioactive waste present in the repository.

In this paper, we proposed the use of time projection chambers (TPCs) for measuring antineutrino emissions. For liquid argon, this technology is presently developed and validated by the neutrino physics community. More research and development work is required in order to demonstrate the feasibility of organic-liquid sensitive materials. Using time projection chambers to measure the antineutrino emissions presents several advantages in comparison to traditional detectors: (*i*) excellent track imaging capabilities – used for efficient background subtraction and locating where a potential diversion occurred, (*ii*) the absence of a kinematic threshold in the detection reaction which would otherwise limit the accessible antineutrino energy range and (*iii*) the relatively low production costs.

We performed a preliminary calculation of the expected event rate in LArTPCs and interpreted it in the context of a diversion scenario. We concluded that after 100 years since the closing of the geological repository a 4%

diversion can be detected within 12 months when using a single 80 t antineutrino detector. The required detection time increases with the age of the waste. Using several TPCs, placed at different locations in the vicinity of the repository, would significantly decrease the required detection time.

However, this evaluation assumes perfect detector efficiency and background rejection. A more realistic estimation of the detection and background rejection efficiencies could lead to an increased detection time. For a realistic feasibility study, the LArTPC performance should be studied in a full simulation that also takes the solar, cosmogenic and geoneutrinos background into account. This simulation together with a detailed treatment of the background forms the subject of our future studies.

6. Acknowledgements

7. References

[1] International Atomic Energy Agency, "Nuclear Technology Review," 2015. [Online]. Available: https://www.iaea.org/sites/default/files/ntr2015.pdf.

[2] International Panel on Fissile Materials, "Managing Spent Fuel from Nuclear Power Reactors," 2011. [Online]. Available: http://fissilematerials.org/library/rr10.pdf.

[3] D. Albright, S. Kelleher-Vergantini, D. Schnur, "Plutonium and Highly Enriched Uranium Inventories - Chapter 2," 2015. [Online]. Available: https://isis-online.org/uploads/isis-reports/documents/Civil_Plutonium_Stocks_Worldwide_March_14_2015_FINAL.pdf.

[4] International Atomic Energy Agency, "Monitoring of geological repositories for high level radioactive waste," 2001. [Online]. Available: https://inis.iaea.org/collection/NCLCollectionStore/_Public/32/018/32018325.pdf?r=1&r=1.

[5] V. Brdar, P. Huber, J. Kopp, "Antineutrino Monitoring of Spent Fuel," *Phys. Rev. Applied,* vol. 8, p. 054050, 2017.

[6] J. Leppänen et al, "The Serpent Monte Carlo code: Status, development and applications in 2013," *Ann. Nucl. Energy,* vol. 82, pp. 142-150, 2015.

[7] Nuclear Energy Agency, "Pressurised Water Reactor Main Steam Line Break Benchmark; Volume I: Final Specifications," 1999. [Online]. Available: https://www.oecd-nea.org/science/projects/benchmarks.html.

[8] A. Ohm, *private communication.*

[9] M. Askins et al, "The Physics and Nuclear Nonproliferation Goals of WATCHMAN: A WAter CHerenkov Monitor for ANtineutrinos," arXiv:1502.01132v1 [physics.ins-det], 2015.

[10] A. Haghighat et al, "Observation of Reactor Antineutrinos with a Rapidly-Deployable Surface-Level Detector," *Phys. Rev. Applied,* vol. 13, no. 3, p. 034028, arXiv:1812.02163v1 [physics.ins-det], 2018.

[11] R. Roncin, "From the measurement of the θ13 mixing angle to the search for geo-neutrinos: studying electron antineutrinos with Double Chooz and Borexino," *PhD Thesis - Université Paris Diderot (Paris 7) Sorbonne Paris Cité,* 2014.

[12] C. Rubbia, "The liquid-argon time projection chamber: a new concept for neutrino detectors," 1977. [Online]. Available: https://cds.cern.ch/record/117852?ln=en.

[13] T. Doke, K. Masuda, E. Shibamura, "Estimation of absolute photon yields in liquid argon and xenon for relativistic (1 MeV) electrons," *Nuclear Instruments and Methods in Physics Research Section A: Accelerators, Spectrometers, Detectors and Associated Equipment,* vol. 291, no. 3, pp. 617-620, 1990.

[14] C. Anderson et al, "The ArgoNeuT Detector in the NuMI Low-Energy beam line at Fermilab," *JINST,* vol. 7, no. P10019, 2012.

[15] R. Acciarri et al - The MicroBooNE Collaboration, "Design and Construction of the MicroBooNE Detector," *Journal of Instrumentation,* vol. 12, no. 2, pp. P02017--P02017, 2017.

[16] The DUNE Collaboration, https://www.fnal.gov/pub/science/lbnf-dune/index.html.

[17] W. J. Marciano, Z. Parsa, "Neutrino-Electron Scattering Theory," *J. Phys. G: Nuclear and Particle Physics,* vol. 29, no. 11, pp. 2629-2645, 2003.

[18] A. Strumia, F. Vissani, "Precise quasielastic neutrino/nucleon cross-section," *Physics Letters B,* vol. 564, no. 1-2, pp. 42-54, 2003.

[19] COHERENT Collaboration: D. Akimov et al., "First Detection of Coherent Elastic Neutrino-Nucleus Scattering on Argon," 2020. [Online]. Available: https://arxiv.org/abs/2003.10630.

[20] A. Suzuki, "Antineutrino science in KamLAND," *Eur. Phys. J. C,* vol. 74, p. 3094, 2014.

[21] DBE Tec - W. Bollingfehr et al, "Endlagerkonzepte - Bericht zum Arbeitspaket 5," no. pp. 78, 2012.

[22] F. Capozzi et al, "DUNE as the Next-Generation Solar Neutrino Experiment," *Phys. Rev. Lett.,* vol. 123, p. 131803, 2019.

[23] G. Zhu et al, "Developing the MeV potential of DUNE: Detailed considerations of muon-induced spallation and other backgrounds," *Phys. Rev. C,* vol. 99, no. 5, p. 055810, 2019.

[24] The COHERENT Collaboration - D. Akimov et al, "The COHERENT Experiment at the Spallation Neutron Source," arXiv:1509.08702v2 [physics.ins-det], 2016.

Validation of ORIGEN for VVER-440 Spent Fuel with Application to Fork Detector Safeguards Measurements

Jianwei Hu[1], Ian. C. Gauld[1], Stefano Vaccaro[2, a], Tapani Honkamaa[3], Germina Ilas[1]

[1]Oak Ridge National Laboratory, Oak Ridge, TN, USA
[2]European Commission, DG Energy, Euratom Safeguards Luxembourg, Luxembourg
[3]Radiation and Nuclear Safety Authority, Finland
Email: huj1@ornl.gov

Abstract:

The US Department of Energy National Nuclear Security Administration and the European Atomic Energy Community (Euratom) are collaborating with the Radiation and Nuclear Safety Authority in Finland to assess spent fuel verification methods for potential application to measurements at the planned spent fuel encapsulation plant and geological repository prior to final disposal in Finland. The fork detector (FDET) used to measure the neutron and gamma radiation from a given spent fuel assembly is an existing technology widely used by the International Atomic Energy Agency (IAEA) and Euratom for the safeguards verification of spent fuel operator declaration. Recently, an FDET data analysis software, referred to as the ORIGEN module, was developed and incorporated into the IAEA/Euratom Integrated Review and Analysis Program. This module uses the ORIGEN burnup code to calculate the nuclide concentrations and the neutron and gamma source terms in the spent fuel based on operator declarations. Then, to predict the expected FDET signals for a given fuel assembly, the module combines the source terms calculated by ORIGEN with FDET response functions that were pre-generated using MCNP models. The inspector can compare the calculated signals to the measured values in real time to identify possible anomalies in fuel assembly's operator declaration, integrity, or measurement. In this work, the capability of the ORIGEN module was extended from application to typical light water reactor fuels to use for VVER-440 assembly types. The accuracy of ORIGEN for this type of fuel assembly calculations was assessed by comparing calculated nuclide concentrations against destructive assay measurements for VVER-440 spent fuel. The performance of the ORIGEN module for FDET safeguards verification in routine inspections was assessed using FDET measurement data for 13 spent VVER-440 assemblies that were measured at the Loviisa Nuclear Power Plant in Finland, by comparing the calculated signals to the measured quantities. The results show that the calculated FDET neutron and gamma detector signals are generally within 12% of the measurements except for one assembly. These results are applicable to future safeguards verification in the planned Finland encapsulation plant, such as for passive neutron albedo reactivity safeguards measurements.

Keywords: spent fuel safeguards; Fork; FDET; ORIGEN; safeguards verification; encapsulation

1. Introduction

Finland is anticipated to be one of the first countries in the world to open a geological repository for permanent storage of spent nuclear fuel [1]. The US Department of Energy National Nuclear Security Administration and the European Atomic Energy Community (Euratom) are collaborating with the Radiation and Nuclear Safety Authority (STUK) in Finland on spent fuel safeguards verification methods that can be implemented prior to the fuel's encapsulation and geological disposal in Olkiluoto, Finland. STUK is working with the International Atomic Energy Agency (IAEA) and Euratom to finalize the spent fuel safeguards verification requirements and approaches for the planned encapsulation plant and repository [1]. The approaches to nondestructive assay (NDA) measurements for safeguards have evolved over time. Because there will be no spent fuel storage pools in the encapsulation plant, the plan is to perform passive gamma emission tomography (PGET) [2] and passive neutron albedo reactivity (PNAR) [3] safeguards measurements under water in the reactor site storage pools for safeguards verification, before transferring the fuel to the encapsulation plant. As one of the primary NDA instruments for spent fuel safeguards, the fork detector (FDET) [4] may be used for special inspections, for example, to re-establish continuity of knowledge of an assembly. The two options under consideration are (1) using PGET + PNAR and (2) using PGET + FDET. PGET measures gamma rays emitted from a given assembly in multiple angular positions around the vertical axis using directionally collimated gamma detectors, in order to reconstruct a cross-sectional image of the assembly to

verify the presence of the rods in the assembly. FDET measures the total neutron and gamma emissions from an assembly [4]. The IAEA and Euratom have used FDET routinely for spent fuel safeguards verification globally since the 1990s. PNAR is similar to FDET in that it also measures total neutron and gamma emissions, but it can also quantify the assembly's neutron multiplication—an indicator of fissile content—using measurements with and without a cadmium liner neutron absorber around the assembly. The combined measurements of PGET + FDET or PGET + PNAR can be used to verify both the integrity of a given fuel assembly and the operator declarations—two primary goals for spent fuel safeguards.

Given the complexities of tracking nuclide transmutations during irradiation and decay and predicting neutron and gamma source terms in a spent fuel assembly, simulations using sophisticated computer codes are generally needed to accurately predict the NDA signals from a spent fuel assembly measurement for safeguards verification. Oak Ridge National Laboratory (ORNL) and Euratom have collaborated to develop a data analysis module for FDET, to fully automate the prediction of neutron and gamma detector signals using operator declarations of a spent fuel assembly [4] [5], with a specialized module resulting from this effort. Such predictions can help the safeguards inspector to draw conclusions in real time on whether the operator declarations of a given fuel assembly are consistent with the measured signals. The new module, referred to as *the ORIGEN module* in this paper, is based on the ORIGEN isotope generation and decay code [6] and incorporates detector response functions developed using MCNP [7] models of the assembly and detector configuration. The ORIGEN module has been incorporated into the Integrated Review and Analysis Program (IRAP) software that is jointly developed and maintained by IAEA and Euratom. The ORIGEN module has been extensively benchmarked for typical pressurized water reactor (PWR) and boiling water reactor (BWR) assembly types [4] [5], but has not been benchmarked for VVER-440 assembly types, as FDET measurement data on those types of assemblies are scarce. In this work, the ORIGEN module's application was extended to VVER-440 assembly types by generating new ORIGEN reactor cross-section libraries, referred to as *ORIGEN libraries* in this paper, and new FDET response functions to support potential applications to the Loviisa reactors in Finland. This paper establishes ORIGEN's accuracy in predicting the fissile and radiation-emitting nuclides in VVER-440 fuel and applies the ORIGEN module to evaluate FDET measurements of 13 spent VVER-440 assemblies at the Loviisa Nuclear Power Plant.

2. VVER-440 assembly designs

VVER-440 fuel assemblies are used in two reactors in Finland and in several eastern European countries. The VVER-440 assembly has 126 fuel rods arranged in a hexagonal lattice, with one central tube that does not contain fuel. There are two basic types of VVER-440 assemblies: standard assemblies and control assemblies with fuel followers. The top section of such control assemblies contain neutron absorbing materials, and the bottom section contains fuel. These control assemblies move vertically in the core, with the follower section of the assembly displacing the control section as the assembly is moved upward in the core. The fuel followers have a slightly shorter active fuel length of 2,320 mm compared to 2,420 mm for standard assemblies, and therefore they contain less uranium. Since FDET measurements are usually performed near the center of the assembly—away from the ends and away from the control element—control assemblies are treated as standard assemblies for the purpose of burnup analysis.

The TVEL Fuel Company (TVEL), a Russian fuel supplier, manufactured assemblies for the Loviisa reactors with initial enrichments of 1.6, 2.4, and 3.6 wt% ^{235}U [8] and a uniform enrichment distribution (i.e., all fuel rods in an assembly have the same enrichment). These enrichments are widely used in other VVER-440 plants. The general design characteristics of the TVEL VVER-440 assembly design are listed in Table 1.

Description	Parameter value
Lattice pitch type	Triangular
Number of fuel rods	126
Number of non-fuel rods	1
Inner fuel pellet radius (cm)	0.075
Fuel pellet radius (cm)	0.3783
Cladding inner radius (cm)	0.388
Cladding outer radius (cm)	0.455
Fuel rod pitch (cm)	1.22
Fuel assembly pitch (cm)	14.70

Table 1: VVER-440 TVEL assembly design data [8].

At higher enrichments, the designs can use either uniform enrichment or enrichment profiling, whereby the fuel rods may have different enrichments, with lower enrichment rods generally located near the periphery of the assembly. These higher enrichment assemblies may have some fuel rods that contain burnable absorbers such as gadolinium. Prior to 2009 Loviisa Nuclear Power Plant operated with a first-generation TVEL design for standard assemblies, with 4.0 wt% ^{235}U enrichments without profiling or gadolinium absorbers, and with a second-generation fuel follower design (see Section 3 for details). Since 2009, the Loviisa has operated with a second-generation TVEL design with a radially profiled enrichment and six gadolinium absorber rods [8] in the fuel assembly. Fuel assemblies manufactured by British Nuclear Fuels Limited (BNFL)/Westinghouse have also been operated in Loviisa, with uniform enrichments of 3.7 and 3.8% without profiling [8]. While the

Westinghouse assembly design is similar to that of TVEL, the fuel rod diameter is slightly smaller, and the fuel rod pellets do not have a central hole to accommodate swelling and fission product gases.

3. Generation of origen libraries for Loviisa assembly designs

ORIGEN libraries are required for standalone ORIGEN calculations to predict the nuclide concentrations and neutron and gamma source terms in nuclear fuel following its irradiation and decay. These ORIGEN libraries can be pre-generated using the TRITON depletion sequence in SCALE [9] to create one-group neutron cross sections for the fuel as functions of assembly design, moderator density, fuel enrichment, and fuel burnup. A large array of libraries for various fuel assembly types is included in the standard SCALE code package [9]. ORIGEN libraries for some of the VVER TVEL designs used at Loviisa are available in the SCALE distribution, but several other VVER designs used at Loviisa are not available, including BNFL/Westinghouse designs and TVEL designs with 4.0 and 4.37% enrichments, as shown in Table 2.

New ORIGEN libraries were generated in this work for all of the VVER-440 assembly types shown in Table 2. ORIGEN libraries for the VVER-440 assembly types existing in SCALE were regenerated to maintain consistency, by using the same set of nuclear data to prevent potential biases caused by different sets of nuclear data. The most recent version of the SCALE code package (version 6.2.3) [9] was used. The ORIGEN libraries were generated with the TRITON depletion sequence in SCALE with two-dimensional (2D) models of the fuel assemblies. TRITON iteratively couples the 2D neutron transport code NEWT with ORIGEN [9]. Under TRITON, the neutron spectrum calculated by NEWT is used to collapse the multigroup neutron cross sections into one-group cross sections, which ORIGEN uses to calculate reaction rates and the time-dependent evolution of nuclide compositions during irradiation and decay. The SCALE 252-group neutron cross section library, used in these TRITON calculations, contains cross sections for more than 400 nuclides, most of which are from ENDF/B-VII.1 [10] with the remainders from JEFF-3.1/A activation libraries [11]. The collapsed one-group cross sections that are calculated when running TRITON are automatically saved as ORIGEN library files for future standalone burnup-dependent ORIGEN calculations. Standalone ORIGEN calculations take only a small fraction of the computation time required for a TRITON calculation.

Figure 1 shows the TRITON models developed in this work for three different VVER-440 assembly designs used in Finland: (a) the TVEL design with flat enrichment profile (first generation); (b) the TVEL design with profiled enrichment (second generation); and (c) the BNFL/Westinghouse NOVA-E3 design with flat enrichment. In Figure 1 (b), the corner rods have lower enrichments and the green colored rods contain gadolinium as a burnable absorber. The central holes in each rod of the TVEL designs are shown in this figure.

Designs	Enrichment(s) (wt% ^{235}U)	Profile
Assembly designs with libraries available in SCALE		
TVEL	1.6, 2.4, 3.6	Flat
TVEL	3.82 (avg.*)	Profiled
TVEL	4.25 (avg.)	Profiled
TVEL	4.38 (avg.)	Profiled
Assembly designs with libraries not available in SCALE but used at Loviisa Nuclear Power Plant		
TVEL standard	4.0	Flat
TVEL Gen-II	4.0	Flat
TVEL Gen-II	4.37 (avg.)	Profiled
BNFL/Westinghouse NOVA E-3	3.7, 3.8	Flat

*average of radially varying enrichment across an assembly

Table 2: VVER-440 assembly designs for ORIGEN libraries [8] [9].
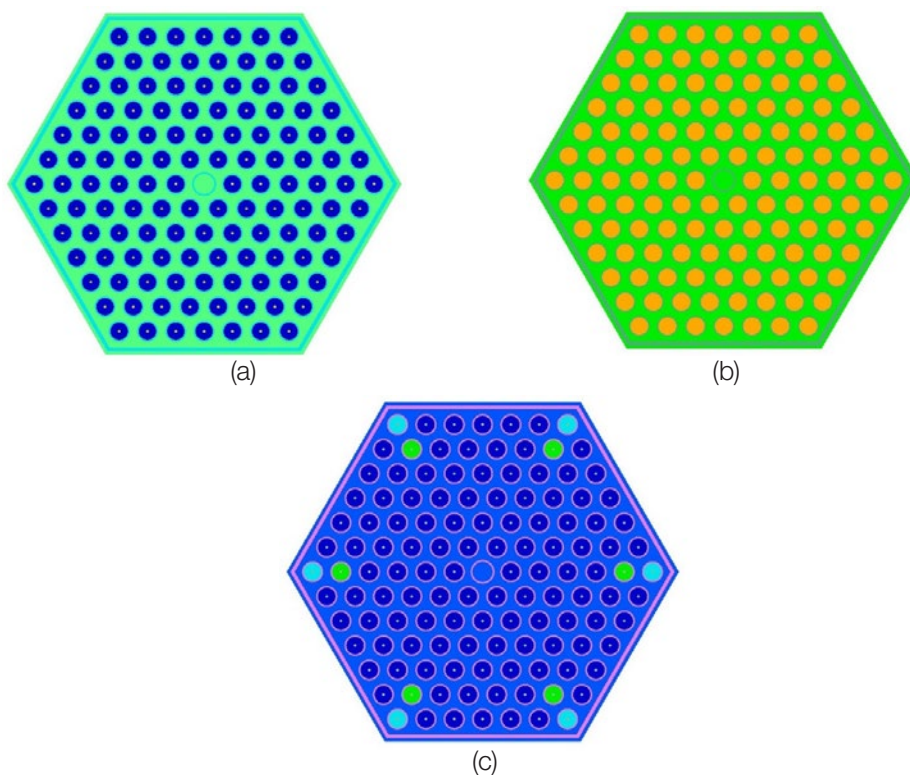
Figure 1: TRITON models of VVER-440 assembly designs: (a) TVEL design with flat enrichment; (b) the TVEL design with profiled enrichment **[8]**; (c) BNFL/Westinghouse NOVA-E3 design with flat enrichment.

4.   Experimental data on nuclide concentrations

It is important to validate the new VVER-440 ORIGEN libraries with measurement data before using them for nuclear safety and safeguards applications. Since the NDA safeguards measurements of spent fuel are mostly performed on individual fuel assemblies, and the ORIGEN calculations using the ORIGEN libraries are designed for assembly-average nuclide concentrations, the ideal measurement data on nuclide concentrations for validation would be on an assembly level as well, e.g., an individually reprocessed assembly; however, such data are not available in the public domain for VVER-440 assemblies.

Measurements of nuclide concentrations in VVER-440 spent fuel samples reported in literature that were performed using destructive assay (DA) in Russia are used as a benchmark dataset in this work. The samples were usually small axial segments (~1 cm long) cut from spent fuel rods, then dissolved in acid solutions and prepared for radiochemical analysis. The concentrations of important nuclides were measured using various techniques, including mass spectrometry and gamma spectroscopy [12]. Many of these measurements were compiled into the international database of spent fuel compositions [13] hosted and maintained by the Organisation of Economic Cooperation and Development/Nuclear Energy Agency [14]. This database, called the Spent Fuel Isotopic Composition (SF-COMPO), was compiled with the contributions and cooperation of many countries. Early efforts to compile and

upload VVER-440 and VVER-1000 data [15] included DA data from three VVER-440 reactors operated in Russia: Kola-3, Novovoronezh-3 (Novo-3), and Novovoronezh-4 (Novo-4). A total of 47 spent fuel samples were measured from 5 different fuel assemblies. The samples cover initial enrichment values ranging from 3.3 to 4.38% ^{235}U. Measurements for all samples include uranium and plutonium isotopes and ^{244}Cm, a major neutron-emitting source. Measurements of ^{137}Cs and ^{154}Eu, both major gamma emitters and frequently used as burnup indicator nuclides, were available for 20 samples (Kola-3 samples).

A summary of the VVER-440 measurement data is provided in Table 3, along with the main fuel characteristics [16] [17] [18]. The locations of the measured fuel rods in the assembly were determined from the fuel rod identification as shown in Table 3, and the schematic of the assembly layout is shown in Figure 2. The rod locations can be important since the rods adjacent to the central instrument tube and at the assembly periphery could be subject to more moderated neutronic environment compared to other rods, which would affect the nuclide concentrations. Larger deviations might be expected for these peripherical samples since they are less representative of the assembly average. Samples located near the periphery or instrument tube are highlighted in Table 3. The rod locations are color coded in this figure, with each color representing samples from the same reactor, and the same color coding is used in the figures in later of this section. Positions 25, 63, and 69 were used by samples from two reactors and therefore they were double colored.

Sample[a] #	Reactor	Assembly	Fig. 2 fuel rod ID	Sample ID	Sample burnup (GWd/tU)[b]	Sample enrichment (wt% 235U)	Cooling time[c] (year)	Axial Elevation[d] (mm)
1	Kola-3	144-46879	96	5	35	4.38	7.3	66
2	Kola-3	144-46879	61	13	47.9	4.37	7.3	185
3	Kola-3	144-46879	61	53	62.7	4.37	7.3	825
4	Kola-3	144-46879	96	63	51.2	4.38	7.3	196
5	Kola-3	144-46879	61	76	42.3	4.37	7.3	108
6	Kola-3	144-46879	62	81	31.8	4.38	7.3	44
7	Kola-3	144-46879	96	98	58.3	4.38	7.3	355
8	Kola-3	144-46879	61	124	32.7	4.37	7.3	43
9	Kola-3	144-46879	62	165	40.8	4.38	7.3	107
10	Kola-3	144-46879	96	169	40.8	4.38	7.3	109
11	Kola-3	144-46879	61	189	57.6	4.37	7.3	314
12	Kola-3	144-46879	96	718	61.4	4.38	7.3	549
13	Novo-3[e]	RP-3371A	63	1	17.1	3.3	3.3	1875
14	Novo-3	RP-3371A	97	2	14.2	3.3	3.3	2170
15	Novo-3	RP-3371A	97	3	8.7	3.3	3.3	200
16	Novo-3	RP-3371A	58	4	13.4	3.3	3.3	200
17	Novo-3	RP-3371A	63	5	13.9	3.3	3.3	375
18	Novo-3	RP-3371A	97	6	11.7	3.3	3.3	300
19	Novo-3	RP-3371A	97	7	11.5	3.3	3.3	300
20	Novo-4f	13602496	7	18	42.7	3.6	4.0	875
21	Novo-4	13602496	25	19	43.5	3.6	4.0	875
22	Novo-4	13602496	30	20	37.2	3.6	4.0	875
23	Novo-4	13602496	52	21	37.2	3.6	4.0	875
24	Novo-4	13602496	66	22	39.2	3.6	4.0	875
25	Novo-4	13602496	69	23	44	3.6	4.0	875
26	Novo-4	13602496	91	24	39.7	3.6	4.0	875
27	Novo-4	13602496	94	25	39.4	3.6	4.0	875
28	Novo-4	13602496	98	26	37.6	3.6	4.0	875
29	Novo-4	13602496	123	27	41.8	3.6	4.0	875
30	Novo-4	213	25	10	38.7	3.6	3.3	1625
31	Novo-4	213	25	11	38.2	3.6	3.3	625
32	Novo-4	213	25	12	38.2	3.6	3.3	1125
33	Novo-4	213	25	8	21	3.6	3.3	2285
34	Novo-4	213	25	9	27.6	3.6	3.3	125
35	Novo-4	213	63	16	32.6	3.6	3.3	1875
36	Novo-4	213	63	17	33.1	3.6	3.3	375
37	Novo-4	213	64	13	22	3.6	3.3	2225
38	Novo-4	213	64	14	20.4	3.6	3.3	125
39	Novo-4	213	64	15	34.9	3.6	3.3	1625
40	Novo-4	13626135	65	182	22.86	3.592	12.4	100
41	Novo-4	13626135	65	21	41.5	3.592	12.4	1000
42	Novo-4	13626135	65	69	31.32	3.592	12.4	2150
43	Novo-4	13626135	67	149	41.9	3.585	12.4	1000
44	Novo-4	13626135	68	162	44.2	3.585	12.4	1000
45	Novo-4	13626135	69	135	29.9	3.592	12.4	100
46	Novo-4	13626135	69	57	36.2	3.592	12.4	2150
47	Novo-4	13626135	69	79	46.3	3.592	12.4	1000

[a]Shaded rows indicate samples located at periphery assembly locations or adjacent to the central instrument tube

[b]GWd/tU = Gigawatt-days per ton of uranium

[c]The time from the fuel was discharged from the reactor to when the measurement was done

[d]Sample location from the bottom of the active fuel region

[e]Novovoronezh-3

[f]Novovoronezh-4

**Table 3:** Measured VVER-440 spent fuel samples [16] [17] [18].
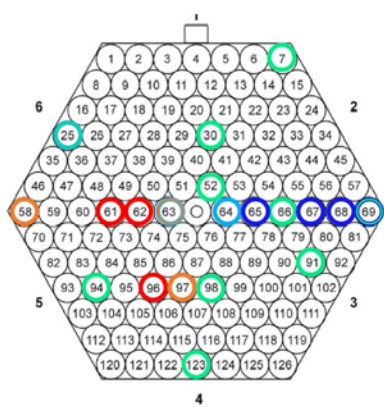
Figure 2: Schematic showing the arrangement of fuel rod identifiers in the VVER-440 assemblies and locations of measured rods; each color represents samples from a specific reactor. The assembly alignment/orientation notch is shown on side 1 (see the 1-6 numbers outside the assembly).

Problems were previously identified for the DA measurement of some nuclides from the Kola-3 assembly 144-46879 [19]. The present analysis of the data, previous independent analyses [19], and comparisons of the Kola-3 measurements with other similar VVER-440 fuels, suggest a systemic under-reporting of measured plutonium by ~ 18%, a value derived from the average bias in $^{238-242}$Pu for all 12 Kola-3 samples. This bias is observed in all isotopes of plutonium and is likely attributed to problems in the chemical separations process or the reference standards used in the measurements. Consequently, the data for all plutonium isotopes in these Kola-3 samples were adjusted to correct for the observed bias.

The comparisons of nuclide concentrations presented in this paper were focused to the nuclides of primary importance to spent fuel safeguards—namely, ^{235}U, ^{238,239,240,241}Pu, ^{244}Cm, and ^{137}Cs—although results for other nuclides, including ^{236}U, ^{238}U, ^{242}Pu, ^{242}Cm, and ^{134}Cs, are summarized in Table 4.

The ^{235}U results are shown in Figure 3. Note the same color coding as in Figure 2 is used here. The percentage values in parentheses in the legend are the initial enrichments of the samples. DA measurements are shown with error bars corresponding to the 95% confidence level, and calculations are shown as colored square symbols. Samples from the same assembly use the same color. The results show bands that are correlated to the different initial enrichments of the fuel rods—nominally 3.3, 3.6, and 4.4 wt % ^{235}U. The calculated results reside within the measurement and uncertainty bands for most of the samples, and they trend consistently with burnup. There is a general trend to overestimate ^{235}U in samples of the Novo-4 assemblies; this trend is not observed in Kola-3 or Novo-3 data. Many of the Novo-4 samples were taken from rods located at the periphery of the assembly, and larger deviations for these samples are expected. This overprediction is likely directly related to an overprediction in ^{239}Pu for these same samples (see Figure 5) that is consistent with the rod position in the assembly. The periphery rods are generally subject to a more thermal, moderated neutron environment due to the additional water at the assembly gap, resulting in less plutonium production compared to the harder neutron spectrum in the assembly interior rods. These ORIGEN calculations were based on assembly average conditions, which are closer to the conditions experienced by the interior rods. Thus, the ORIGEN calculations will overpredict the plutonium concentrations for the Novo-4 samples from the periphery of the assembly. The overestimation of ^{239}Pu leads to increased ^{239}Pu fission, and consequently, it leads to less ^{235}U consumption due to fission, resulting in an overestimation of the remaining ^{235}U for these locations. For example, the Novo-4 sample with the highest burnup of 46.3 GWd/tU located at the corner of the assembly (rod #69) saw the largest overestimation of ^{235}U, as represented by the rightmost blue square in Figure 3.
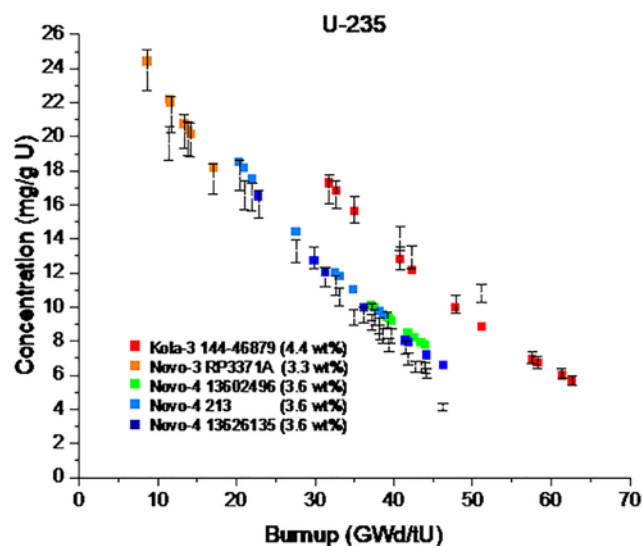
Figure 3: Comparison of measured (error bars) and calculated (color squares) ^{235}U concentration in VVER-440 spent fuel samples.

The results for the plutonium isotopes [238]Pu, [239]Pu, [240]Pu, and [241]Pu are shown in Figure 4 through 7, respectively. Note the same color coding as in Figure 2 is used in these figures. The calculated nuclide concentrations were in generally good agreement with measurements for all Pu isotopes. The overprediction of [239]Pu in many of the Novo-4 samples was consistent with the fuel rod locations, as discussed previously. Note that the enrichment band positions for the [241]Pu results are also affected by different cooling times of the measurements. As shown in Table 3, the Novo-4 13626135 samples had much longer cooling times than the other Novo-4 samples, which resulted in lower [241]Pu concentrations in the Novo-4 13626135 samples than the other Novo-4 samples due to the extra decay of [241]Pu, even though they had the same initial enrichments of 3.6%. Plutonium-241 has much shorter half life than the other three Pu isotopes studied here and it is more sensitive to differences in cooling times.

Results for [244]Cm, the dominant neutron source in spent fuel with a relatively long cooling time (>2 years), are shown in Figure 8. Measurement uncertainties were generally much larger for curium isotopes than for the uranium and plutonium isotopes because of different measurement techniques used [20]. The results show that the calculations trend well with burnup and most of the measurement data. Accumulation of [244]Cm in spent fuel is generally considered to trend to the ~4th power of burnup, which was consistent with the calculation results and measurement data included in this figure.
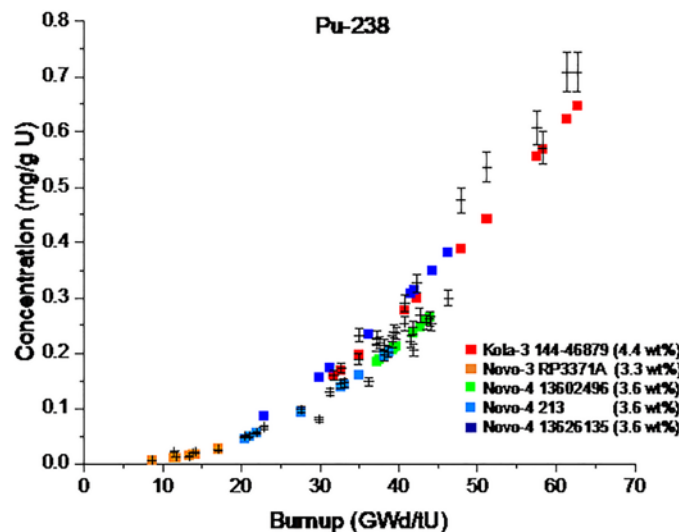
Figure 4: Comparison of measured (error bars) and calculated (color points) [238]Pu concentration in VVER-440 spent fuel samples.
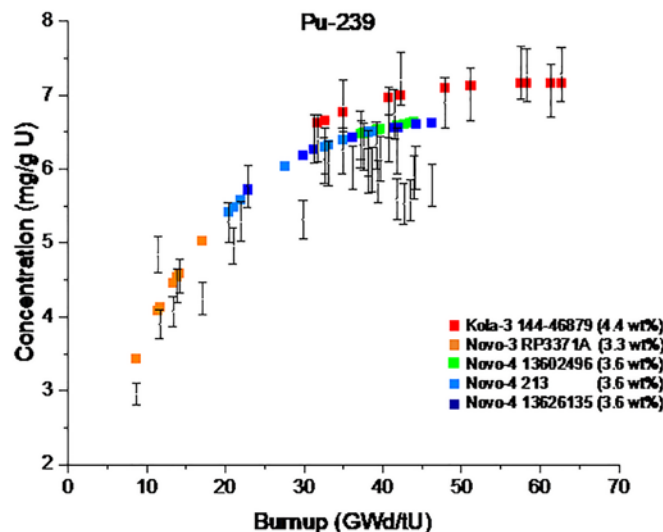
Figure 5: Comparison of measured (error bars) and calculated (color points) [239]Pu concentration in VVER-440 spent fuel samples.
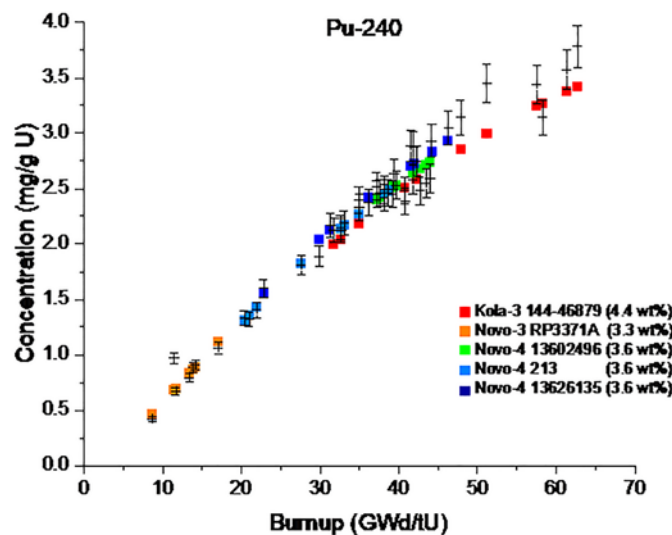
Figure 6: Comparison of measured (error bars) and calculated (color points) [240]Pu concentration in VVER-440 spent fuel samples.
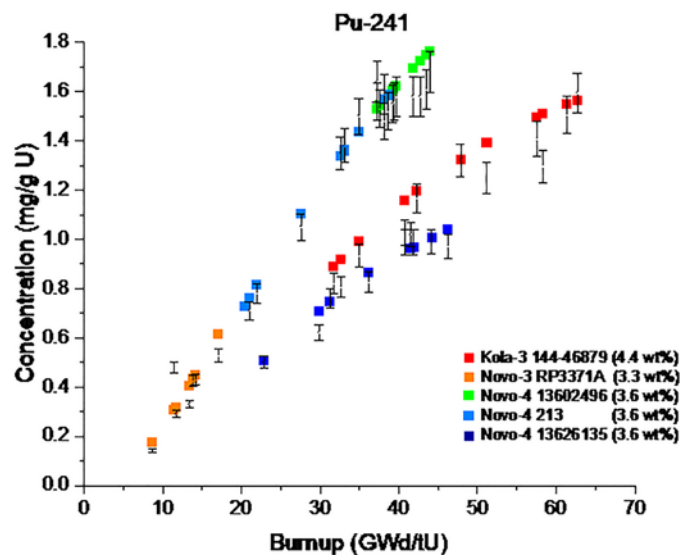
Figure 7: Comparison of measured (error bars) and calculated (color points) [241]Pu concentration in VVER-440 spent fuel samples.
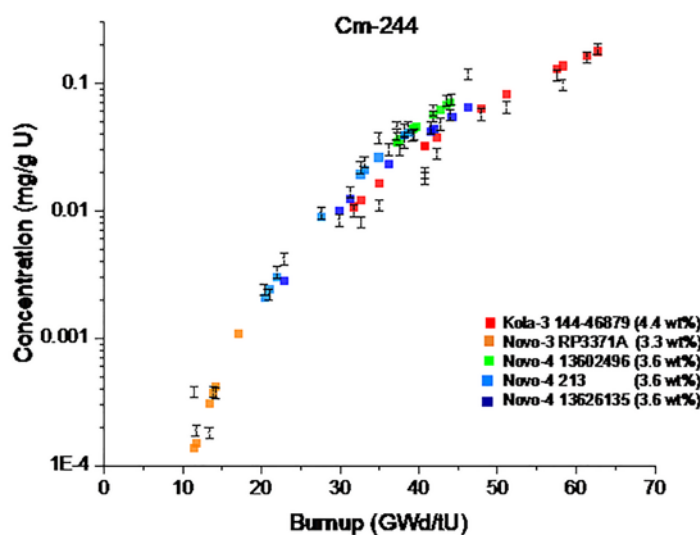
Figure 8: Comparison of measured (error bars) and calculated (color points) [244]Cm concentration in VVER-440 spent fuel samples.

Fission products are the primary gamma emission sources in spent fuel, with the nuclides ^{137}Cs, ^{134}Cs, and ^{154}Eu being dominant for gamma NDA measurements at longer cooling times (> 5 years). Measurements of ^{134}Cs and ^{154}Eu were available for the Kola-3 samples but were not considered due to likely errors in measured values from incorrect decay time corrections. Cesium-137 has a half life of ~30 years, which is much longer than that of ^{134}Cs or ^{154}Eu and is less sensitive to decay time corrections. The results for ^{137}Cs using available data are shown in Figure 9. Calculated values were generally within the estimated relative measurement error of typically ±5%. As shown in Table 3, the Novo-4 13626135 samples had much longer cooling time than that of Kola-3, which resulted in less ^{137}Cs in

Novo-4 13626135 samples than in Kola-3 samples due to the extra decay of ^{137}Cs.

To provide a quantitative assessment of ORIGEN library performance, the mean and standard deviation of the difference between measurements and calculations of nuclide concentrations are summarized in Table 4. Several samples were removed due to very large deviations compared to other samples in the measurement set. Specifically, Novo-3 sample RP-3371A-97-7 (#19) and Novo-4 sample 13626135-69-79 (#47) were removed from the statistical analysis since the deviations for many of the major actinides exceeded three standard deviations (3σ) for the population of data for the other samples.
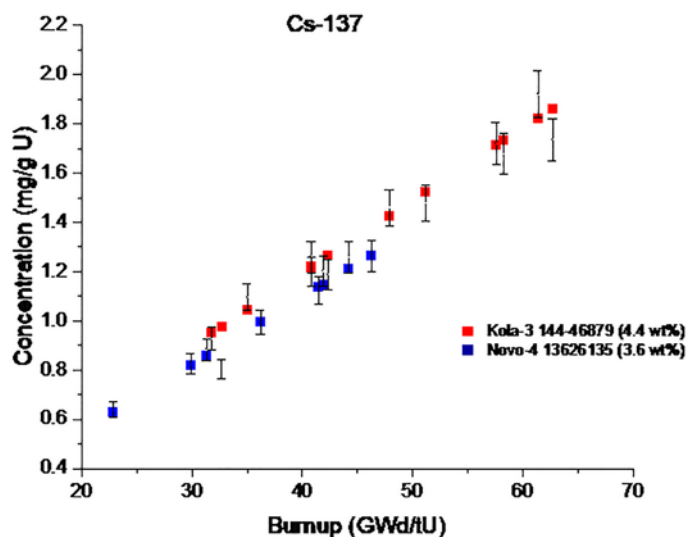
**Figure 9:** Comparison of measured (error bars) and calculated (color points) ^{137}Cs concentration in VVER-440 spent fuel samples.

Nuclide	Measurements #	Mean	Standard deviation
^{235}U	45	6.1%	8.9%
^{236}U	45	-3.1%	6.0%
^{238}U	45	-0.4%	0.3%
^{238}Pu	38	-5.9%	8.2%
^{239}Pu	44	5.7%	6.3%
^{240}Pu	45	-0.8%	5.1%
^{241}Pu	44	5.3%	7.0%
^{242}Pu	44	-0.9%	8.9%
^{242}Cm	12	1.2%	29.5%
^{244}Cm	43	7.5%	27.3%
^{134}Cs	19	14.4%	20.7%
^{137}Cs	19	0.8%	6.2%

Mean and standard deviation are calculated as and $\text{Mean} = \frac{1}{N}\sum_{k=1}^{N}\left(\frac{C}{M}-1\right)_k$ $\left\{\frac{1}{N-1}\sum_{k=1}^{N}\left[\left(\frac{C}{M}-1\right)_k - \text{Mean}\right]^2\right\}^{1/2}$, where N is total number of measurements, k is each sample, C is the calculated nuclide concentration, and M is the measured concentration.

Table 4: Statistical analysis of nuclide predictions.

The mean deviation between calculations and measurements (bias) was less than 8% for most nuclides, except for [134]Cs probably due to its shorter half life and higher sensitivity to errors in decay time corrections. Similarly, the relative standard deviation (bias uncertainty) was less than 9% for the uranium and plutonium isotopes. Larger uncertainties were seen for the curium isotopes.

Calculations were performed using VVER-440 fuel assembly libraries that were developed to predict assembly average nuclide concentrations. However, measurements were performed on small samples from individual rods. Such inconsistency is avoided in a spent fuel safeguards practice because the NDA measurement and the ORIGEN calculations are performed on individual assemblies. Conversely, for predicting NDA signals using the ORIGEN modules, the uncertainties in the calculated nuclide concentrations contribute to only part of the overall uncertainties. Other factors, such as the detector response and multiplications in the assembly, also play a role, as discussed in the subsequent sections.

To assess the performance of the ORIGEN module's capability in predicting the FDET signals from VVER-440 assemblies, FDET measurement data were collected. FDET models were developed for these fuel types, and the calculated results of the ORIGEN module were compared to the measurement data, as discussed in the following three sections.

5. Loviisa measurement campaign

FDET measurements were performed on 13 VVER-440 assemblies at the Loviisa Nuclear Power Plant in February 2017 using a standard Euratom BWR FDET. The characteristics of the measured assemblies are summarized in Table 5. Assemblies from Loviisa units 1 and 2 were included in the measurements. All the measured assemblies operated in contiguous reactor cycles (i.e., they were not unloaded for one or more cycles before being reinserted in the core for further irradiation) except for assembly #1, which was out of the core during cycle 24.

6. FDET MCNP models for VVER-440

The FDET measurement configuration of the VVER-440 assemblies in the Loviisa spent fuel pool was modeled using MCNP to calculate the expected FDET signals (neutron counts and gamma current) as a function of emitted neutron/photon particle energy in the fuel. This calculation requires modeling the fuel assembly, the FDET instrument, and the pool water, including the soluble boron concentration used in most pools containing PWR fuel like VVER-440. The boron concentration was based on criticality safety considerations and is not necessarily constant, although levels are usually within a well-defined range. The Loviisa pools operate with a boron level of 13–15 g boric acid $(B(OH)_3)$ per kilogram of fresh water [3]. Consistent with previous studies of the PNAR instrument [3], an average value of 14 g/kg was used in the current work, corresponding to a 2,450 ppm boron concentration.

The MCNP models for the VVER-440 assembly measurement configuration and details of the neutron/gamma detectors of the FDET are illustrated in Figure 10. The FDET used in the Loviisa measurement campaign was designed for BWR assembly types and has an internal width (opening) of 168 mm and a depth of 178 mm. The VVER-440 assembly outer dimensions are 145 mm (flat-to-flat) by 167 mm (diagonal). To avoid jamming the assembly in the FDET opening, the measurements were performed with the assembly rotated as shown in Figure 10.

ID	Fuel type	Enrichment (wt %)	Reactor cycles	Burnup (MWd/tU)	Cooling time (days)
1	BNFL modified	3.8	22, 23, 25	38,342	5,390
2	BNFL modified	3.8	22, 23, 24, 25	43,685	5,390
3	TVEL standard	3.6	15	5,716	8,120
4	TVEL standard	3.6	13, 14, 15	38,710	7,917
5	TVEL standard	4.37	33, 34, 35, 36	50,166	1,343
6	TVEL fuel follower	4.0	34, 35, 36	41,114	1,343
7	BNFL standard	3.7	32, 33, 34	40,068	2,071
8	TVEL standard	3.6	19, 20, 21	39,339	6,832
9	TVEL standard	3.6	24, 25, 26	41,749	5,012
10	TVEL standard	3.6	10, 11, 12	38,233	9,044
11	TVEL standard	3.6	13, 14, 15	39,635	7,917
12	TVEL standard	3.6	22, 23, 24	39,763	5,733
13	TVEL standard	4.37	31, 32, 33, 34	48,568	980

Table 5: Characteristics of measured VVER-440 assemblies.
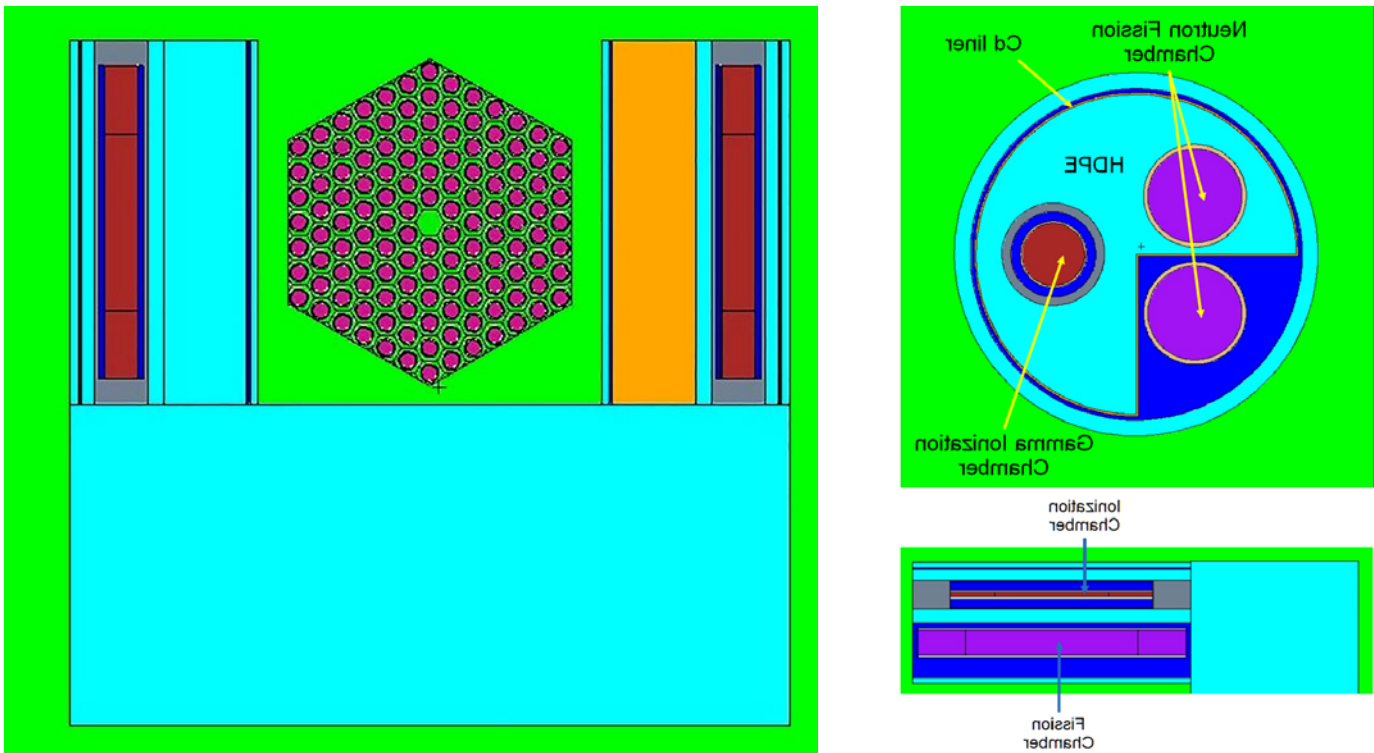
Figure 10: MCNP models of the FDET measurement of an VVER-440 assembly: (Left) the horizontal cross sectional view of the measurement configuration; (Right) the horizontal and vertical cross sectional views of one of the two tines of the FDET.

The FDET response functions were generated based on each of the neutron/photon source particle histories. For the FDET neutron response functions, 20 discrete source neutron energies ranging from 0.01–20 MeV were modeled, with one energy modeled in a separate MCNP model. Since most neutrons are born at ~2 MeV in spent fuel, the used neutron energy discretization was deemed sufficient. Similarly, the FDET gamma response functions and 18 discrete source photon energies ranging from 0.1–10 MeV were modeled. For the neutron/photon source particle energies that fell between the discretized energies, the response functions were interpolated by the ORIGEN module. In each MCNP model, a fixed-source calculation was performed using MCNP5 version 1.6 [7], with the source particles sampled uniformly in the horizontal direction of the fuel assembly but nonuniformly in the axial direction based on the calculated neutron/photon emission probability to account for the axial burnup variations. A number of 3E8 particle histories were used in the MCNP calculations, which took the neutron models 5,000–10,000 minutes to complete on a single processor, depending on which source energy was used, resulting in < 0.3% uncertainties in the calculated neutron response functions for most energies. For the photon models, it took 200–300 minutes to complete, resulting in < 1% uncertainties for the majority of energies. For the neutron signals, the fission rates in the U_3O_8 coating layers of the fission chambers were calculated, whereas the gamma dose rates in the active gas of the ionization chambers were calculated for the gamma signals. The calculated response functions are listed in Table 6.

MeV	Gamma (×10⁻¹⁰)
0.1	0.001809
0.2	0.031539
0.3	0.092311
0.4	0.17800
0.5	0.27808
0.6	0.39391
0.7	0.51901
0.8	0.64721
0.9	0.78029
1.0	0.91562
1.2	1.18221
1.4	1.44747
1.6	1.68525
1.8	1.92923
2.0	2.15605
3.0	3.14516
5.0	4.68432
10.0	7.97987

MeV	Neutron-A (×10⁻³)	Neutron-B (×10⁻³)
0.01	0.73999	1.0554
0.03	0.76293	1.1244
0.06	0.77571	1.1668
0.1	0.78218	1.2083
0.2	0.79549	1.2756
0.4	0.79545	1.3309
0.6	0.79105	1.3850
0.8	0.77850	1.4052
1.0	0.77355	1.4042
2.0	0.72734	1.4108
3.0	0.67843	1.3437
4.0	0.64998	1.3084
5.0	0.59511	1.2095
6.0	0.59326	1.2092
7.0	0.59687	1.2046
8.0	0.61800	1.2332
9.0	0.60591	1.2156
10.0	0.60043	1.1999
14.0	0.61924	1.2397
20.0	0.67253	1.3303

Neutron-A = Fission chamber (bare)

Neutron-B = Fission chamber (with cadmium liner)

Table 6: FDET response functions for VVER-440 fuel.

7. Results of calculated and measured FDET signals

The FDET neutron/gamma signals for the 13 measured VVER-440 assemblies were also calculated using the ORIGEN module with the new VVER-440 libraries and the FDET response functions that were generated in this work. The module used the ORIGEN code to calculate the assembly average nuclide concentrations, the infinite neutron multiplication factor of the fuel (k_∞) used to account for subcritical neutron multiplication, and the neutron/photon emission rates in each energy group from a given VVER-440 spent fuel assembly using the cycle-average irradiation histories provided by the operator. The module also combined the neutron/photon emission rates with the detector response functions to predict the FDET neutron/gamma signals for each fuel assembly. Before the predicted signals were compared against the measured ones, several additional data processing procedures were implemented, as discussed below.

Previous studies have indicated that the LND ionization chamber (Model 52110) used in the Euratom FDET exhibits a nonlinear response to the gamma dose rate [4]. To account for this, the calculated gamma signals in this work were further modified using an empirical correlation developed in the previous work [5] with a power coefficient of 0.77. The calculated neutron count rates were also modified to account for the neutron multiplication [5] of a given assembly using the infinite neutron multiplication factor for the fuel (k_∞) calculated by ORIGEN and the neutron leakage factor (L) predetermined by MCNP for a particular fuel assembly design. The L factor was set to 0.765 given the 2,450 ppm boron concentration in the pool; it would have been 0.626 if there were no boron in the pool.

An absolute calibration factor was not available for these assemblies. Instead, the ratio of the measured average signal to the calculated average was used to scale the calculated signals in each fuel assembly in the set to account for factors that were not considered (e.g., electronic efficiency, conversion of gamma instrument current to gamma signal) in the ORIGEN calculations or by the response functions. Calibration factors can be developed using measurement data collected by the same FDET instrument at the same spent fuel pool.

With these modifications, the calculated FDET neutron/gamma signals were compared to the measured values for all 13 assemblies. Table 7 summarizes these results and lists the calculated neutron multiplication of the assemblies as determined using the k_∞ from ORIGEN and the L factor from MCNP. The relative deviations between the measurements and calculated signals for each assembly are plotted in Figure 11. Note that the data acquisition software of the FDET used in this measurement converted the measured electric current from the two ionization chambers into digital signals using an arbitrary constant factor, which was accounted for using a detector calibration factor. The

calculated FDET signals were observed to be generally within ~ 10% of the measurements for all assemblies, except for assembly #3. The relative standard deviations for the deviations between calculations and measurements among all assemblies were 10.5, 10.8, and 5.6% for the neutron-A, neutron-B, and gamma signals, respectively.

Assembly #3 was only irradiated in the reactor for one cycle, and it achieved a very low discharge burnup of 5.7 GWd/tU. Due to the low burnup, the neutron count rates for this assembly (< 0.4 cps) are approximately three orders of magnitude lower than that of the other assemblies, so statistical counting uncertainties (~9%) may have contributed to the large error. (The counting time for these

FDET measurements was ~5 minutes.) Further work to resolve the deviations for this assembly is ongoing. If assembly #3 were excluded from the set, then the relative standard deviations would be reduced to 5.8, 5.9, and 5.2% for the neutron-A, neutron-B, and gamma signals, respectively. These results are consistent with those reported previously for PWR measurement campaigns [5].

As with previous measurement campaigns, the correction for the gamma nonlinear ionization chamber response was found to be essential to the data analysis; assuming a linear response increases the relative standard deviation of the gamma results from 5.6% to more than 23%, with the largest deviations exceeding 45% for assembly #3

FA #	Fuel type[a]	Profile type[b]	Enrich (wt %)	Burnup (MWd/t)	Cooling time (days)	nA (cps)	nB (cps)	gamma (arbitrary units[c])	nA (cps)	nB (cps)	gamma (units)	Multiplication	nA	nB	gamma
						Measurements (M)			Calculations (C)				C/M-1 (%)[d]		
1	4	F	3.8	38,342	5,390	246.00	128.33	354,081	246.6	125.6	360,031	1.289	0.2	-2.1	1.7
2	4	F	3.8	43,685	5,390	400.00	209.00	446,000	412.0	209.8	398,095	1.274	3.0	0.4	-10.7
3	1	F	3.6	5,716	8,120	0.43	0.22	76,650	0.558	0.287	70,335	1.438	29.8	30.4	-8.2
4	1	F	3.6	38,710	7,917	224.63	119.57	310,250	221.2	112.7	310,382	1.274	-1.5	-5.8	0.0
5	1	P	4.37	50,166	1,343	916.25	450.67	1,151,348	878.8	447.5	1,129,271	1.289	-4.1	-0.7	-1.9
6	2	F	4.0	41,114	1,343	434.00	220.37	921,250	474.0	241.4	949,539	1.301	9.2	9.5	3.1
7	3	F	3.7	40,068	2,071	476.38	239.25	715,824	438.2	223.2	679,193	1.295	-8.0	-6.7	-5.1
8	1	F	3.6	39,339	6,832	282.45	141.15	325,193	263.8	134.3	336,003	1.275	-6.6	-4.8	3.3
9	1	F	3.6	41,749	5,012	398.62	207.85	373,438	402.9	205.2	403,609	1.274	1.1	-1.3	8.1
10	1	F	3.6	38,233	9,044	209.88	108.86	272,250	188.2	95.9	288,876	1.273	-10.3	-11.9	6.1
11	1	F	3.6	39,635	7,917	254.09	128.00	314,278	243.0	123.8	315,971	1.271	-4.3	-3.3	0.5
12	1	F	3.6	39,763	5,733	340.19	172.61	373,288	308.1	156.9	365,497	1.277	-9.4	-9.1	-2.1
13	1	P	4.37	48,568	980	803.03	392.18	1,265,443	811.6	413.2	1,331,992	1.295	1.1	5.4	5.3

[a]1 = TVEL standard fuel; 2 = TVEL fuel follower; 3 = BNFL standard fuel; 4 = BNFL modified fuel

[b]P = profiled enrichment assembly; F = flat (uniform) enrichment assembly

[c]The FDET software converted the measured electric current from the gamma detectors into digital signals with a constant factor.

[d]nA = neutron-A (bare) channel; nB = neutron-B (Cd liner) channel

Table 7: Summary of VVER-440 Fork measurements and analysis results.
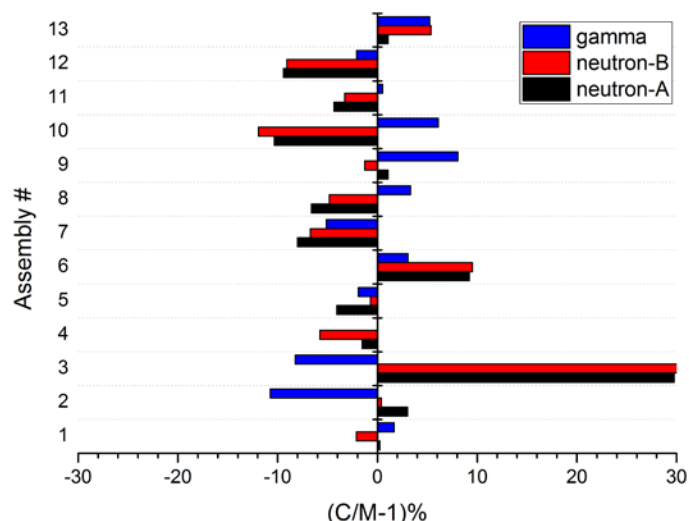
Figure 11: Relative difference between the calculated (C) and measured (M) neutron and gamma signals for the 13 measured VVER-440 assemblies.

(smallest signal) and assembly #13 (shortest cooling time and largest gamma signal).

Additional calculations were performed for assemblies #1, #2, #5, and #13 using ORIGEN libraries that were developed for both TVEL and BNFL/Westinghouse designs. Additional calculations were also performed to compare results using flat and different enrichment profile designs, since inspectors might not have access to this type of information. For these calculations, the effect of using different VVER-440 design libraries was < 1% for the gamma signal and 2–4% for the neutron signals. These differences are not large compared to other uncertainties and suggest that detailed knowledge of the fuel vendor or the detailed enrichment profile of the assembly are not essential.

Thresholds for significant discrepancies must be set by the safeguards inspectorate and the facility operator to trigger alarms when anomalies are suspected in the spent fuel assembly, the operator declarations, or the measurements. Careful considerations must be taken to set such thresholds to minimize the likelihood of false positive or false negative events. The thresholds must consider all the uncertainty sources in the predicted signals, including the uncertainties in the predicted nuclide concentrations and neutron/gamma source terms by the ORIGEN code with the ORIGEN libraries, the uncertainties in the response functions, the uncertainties in the measurements, the uncertainties caused by lack of detailed information regarding to fuel design and operating conditions, etc. These results provide initial data that can be used to develop such thresholds.

8.   Summary and conclusions

The FDET (a mature technology) and the PNAR (a new technology) are expected to play a role in safeguards measurements at the Finnish spent fuel encapsulation plant for final disposal. The ORIGEN module, incorporated into IAEA and Euratom's IRAP software, was developed to predict the FDET signals using pre-generated ORIGEN libraries, response functions, and operator declarations to assist the safeguards inspectors in identifying anomalies in real time. The ORIGEN module can be modified to predict signals for other NDA (e.g., PNAR) spent fuel measurements.

This paper provides an analysis of FDET measurement data obtained during a VVER-440 measurement campaign at the Loviisa Nuclear Power Plant in Finland for 13 assemblies. The FDET signals of these 13 assemblies were calculated using the new ORIGEN libraries, the new response functions, and the operator declarations of the fuel assemblies provided by the Finnish reactor operator. The results show that the calculated FDET neutron and gamma detector signals are generally within 12% of the measurements except for one assembly. This assembly had a much lower burnup than the others, and it had a measured neutron count rate of only 0.4 cps. Therefore,

the large discrepancy between the calculation and measurement in this case (~30%) can be attributed to poor counting statistics. If the assembly is excluded from the statistics, the average relative standard deviation between calculations and measurements is < 6% for both neutron and gamma signals. This result is consistent with previous results obtained for PWR measurement campaigns.

New ORIGEN libraries were developed using SCALE/TRITON based on ENDF/B-VII.1 nuclear data and fuel design information for the VVER-440 assemblies used in Finland. Performance of the new ORIGEN libraries was assessed by comparing the predicted nuclide concentrations using these libraries to DA-measured quantities obtained from literature. The comparisons of measured and calculated concentrations illustrate a generally good performance of the new ORIGEN libraries, with most calculated values being within or close to the assigned measurement uncertainties with several exceptions, which are discussed and explained in the paper. For application to spent fuel NDA, the simulations trend very closely to the measurements as a function of fuel burnup. New FDET response functions were generated using MCNP models for the VVER-440 fuel assemblies.

These results are directly applicable to preparing the ORIGEN module and FDET for use in safeguards verifications of spent VVER-440 fuel assemblies in routine inspections. These results are also applicable to future safeguards verifications in the planned Finnish encapsulation plants. A comprehensive study on various uncertainty components in the calculated FDET signals is recommended for future work to establish the acceptance threshold for the deviation between the calculated and measured FDET signals. The ORIGEN module is also being modified to predict PNAR signals in an ongoing effort.

9.   References

[1]   CHADWICK, M., HERMAN, M., OBLOŽINSKÝ, P., & al., e. (n.d.). *ENDF/B-VII.1 Nuclear Data for Science and Technology: Cross Sections, Covariances, Fission Product Yields and Decay Data.* Nuclear Data Sheets 112:12 (2011) pp. 2887-2996. https://doi.org/10.1016/j.nds.2011.11.002.

[2]   Gauld, I., Giaquinto, J., Delashmitt, J., Hu, J., Ilas, G., Haverlock, T., & Romano, C. (2016). Re-evaluation of spent nuclear fuel assay data for the Three Mile Island unit 1 reactor and application to code validation. *Annals of Nuclear Energy, 87*, 267-281.

[3]   Gauld, I., Hu, J., Baere, P. D., & al., e. (2015). In-Field Performance Testing of the Fork Detector for Quantitative Spent Fuel Verification. *37th ESARDA Annual Meeting, ISBN 978-92-79-49495-6.* Manchester, UK.

[4]   Gauld, I., Hu, J., Baere, P. D., & al., e. (2015). In-Field Performance Testing of the Fork Detector for

Quantitative Spent Fuel Verification. *ESARDA, ISBN 978-92-79-49495-6.* Manchester, UK.

[5] Gauld, I., Radulescu, G., Ilas, G., Murphy, B., Williams, M., & Wiarda, D. (2011). Isotopic depletion and decay methods and analysis capabilities in SCALE. *Nuclear Technology, 174*(2), 169-195, https://doi.org/10.13182/NT11-3.

[6] GAULD, I., SLY, N., & MICHEL-SENDIS, F. (n.d.). OECD/NEA Benchmark Database of Spent Nuclear Fuel Isotopic Compositions for World Reactor Designs. *PHYSOR 2014.* Kyoto, Japan.

[7] HAVLUJ, F. (2011). *ISTC #3958 project benchmark specification and preliminary evaluation.* London, UK: presentation at the OECD NEA WPNCS meeting of the Expert Group on Assay Data for Spent Nuclear Fuel.

[8] Honkamaa, T., Levai, F., Turunen, A., Berndt, R., Vaccaro, S., & Schwalbach, P. (2014). A Prototype for Passive Gamma Emission Tomography. *Symposium on International Safeguards.* Vienna, Austria.

[9] Hu, J., Giaquinto, J., Gauld, I., Ilas, G., & Keever, T. (2017). Analysis of new measurements of Calvert Cliffs spent fuel samples using SCALE 6.2. *Annals of Nuclear Energy, 106*, 221-234.

[10] ILAS, G., MURPHY, B., & GAULD, I. (n.d.). VVER and RBMK Cross Section Libraries for ORIGEN-ARP. *Proc. of the 8th International Conference on Nuclear Criticality Safety (ICNC 2007), vol. 2, p. 413–417.* St. Petersburg, Russia.

[11] JARDINE, L. (2005). *Radiochemical Assays of Irradiated VVER-440 Fuel for Use in Spent Fuel Burnup Credit Activities.* Lawrence Livermore National Laboratory, UCRL-TR-212202. http://www.llnl.gov/tid/lof/documents/pdf/319467.pdf.

[12] KUOPANPORTTI, J. (2016). *Design and simulation of reactor operating cycle.* presentation for Aalto University, PHYS-E0562 Nuclear Engineering. https://mycourses.aalto.fi/pluginfile.php/456531/mod_folder/content/0/PHYS_E0562_Kuopanportti.pdf?forcedownload=1.

[13] MAKAROVA, T., BIBICHEV, B., & DOMKIN, V. (2008). Destructive Analysis of the Nuclide Composition of Spent Fuel of WWER-440, WWER-1000, and RBMK-1000 Reactors. *Radiochemistry, 50*(4), 414-426.

[14] MICHEL-SENDIS, F., GAULD, I., MARTINEZ, J., & al., e. (n.d.). SFCOMPO-2.0: An OECD/NEA Database of Spent Nuclear Fuel Isotopic Assays, Reactor Design Specifications, and Operating Data. *Annals of Nuclear Energy, 110*(https://doi.org/10.1016/j.anucene.2017.07.022), 779-788.

[15] Nuclear Energy Agency. (2011). *Spent Nuclear Fuel Assay Data for Isotopic Validation (State-of-the-art Report).* NEA/NSC/WPNCS/DOV(2011)5, Nuclear Energy Agency. https://www.oecd-nea.org/science/wpncs/ADSNF/SOAR_final.pdf.

[16] OECD/NEA Working Party on Nuclear Criticality Safety. (n.d.). *Expert Group on Assay Data for Spent Nuclear Fuel.* https://www.oecd-nea.org/science/wpncs/ADSNF/index.html.

[17] Okko, O., Moring, M., Honkamaa, T., Martinkka, E., & Hmalainen, M. (2018). GOSSER - Geological Safeguards and Security R&D Project in Finland - How STUK prepares itself for the Final Disposal in Finland. *ESARDA Bulletin, 56*, 2-5.

[18] PAVLOV, S. (2011). *Investigation of the VVER-440 Fuel Burnup and Nuclide Composition for the Use in Burnup Credit-Related Tasks (BUC-II).* Dimitrovgrad, Russia: Final Scientific Technical Report on Task 5, ISTC Project #3958p, Research Institute of Atomic Reactors (SSC RIAR).

[19] REARDEN, B., & JESSEE, M. (n.d.). *SCALE Code System.* ORNL/TM-2005/39, Version 6.2.2, Oak Ridge National Laboratory, Oak Ridge, Tennessee (2017).

[20] Smejkal, A., Regula, J., Nordquist, H., Longo, J., & Linnebach, R. (2014). A New Software Development Paradigm. *Symposium on International Safeguards.* Vienna, Austria.

[21] SUBLET, J.-C., KONING, A., FORREST, R., & KOPECKY, J. (n.d.). *The JEFF-3.0/A Neutron Activation File—EAF-2003 into ENDF-6 Format.* JEFDOC-982, Commissariat à l'Energie Atomique, France, (2003).

[22] TOBIN, S., PEURA, P., HONKAMAA, T., DENDOOVEN, P., MORING, M., & CHAMPAGNE, C. B. (2018). *Passive Neutron Albedo Reactivity in the Finnish Encapsulation Context.* STUK report (Nuclear Materials), ISBN 978-952-309-406-2.

[23] Vaccaro, S., Gauld, I., Hu, J., & al., e. (2018). Advancing the Fork detector for quantitative spent nuclear fuel verification. *Nuclear Inst. and Methods in Physics Research, A, 888*, 202-217.

[24] Vaccaro, S., Gauld, I., Hu, J., & al, e. (https://doi.org/10.1016/j.nima.2018.01.066, 2018). Advancing the Fork detector for quantitative spent nuclear fuel verification. *Nuclear Inst. and Methods in Physics Research, A, 888*, 202-217.

[25] X-5 Monte Carlo Team. (2003). *MCNP - A General Monte Carlo N-Particle Transport Code, Version 5.* Los Alamos, NM: Los Alamos National Laboratories (LA-UR-03-1987).

Opportunities for a graded approach in air sample assay and triage

Robert B. Hayes[1] and S. Joseph Cope[2]

[1]North Carolina State University, Nuclear Engineering Department, 2500 Stinson Dr, Raleigh NC, 27695-7909, USA
[2]Joint Base Andrews, 1783 Arnold Ave, MD 20762 USA
Email: rbhayes@ncsu.edu, copesj@nv.doe.gov

Abstract:

Rather than waiting for radon progeny to decay prior to counting an air sample, scalar counts have been shown to provide useful information when appropriate technical interpretation is utilized. This work will review limits from the first frisk of an air sample to recent research showing how the initial decay profile can provide ever increasing discrimination capabilities if measured. Methods demonstrated in the literature along with future opportunities will be reviewed in this presentation. Applications for routine nuclear facility operation, radiological emergency response and treaty verification will also be considered.

Keywords: Air monitoring; Triage; Routine sampling assay

1.   Introduction

The downwind monitoring of radioaerosols can be used to monitor upwind releases from nuclear facilities. Correlating a measurement to an upwind source can be an arduous task involving many uncertainties and assumptions [1]. One of the physical properties that has to be well understood is the interference created by radon progeny in the air. With radon progeny being alpha, beta and gamma emitters, this can pose various challenges.

Radiological aerosols have additional evolutionary size properties not found in typical organic materials. If these begin as a radioactive gas and have a charged particle decay mode, unique physics can change their subsequent behaviour. Specifically, when the airborne radioisotopes decay by charged particle emission, the resulting atom itself is left with a net charge. This can then induce polarization in any nearby aerosol such that the point charge and the induced dipole have a coulombic attraction allowing them to become attached causing the aerosol to evolve in shape as a function of time and subsequent decays.

Not all radioactive gases with charged particle decay modes will attach to aerosols. This results in an attached fraction and an unattached fraction of the subsequent decay progeny as occurs with radon progeny [2]. The evolution of these radioaerosol particles are then generally sampled with an air filter which itself has particle size sampling efficiencies making precision air monitoring convoluted at best.

1.1   Natural sources and decay products from radium

A primary difficulty in radiological air monitoring is due to the ubiquitous and dynamic properties of radon progeny. The crustal content of both ^{226}Ra and ^{224}Ra are from their respective ^{238}U and ^{232}Th parent primordial decay chains. All ^{226}Ra and ^{224}Ra decay into ^{222}Rn and ^{220}Rn respectively which are commonly referred to as radon and thoron accordingly. The radon and thoron then have their own decay chains eventually becoming isotopes of lead. These naturally occurring radioactive materials (NORM) have dynamic contributions arising from disparate decay rates, meteorology and regional geology.

The decay series of Radon and Thoron are shown in Figures 1 and 2 respectively

1.1.1 Radon

The relevant decay series for radon shown in Figure 1 includes maximum beta emission energies. Note that once ^{210}Pb is formed, it's 21 year half-life effectively removes it from any atmospheric content as it is naturally scrubbed from the air into the soil. The subsequent decay series can be resuspended but generally has a negligible content in air samples.

As radon has a half-life of 3.8 days, it has some time to diffuse out of the host rock which contained its parent ^{226}Ra. This does require that the noble gas can migrate to a grain boundary or other pathway out of the rock. Even being a noble gas, its generation in the radium inclusions of the host rock do not guarantee a simple diffusion path to the atmosphere. The alpha track damage from the radium decay accumulates over time around these radioactive inclusions and can create at least a portion of a viable path (particularly over time). Recoil from alpha decays of the ^{226}Ra also cause shorter range local μm scale damage to the mineral matrix. The greater track length of an emitted alpha effectively punches a hole in its host matrix up to many 10's of μm which build up over time resulting in various radial starting pathways for successive radon emanations to travers when randomly attempting to find a grain boundary.
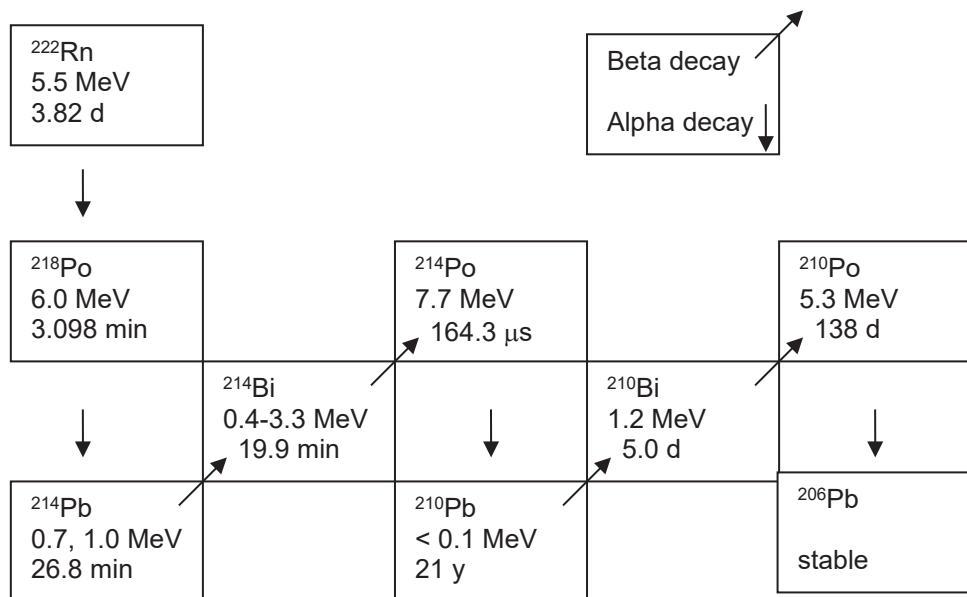
Figure 1: ^{222}Rn decay series (from ^{238}U), half-lives shown below characteristic energies.
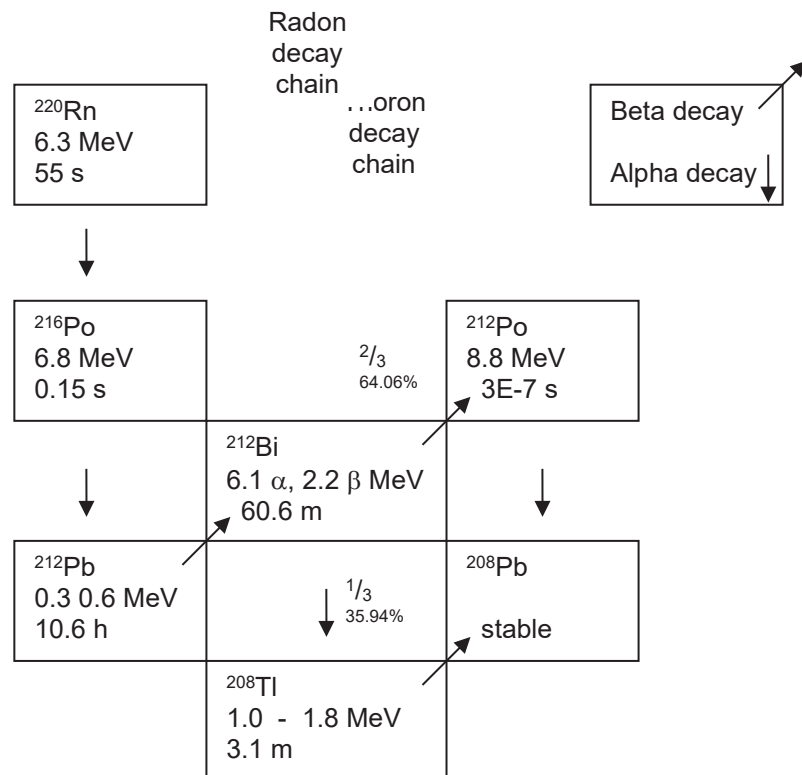
**Figure 2:** ^{220}Rn decay series (from ^{232}Th), half-lives shown below characteristic decay energies.

1.1.2 Thoron

The thoron decay series is shown in Figure 2 also includes maximum beta energies shown.

Thoron is a bit unique in that its parent ^{224}Ra along with the primordial ^{232}Th has a much higher crustal abundance compared to ^{238}U and its progeny ^{226}Ra but has a much lower atmospheric content. Although this converse relationship is not expected due to source terms (thoron having a lower air concentration than radon), the actual cause is the half-life of the noble gas ^{220}Rn which is just under

1 minute. This means that if the thoron is not able to easily escape from the rock matrix into the atmosphere in less than a minute, it will decay back into a heavy metal and so the resultant decay chain is confined to the soil. As such, on average, radon will exceed thoron to around a 3 to 1 ratio even though their parent ratios are inversed.

The thoron decay series has a unique feature of interest in that the isotope ^{212}Bi is able to decay by either beta or alpha decay with an approximate 2:1 split. This isotope will typically be in transient equilibrium with its longer lived parent ^{212}Pb when left undisturbed over many hours.

1.1.2.1 Thoron constancy

An additional unique aspect in thoron content is that with the parent having less than a 1 minute half-life, it cannot travel far prior to initiating its decay series. This because radioactivity by nature always has an independent probability of decay so that the portion which arises in gaseous form still has the same half-life as that which was retained in the soil mineral components.

Unlike radon which has a 4 day half-life and can travel great distances with the wind, the 1 minute half-life of thoron does not allow it to travel even nominal distances as it will decay into heavy metals very quickly (Figure 2). The ^{212}Pb can travel nominal distances having an 11 hour half-life but it is not able to be fed by a continual ^{220}Rn source as this thoron stays effectively right where it was generated (from ^{224}Ra decay).

1.2 Temporal variations in radon progeny

All the isotopes seen in Figures 1 & 2 are dynamic in that they can be going from attached to unattached (through radioactive decay recoils and gaseous collisions) along with the parent gaseous isotopes going through increases or decreases from other effects. These changes can all contribute to the variations seen in this interfering background radon progeny distribution. Understanding the various causes for these changes can allow mitigation, controlling or otherwise addressing any deleterious effects from the same. An example of a typical alpha and beta spectrum from ambient air showing the various naturally occurring airborne radionuclides is seen in Figure 3.

#### 1.2.1 Causal initiators of radon progeny dynamics

There are many factors which give rise to variations in natural airborne radioactivity levels. The largest tends to be that of temperature inversions. A natural inversion typically occurs in the mornings due to the adiabatic lapse rates from the ground preventing any mixing of surface air with the upper atmosphere. This means that all radon which has escaped from the ground simply builds up near the surface until it can be diluted later in the morning due to convective currents which allow mixing with the upper atmosphere. These convective currents are initiated by ground heating from solar irradiance in the morning. This effect also has seasonal dependencies with winter typically having the largest inversion effects resulting in the largest ground radon concentrations.

Another very large effect in environmental radon and its progeny comes from precipitation. When rain falls through radon and its progeny it pushes these radionuclides to the ground cleaning the air but raising the terrestrial dose rate by many orders of magnitude [3]. Barometric pressure is another cause of changing radon levels. When a low pressure comes in, this can pull radon from the soil as a high pressure system can retard radon diffusion from the ground.

1.3 Alpha and beta spectra from environmental samples

The distribution of energies shown in Figures 1 and 2 result in spectra exemplified by Figure 3 where no transuranic (TRU) activity is present. Here, the peaks are labelled by their dominant contributing radionuclides. The peak location represents those occurrences when emitted alpha particles move normal to the filter and detector depositing a characteristic energy into the detector active volume. Spreading occurs from interstitial air, filter media and oblique paths to the detector from the source filter. In this sense, the majority of detected alpha particles is not at the maximum possible energy for a particle where minimum attenuation takes place in the filter, its sampled material, the air layer separating the detector and the detector dead layer.
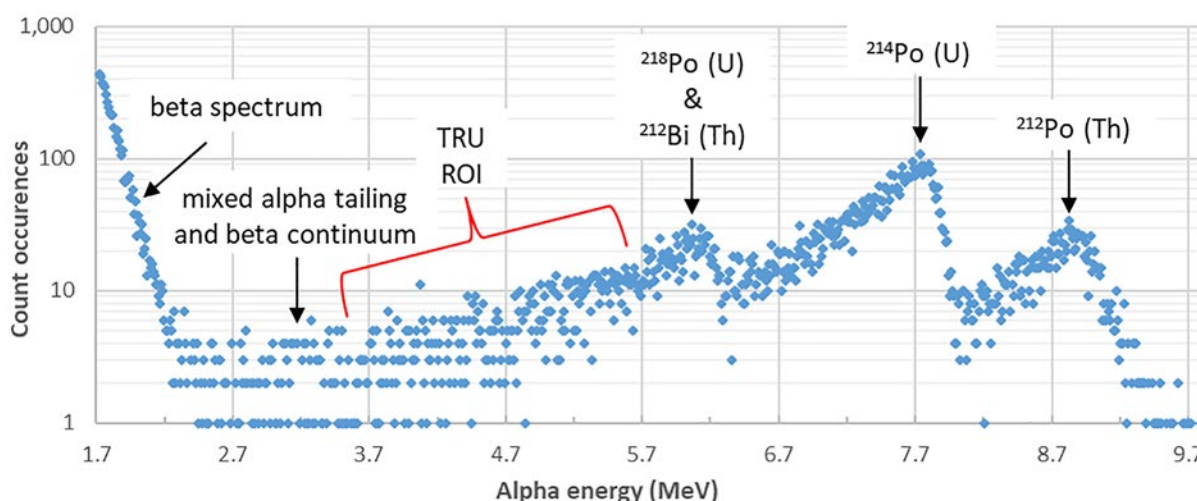
Figure 3: Example charged particle spectra (semi-log) measured from an environmental air sample with peaks and regions labelled associating primordial parents indicated as ^{238}U=U and ^{232}Th=Th from Figures 1 & 2.

The TRU region of interest (ROI) in Figure 3 represents where most of the transuranic isotopes will be present and so the large count rate present from tailing of the higher energy NORM alpha peaks creates considerable background in the TRU ROI (hence the desire to allow them to decay prior to assay).

The abscissa scale is based on only the three labelled NORM peaks so that the beta energies are overestimated in this scheme. This is because the ionization in the detector has a higher efficiency with beta particles than alphas for the same kinetic energy. Alpha particles lose a certain portion of their energy creating vacancies and interstitials due to recoiling nuclei whereas beta particles have a much higher threshold to displace an atom in the detector volume resulting in a larger fraction of their deposited energy going into ionization only.

1.3.1 Spectral manipulation options

Typical commercial options to mitigate these features involve curve fitting the shapes which is feasible when substantial particulate loading does not drastically degrade the spectra from self-attenuation effects. The more complicated options include Gaussian fits to the top of the peaks with exponential tails above and below these. Other options include simple region of interest (ROI) summing of the peak areas separated by their respective minima. Template shapes for each peak could be fit in amplitude as well but each of these options have potential issues with spectral degradation occurring as filter loading increases (due to dust build-up).

Peak shifting and tailing slope dependencies with filter loading could be mitigated by allowing peak locations to be variables along with exponential fitting portions (or template shapes). This would require sufficient knowledge of overlap dependencies in the TRU ROI for discrimination purposes.

1.3.1.1 Limitations with spectral manipulation

When filter loading occurs, the peak locations shift to lower energies and the low energy tails from each peak will increase accordingly. The low energy tails seen in Figure 3 can be verified upon inspection that they would all match an exponential function well (due to the linear appearance in the semi-log format). The argument of the exponential in such a fit would then be functionally dependent on the filter loading in a potentially predictable manner with sample mass (assuming linear deposition rates). Similarly, the peak locations could also be functionally dependent on filter loading. In principle, dependencies such as these could be monitored and trended to estimate filter loading and so serve as a metric for when to change a filter and so optimize sample sensitivity overall.

It should be pointed out that there are some TRU isotopes having energies near the 6 MeV NORM peak, specifically,

the ^{252}Cf and some of the curium isotopes, such that these have peaks very near or even indistinguishable from the 6 MeV NORM peak. Methods to mitigate this are discussed in a later section but invariably utilize the decay series (see section 1.3.2) in some fashion.

1.3.1.2. Potential benefits from spectral analysis

In principle, sensitivity could be increased over gross counting given that each alpha emitter has distinct ROIs which follow defined patterns which could be leveraged in the analysis using various means. If the contributions to the TRU ROI can be accurately estimated from the higher energy NORM peaks, then the background in this ROI can be substantially decreased and so concomitantly decrease the detection limit for anthropogenic activity. If spectral quality metrics are designed to indicate when the assumptions from the fit are being challenged, then additional rigor in the assay can be realized. Care should be utilized in any such approach as vendors have historically fallen short in properly testing and validating such systems prior to marketing.

1.3.2 Spectral and temporal coupling

The decay series given in Figures 1 & 2 all have to obey the Bateman equations represented by Equation 1. These are the governing equations for all radioactive decay series allowing for any length of a decay chain. Here each isotope activity A_j has an associated decay constant λ_j with an initial parent concentration $N_1(0)$.

$$A_j(t) = N_1(0) \sum_{m=1}^{j} C_m e^{-\lambda_m t} \text{ where the coefficients}$$

$$C_m = \frac{\prod_{i=1}^{j} \lambda_n}{\prod_{\substack{i=1 \\ j \neq m}}^{j} (\lambda_i - \lambda_m)} \tag{1}$$

1.3.2.1 Decay characteristics for thoron 6 MeV alpha contribution

This means that the standard decay rate of the ^{212}Bi alpha peak at 6.1 MeV will be fed by the decaying ^{212}Pb isotope which is easily discriminated by it's associated isolated 8.8 MeV peak from the subsequent progeny ^{212}Po. Due to the negligible half-life of ^{212}Po, it is continually in transient equilibrium with its parent ^{212}Bi scaled only by the appropriate beta branching ratio of the latter.

1.3.2.2 Decay characteristics for the radon 6 MeV alpha contribution

Likewise, the radon progeny contribution to the 6 MeV peak from the ^{218}Po initial activity is itself the source of contributing activity to the initial ^{214}Pb activity which contributes to both of the initial ^{214}Bi and ^{214}Po activities with the latter emitting the readily discriminated 7.7 MeV peak. Specifically, due to the negligible half-life of ^{214}Po, it is

always in transient equilibrium with its parent ^{214}Bi. From these, the Bateman equations (Eq. 1) could be used (explicitly or through some simplification) to correlate background in the TRU ROI (from ^{218}Po contributions) to the readily discriminated count rates in the ^{214}Po ROI (this would likely be a retrospective or delayed correction).

1.3.3 Beta spectral options

The beta portion of the spectrum can be folded into any desired use of the Bateman equations (Eq. 1). Typically, the radiological risk from beta activity is so much lower than that of TRU alphas that gross counting is adequate to provide desired detection sensitivity [4]. As such, the exact beta energy calibration is not considered of high importance given its added difficulty of only having a continuum source preventing a simple and precise means of scaling (particularly in the presence of alpha cross talk).

1.4   Mitigating radon progeny in air monitoring

Typical air monitoring techniques involve pulling a precisely measured volume of air through an air filter. The air filter is then assayed for radiological content such that the ratio of the assay to the volume is the resultant air concentration ascribed to the space sampled. The standard approach utilized in routine nuclear operations, radiological emergency response and even treaty verification is to allow the air sample to sit for multiple days to allow the entrained radon progeny to decay prior to characterizing any anthropogenic content on the air filter. This is due to the array of alpha, beta and gamma disintegration energies present in any aged sample of ambient air due to all the radon progeny present (Figures 1, 2 and 3).

In principle, the air sample could be measured at any time while waiting for the radon progeny to decay away, but unless the anthropogenic component is large compared to the radon progeny, discrimination is haphazard at best. Vendors have claimed to produce algorithms which can discriminate anthropogenic activity based on alpha and beta spectrometry which have been shown to be unreliable [5,6].

1.4.1 Initial frisk

Based on the ratio of alpha to beta activity, some limits can be placed on the maximum anthropogenic which can be present and still attain these ratios [7]. Given that radiation cannot be sensed in any of the traditional observational modes (sight, smell and touch), it requires detectors and so airborne radioactivity, when present, requires similar infrastructure. The variability in alpha to beta ratios can vary dramatically due to all the dependencies on the contributing isotopes (see section 1.2). All that the initial frisk can determine is whether the ratio of alpha activity to beta activity could credibly have been obtained from the normal variability in NORM.

1.4.1.1   Mitigation limitations

Any initial frisk values will by definition be dynamic and so generally very insensitive in discriminating NORM from anthropogenic. The various combinations of attached and unattached fractions coupled with dynamic radon and thoron levels with size dependent filter efficiencies etc all couple into a difficult characterization at best.

This is problematic in that virtually all air samples have only trace quantities of the target isotopes unless only radon progeny itself is being assayed. This trace characteristic inherent to the isotopes of interest in an air sample arises from the nature and purpose of the sample. In normal operations, most air samples are intended to demonstrate either a zero release or at most a regulatory compliant result (which is always small).

In emergency response, field teams would have to dress out in full personnel protective equipment along with decontamination of vehicles if they were to sample in contaminated areas. As such, field teams typically sample on the penumbra of a plume so that the contamination levels are comparable to background already making detection difficult (where the bulk of any release or ground deposition characterization occurs from the air with large gamma detection arrays).

Treaty verification is generally very far down range again making concentrations almost vanishingly small. In all cases then, the radon progeny on an air sample is likely to be the dominant source of all ionizing radiation emissions.

1.5   Utility of the presented methodologies

The research reviewed in this work demonstrates novel methods to characterize the anthropogenic activity in such a way as to utilize the interferent radon progeny signals to estimate the long lived activity on the filters. Rather than throw away these interferent signals, this work will review various means to use them in a graded approach to characterizing airborne radioactivity. In this way, rapid, yet quality, initial TRU estimates can be obtained in any air sample protocol from treaty monitoring to nuclear safety and even operational radiation safety applications.

2.   Graded approach

The graded approach itself means that improving levels of quality will scale with increasing effort or time permitting defence in depth towards the eventual goal. In this case, we are looking for a quality method to characterize anthropogenic radionuclide levels in the atmosphere despite the interfering radon progeny species. Quality being defined here as a measurement containing rigorous physics based characterization of the true dispersion inherent to the final assay results.

The current missing piece in air monitoring data is a quality assay technique which can be used to characterize air samples while the radon progeny is still relatively high. Provided that the uncertainty estimates are rigorous and accurately describe the dispersion in the measurements, high uncertainty values are entirely useful. This is because some quality information is always better than no information where quality is strictly defined as any assay having rigorous uncertainty estimators.

2.1 Quality convergence

The intent for air monitoring is to properly characterize the risks associated with airborne materials. With radiological materials, this is typically the risk from inhalation which is measured in actual or potential dose. Potential dose being the dose a person would receive were they to actually be in a given location for a proscribed period of time (such as a theoretically maximally exposed individual). Consequences can also be in terms of land contamination which again is typically measured in terms of risk by the maximum potential dose an individual could credibly receive from all input vectors. With treaty compliance monitoring, the desired result is not just detection but discrimination from legitimate commercial sources.

2.1.1 Nuclear security

In nuclear emergency response, treaty verification and even non-proliferation applications, quality may be measured in at least two ways. In some sense, characterization of any anomaly would be inherently useful enabling further investigation. In a more detailed example, quality may be expressed in terms of the rigor with which the anthropogenic portions of the air sample can be ascribed to adversary behaviour and discriminated from legitimate industrial or commercial endeavours. It is in the discrimination of adversary actions from those beneficial activities that is needed in nuclear security applications.

Current technology largely relies on chemical, nuclear and morphological assays from air sample particulate. As with all of the other air monitoring applications, the radiological characterization portion requires mitigation of the natural radon progeny inherent to all commercial air sampling technologies.

3. Using all the decay data

When allowing the radon progeny to decay prior to the resultant air sample assay, it is inherently assumed that the progeny is purely an interferent and so does not contain useful information regarding the target assay of the anthropogenic activity. Our research has shown that there is useful information which can be extracted from the natural radon progeny when evaluated in a graded approach formalism. Specifically, starting with a quick handheld frisk for a very low quality assay (assuming a frisk has known

efficiencies [7]), some information can be obtained. Additional measurements when continually applied (utilizing appropriate instrumentation and analysis) allows a continual improvement in the precision of assays (without compromising accuracy) until the eventual "gold standard" of destructive assay by radiochemistry can be applied some days or weeks later. The key is being able to use the physics of the interferent to help characterize it and so subtract or mitigate it in some useful way.

3.1 Decay curve fitting

In principle, all radioactive decay chains adhere to the Bateman equations (Eq. 1) which can address only radioactive decay. If the initial conditions are known, then the Bateman equations can be solved to predict all isotopic abundances in the decay chain for all future times. Radon progeny has the inherent difficulty that the parent is continually changing (see section 1.2) and meteorological changes can also drastically bias progeny separate from the radon parent. This being partially due to the parent being a noble gas with the progeny being heavy metal (ions) either attached or unattached to ambient aerosols.

If the Bateman equations were utilized, their general form would follow that given in Equation 1 such that fitting to a measured series of counts (a decay curve) could result in an overdetermined system of equations. With radon having only 4 relevant radioactive progeny (Figure 1) and thoron having 5 (Figure 2), this would require at a minimum of 9 decay count measurements to obtain estimates for each isotope initial activity estimate. If only 9 counts were obtained, measurement scatter would prevent an exact fit despite 9 fitting parameters attempting to model 9 data points as Equation 1 can only model continuous and smooth functions and so not noise.

3.1.1 Curve fitting statistics

Due to instrument uncertainty and statistical fluctuations in decay rates, at least a dozen or so measurements are desired for each degree of freedom to approximate a normal distribution in the fitted parameters convergent value. With this number of data points, a mean, its standard deviation along with a chi-squared test to evaluate the likelihood that the distribution was normal can all be estimated for any given parameter. When multiple parameters are being estimated in a curve fit, commensurately more data points would be desired. If only 2 parameters are to be estimated (an initial activity and a decay constant), then preferentially more than a dozen measurements would be the target.

This approximation assumes that around ten measurements are desired for a single mean, and a few dozen for a line and around 30 for a quadratic and so on. There is no hard limit or rule for such a generalization but the driver here is to get a quality *t*-test on each fitted parameter. A quality *t*-test is not dependent on sample number if the

assumption of normality is valid. Estimating normality based on a small sample is largely untenable so this gross assumption is stated as a matter of opinion only.

3.1.2 Overdetermined curve fits

Technically, one can estimate the slope, intercept and their uncertainties along with a standard error of the fit and a correlation coefficient from just 3 points (even random points). In this extreme example, 5 values are obtained from 3 data points giving an apparent negative set of degrees of freedom. This really just means that multiple measures of the mean and distribution are redundant and do not convey independent information despite their typical interpretation being independent measures of central tendency.

One general goal in curve fitting is to increase your degrees of freedom as much as possible without excessively incurring scatter by splitting up your counting interval into ever decreasing intervals. Using the traditional definition of degrees of freedom (*DoF*) being the difference between the number of fitted data points (*N*) and that of the number of fitting parameters (*M*), it is preferable to have this value (*DoF=N-M*) as close to 30 as possible to enable an assumption of normal statistics. Otherwise, a *t*-distribution would be assumed incurring less certainty in distribution types (which can itself be tested).

3.2 Radon progeny decay curves

The two dominant isotopes driving the decay rates from radon progeny are the ^{214}Pb and ^{214}Bi isotopes having half-lives of 26.8 m and 19.9 m respectively (Figure 1). Combining these two in sequence via Equation 1 results in an approximately effective decay constant greater than either producing values ranging from 30 to 40 minutes (depending on initial conditions).

In order to get proper leverage in measuring the half-life of a radionuclide through a decay curve, ideally the measurement time should be long compared to the half-life. If a large section of the effective decay curve from radon progeny is to be sampled, then ideally at least 30 minutes of sampling time would be a minimum.

3.3 Long lived activity decay curves

If an operationally friendly time window for measuring an air sample is a few hours, then any activity having a half-life large compared to this would appear to be largely indistinguishable from a constant. Here, an isotope with constant activity does not actually exist but can be approximated by any radionuclide with a very long half-life compared to the count time.

With this, if thoron content is present in an air sample which only measures decay over a period of a few hours or less, the 10.6 hr half-life of ^{212}Pb would cause it to look like constant (anthropogenic) activity like that of a transuranic (TRU) nuclide. If a decay curve fit modelling the radon progeny did not account for this thoron content in a short time window, this component would conservatively bias the long lived (approximately constant) activity to have a higher estimate.

3.4 Combined decay curves

If a decay curve is measured within a few hour window, the radon progeny would appear to go through multiple half-lives while the thoron progeny would appear largely constant. Any anthropogenic activity present will likely have decay constants comparable to ^{137}Cs, ^{90}Sr or any of the TRU nuclides which effectively would be modelled as a constant activity. Putting all this together in a decay curve fit model, Equation 2 presents the filter activity *A*(*t*) at any given time *t* following flow cessation. Here, *m*1 is the initial short lived activity, *m*2 is the effective short lived decay constant and *m*3 is the long lived activity which will be biased high due to thoron progeny. If this function is then fit to a decay curve, the effective half-life is then ln(2)/*m*2. All results used the Levenberg-Marquardt fitting algorithm to data.

$$A(t) = m1 \times e^{-m2 \times t} + m3 \qquad (2)$$

4. Historical results

When fitting actual filter decay data, the distribution seen in Figure 4 was obtained as described elsewhere [8]. The distribution shown represents the suite of resultant *m*3 values and their uncertainties combined via a kernel density estimator. The results from plutonium superposition with environmental air samples is shown on the left with a similar thorium study shown on the right. In these works, the results from using Equation 2 on actual air filters both with and without anthropogenic activity are compared in their rapid assay capabilities.

The histogram results shown in red are the calibration results obtained from filters not having any interferent NORM activity representing the correct values and their distribution which should be obtained from a proper use of Equation 2 on air filters having both interferent natural and anthropogenic activity.

The blue histogram results were obtained using Equation 2 on filter decay counts which had both the anthropogenic and natural radioactivity constituents. The two distributions (red and blue) are visually indistinguishable although the histogram results do not incorporate individual measurement errors from fitting Equation 2 to the decay curve data.

The red and blue dashed vertical lines represent the mean from each distribution. In this sense, the blue is the best estimate from the fitting approach of Equation 2 to environmental air samples with a TRU source superposition. The TRU source distribution without radon progeny activity is shown in red. What is evident from the blue data is that
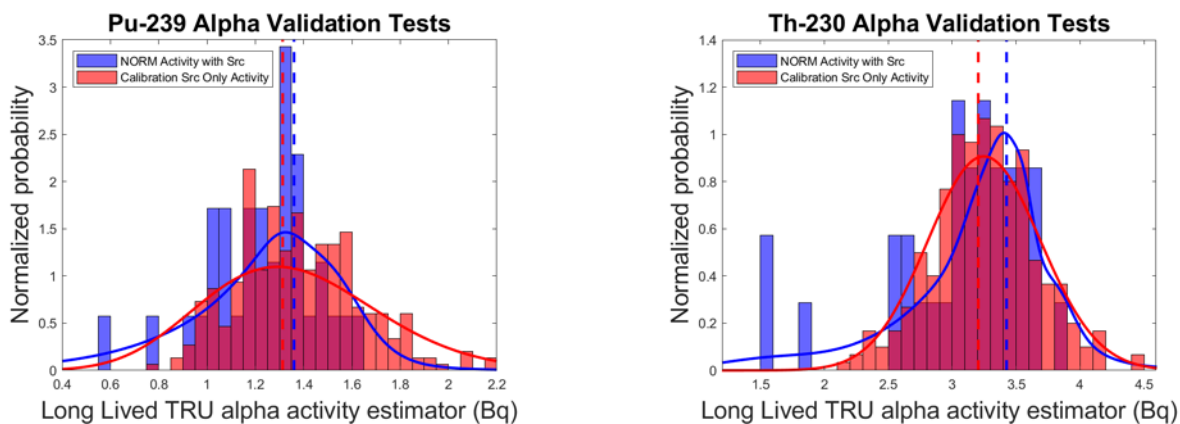
Figure 4: Decay curve fit results from effectively spiked air filters [8]. Blue values represent a used air filter superimposed with TRU activity. The red values represent blank (unused) filters superimposed on the same TRU activity used in making the blue results.

on average, use of Equation 2 provides conservative estimates of the known anthropogenic activity (indicated by the red data).

4.1 Kernel density estimator (KDE)

When histogramming data possessing individual uncertainties, the uncertainty portion of the data is simply discarded. This need not be the case when using a KDE which is represented by Equation 3. This effectively turns each data point used to construct the histogram into a normalized Gaussian so that the superposition of all these Gaussians becomes a continuous probability distribution function when Equation 3 is used to represent the data. This allows deconvolution of the resultant KDE into individual components or to conduct hypothesis testing on the resultant distribution. Note that the parameters used in Equation 3 are such that μ_i are the individual measured values having unique uncertainty values of σ_i from n total measurements. The use of $P(x)$ is intended to convey that when normalized in this way, the KDE is a proper probability density function sufficient for hypothesis testing.

$$KDE(x) = P(x) = \frac{1}{n}\sum_{i=1}^{n} \frac{e^{-0.5\left(\frac{x-\mu_i}{\sigma_i}\right)^2}}{\sigma_i\sqrt{2\pi}} \qquad (3)$$

The KDE values from the fitted $m3$ distributions (Equation 2) are presented in Figure 4 as continuous lines which are color-coded in conjunction with the histograms.

4.2 Upper confidence limit of individual fits

The blue results seen in Figure 4 clearly have entries which are below the red dashed line. With the red vertical dashed line representing the correctly calibrated (best estimate) of the TRU content measured with the air filters, the lower blue occurrences would be underestimates and so not a conservative assay. As such, this might appear to give results which when using Equation 2 would underestimate the correct anthropogenic activity and so constitute a potential safety concern. This turns out not to be the case

when individual measurement results are evaluated at their upper 95% confidence limit. When taking all the assayed results at their upper 95% CL, there were no underestimates of the characterized TRU source activity found demonstrating the savings offered from fitting decay curves using Equation 2 allowing for conservative upper bounds in all observed cases.

A histogram of all the measured assays of the TRU content using Equation 2 are shown in Figure 5. Here, the results shown are all of the $m3 + 1.645\sigma_{m3}$ values obtained previously [8].

Previous work has considered 30 min intervals within a 2 hr counting window to understand the uncertainty penalties associated with more rapid TRU activity estimation; again, the results can still be considered quality, even with a large uncertainty estimator, provided that it is rigorous and maintains a physical basis. Utilizing a weighted average of 35 filters for each TRU source study, the TRU estimate for each time study is given in Figure 6. The error bars noted in Figure 6 represent the standard error of the mean at the 95% CL and should be interpreted as a potential "best estimate" scenario when conditions allow for a weighted average technique. What is truly profound is that this conservatism remains throughout the range of 30 minutes up to 2 hr measurement time with shorter measurement intervals incurring larger uncertainty (and so higher conservatism in the upper 95% CL) as reported elsewhere [9].

These results show that the asymptotic constant activity value at infinity from Equation 2 results in conservative estimates of the long lived activity whenever uncertainties are evaluated at the 95% CL. This is attributed to both the thoron progeny bias (^{212}Pb limiting the ^{212}Bi activity change in rate) when measuring a short time interval and taking only the upper 95% CL. In this thoron progeny bias, the ^{212}Bi alpha and beta decays approach a transient equilibrium with the parent ^{212}Pb activity which has just under an 11 hour half-life.
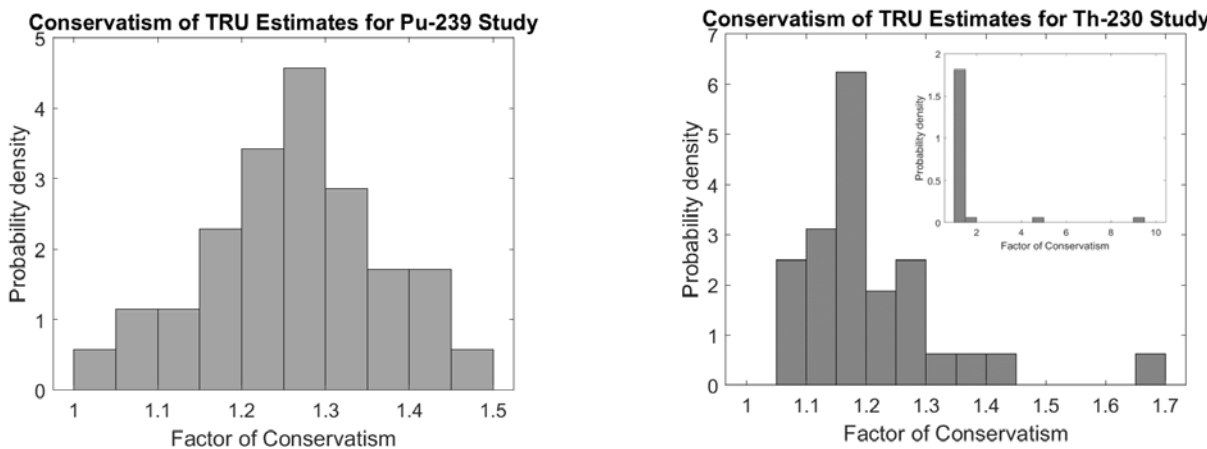
Figure 5: Upper 95% confidence level obtained from using Equation 2 to rapidly estimate anthropogenic content on air filters [8]. Values include thoron progeny bias from conducting only a 2 hour decay count.
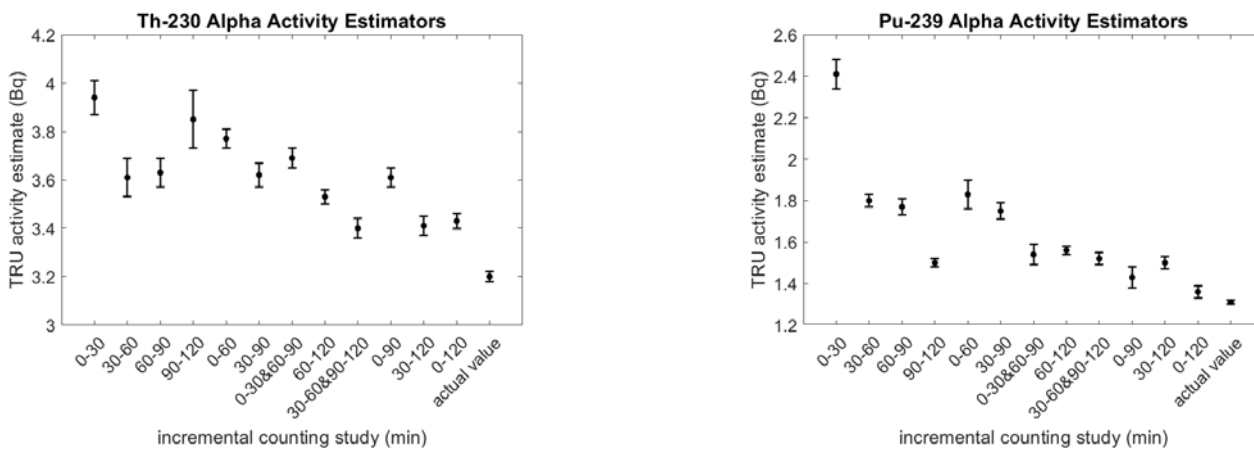
Figure 6: Incremental 30 min weighted average TRU alpha activity estimates from effectively spiked environmental air filters with uncertainties shown as standard error of the mean [9].

4.3 Summary of results

The decay curve fitting of sequential count data using the Levenberg-Marquardt algorithm can provide parameter estimates with their associated uncertainties to Equation 2. This enables novel applications involving kernel density estimators and their subsequent deconvolution [10]. More importantly, multiple options for using the information normally discarded in traditional air sampling assay has been shown to give quality low precision results quickly [9]. This in turn fills a high priority information gap typically occurring when air concentration data is desired rapidly from standard air samples.

4.3.1 Alternative approaches to triage

Many other options for pursuing further graded approaches in air sample assay and triage have been identified beyond the results reported here [11,**Error! Reference source not found.**2]. These generally involve spectroscopy coupled with other methodologies but can even include additional gross assay techniques (such as longer count times). The spectral analysis methods could even include mass loading mitigation, temporal dependencies and assaying of TRU isotopes having the insidious alpha decay energies very near 6 MeV.

5. Discussion

The KDE results seen in Figure 4 would permit deconvolution into the respective error contributing sources. Previous results have been able to discriminate contributions from the instrument and those of radon and thoron [10]. The techniques described here demonstrate utility in the period of time while samples are customarily being allowed to passively decay away to clear up the TRU ROI signals seen in Figure 3 and so allow low detection limits.

5.1 Emergency response applications

In emergency response scenarios, this could be accomplished when samples are being returned from the field. Having a small scalar or spectral counter in the transport vehicles would allow obtaining results prior to submitting samples to the lab. Starting with an initial frisk, the samples could be continually counted in a decreasing uncertainty manner allowing quality triage in determining which samples should be shipped off for formal radiochemical digestion, separation, electroplating and final vacuum alpha and beta spectroscopy (a high resolution version of Figure 3 with no radon progeny present).

5.2 Treaty verification applications

Modern Comprehensive Test Ban Treaty (CTBT) monitoring based on the Radionuclide Aerosol Sampler/Analyzer (RASA) systems require a delay in assaying radioaerosols to allow radon progeny decay. If a large release just went past a monitoring station, it would have to wait for the decay period to elapse prior to even looking for the activity. The discussed approach involving decay curve fitting could be accomplished as a low sensitivity interim measurement enabling this early warning capability for any nominal plume passage prior to the customary wait periods.

5.3 Operational health physics applications

Nuclear facilities routinely allow air samples to lay dormant prior to measurement to remove radon progeny through decay. If early estimates were desired, fitting the decay curve would allow just such a graded approach to their defence in depth. Simply put, quality assays can be obtained rapidly if desired.

6. Conclusions

Many opportunities to improve standard air sample analysis have been explored with examples provided of some of those which already have experimental results. Utility of the decay curve fitting methodologies appear to have potential application in nuclear safeguards, non-proliferation, radiological emergency response and even routine health physics applications.

7. Acknowledgements

8. References

[1]   Hayes RB. Reconstruction of a radiological release using aerosol sampling Health Phys. **112**(4), p 326-337; 2017.

[2]   NCRP, National Council on Radiation Protection and Measurements. Radon exposure of the U.S. population, status of the problem. Bethesda, Md: National Council on Radiation Protection and Measurements; 1991;1990;.

[3]   Mercier JF, Tracy BL, d'Amours R, Chagnon F, Hoffman I, Korpach EP, Johnson S, Ungar RK; *Increased environmental gamma-ray dose rate during precipitation: a stong correlation with contributing air mass*; Journal of Environmental Radioactivity; **100**; p 527-533; 2009.

[4]   Code of Federal Regulations; *Derived Air Concentrations (DAC) for controlling radiation exposure to workers at DOE facilities*; 10 C.F.R. § 835 Appendix A; 2011.

[5]   Hayes RB; *False CAM Alarms from Radon Fluctuations*; Health Phys; **85**; p S81-84; 2003.

[6]   Hayes RB; *Problems found using a radon stripping algorithm for retrospective assessment of air filter samples*; Health Phys; **94;** p 366-372; 2008.

[7] Justus AL; *Prompt Retrospective air sample analysis – A comparison of gross-alpha, beta-to-alpha ratio, and alpha spectroscopy techniques*; Health Phys; **100**-2**;** p 191-200; 2011.

[8]   Cope SJ, Hayes RB; *Validation of a Rapid, Conservative Transuranic Alpha Activity Estimation Method in Air Samples*; J Radiolog. Prot **39**, 749-765 doi. org/10.1088/1361-6498/ab1bfd.

[9]   Cope SJ, Hayes RB; *Incremental Gains in Transuranic Activity Analysis in Air Samples for Radiological Emergency Response*; Nuc Tech; . DOI: 10.1080/00295450.2019.1590074.

[10] Cope SJ, Hayes RB; *Preliminary work toward a Transuranic Activity Estimation Method for Rapid Discrimination of Anthropogenic from Transuranic in Alpha Air Samples*; Health Phys; **114**-3; p 319-327; 2018.

[11] Konzen K, Brey R; *A method of discriminating transuranic radionuclides from radon progeny using low-resolution alpha spectroscopy and curve-fitting techniques*; Health Phys; **102**; p S53-S59; 2012.

[12] Pollanen R, Siiskonen T; *Minimum detectable activity concentration in direct alpha spectrometry from outdoor air samples: continuous monitoring versus separate sampling and counting*; Health Phys; **90**; p 167-175; 2006.

Unaccounted for uncertainties in radioaerosol assays as used in plume reconstruction or treaty verification

Robert B. Hayes

North Carolina State University, College of Engineering
Nuclear Engineering Department
Retrospective Dosimetry and Nuclear Assay
2500 Stinson Dr. Raleigh, NC 27695-7909, USA
E-mail: rbhayes@ncsu.edu

Abstract:

The typical approach used in air sampling is to ascribe the radiological concentration of interest in an air sample to the ratio of filter activity to volume pulled. This attribution is reasonable provided the sample is representative, however, the uncertainties ascribed to this concentration are generally considered Poisson errors from the counting scheme used. This work will show how the actual dispersion can be one or two orders of magnitude larger in some cases even when the radioaerosol has constant specific activity due to the lognormal size distribution of the particulate sampled. Applications in plume monitoring and the actual release from the February 2014 event at the Waste Isolation Pilot Plant in New Mexico USA will be considered and presented.

Keywords: air monitoring; uncertainty; dispersion; sampling

1. Introduction

Air sampling is one of the key aspects to the comprehensive test ban treaty (CTBT) monitoring regime. Samples of interest include radioaersols (e.g., radioiodines and transuranics) along with noble gases (eg. Xe isotopes). This work addresses only the aerosol physics of this sampling but as such, it also has applicability to operational health physics and radiological emergency response. The application to the February 2014 transuranic waste drum deflagration at the Waste Isolation Pilot Plant (WIPP) in southeast New Mexico USA will be evaluated as a case in point on the effect described here [1]. The effects of aerosol physics on the sample collection will demonstrate how typical air sampling interpretations for common assays will underestimate true dispersion by as much as an order of magnitude in most cases, possibly even 2 orders.

1.1 Aerosol sampling and assay

The process for taking an air sample has largely been unchanged for the past 70 years. This method involves pulling a known volume of air through a filter and then assaying that filter. The sampled air is then ascribed a concentration value equal to the ratio of the filter assay activity to the volume of air pulled.

Typically, the volume of air is known quite precisely and the assay is constrained to Poisson statistics relegating the dominant uncertainty in the airborne concentration estimate to that of the Poisson counting in the assay.

1.2 Representative sampling

In order to obtain a quality sample, the collection of all particulate must be representative of the total population present in the space of interest. This is typically only considered to be an issue when the sampling is taking place in a duct or exhaust system. When sampling an effluent, the linear face velocity through the filter has to be equal to that of the general volume surrounding it to prevent over or under sampling of the particulate. This can be challenging when the linear flow rates of the effluent vary or are turbulent.

Undersampling is expected to occur when the linear face velocity through the filter is lower than the bulk volume around the sampling head. This will cause some of the smaller particulate to follow the flow path avoiding the filter even though it would have initially traversed it were the sampling head not present.

Oversampling is expected when the linear face velocity through the filter is higher than the bulk volume around the sampling head. This would cause particulate which otherwise would not have passed along the intake face of the filter to divert from its ambient path into the filter due to the higher sampling flow rate.

One way to overcome this challenge for dynamic flow conditions is to use a shrouded probe as shown in Figure 1 [2]. The shroud forces air through the outer channel to take a more linear path surrounding the filter's sample head and therefore can prevent any under- or oversampling.

1.3 Aerosol physics

Aerosols evolve in an effectively fractal manner. They are not generally spherical but rather dendritic and are composed primarily of organic matter, micron-sized silicates and/or ocean mist near the coast [3]. Their evolution will depend on relative humidity, particle density and types.

Typical binding forces are those of Van der Waals when gross kinetic impact of any kind occurs. Aerosol particulate growth is not spherical but erratic resulting in dynamic
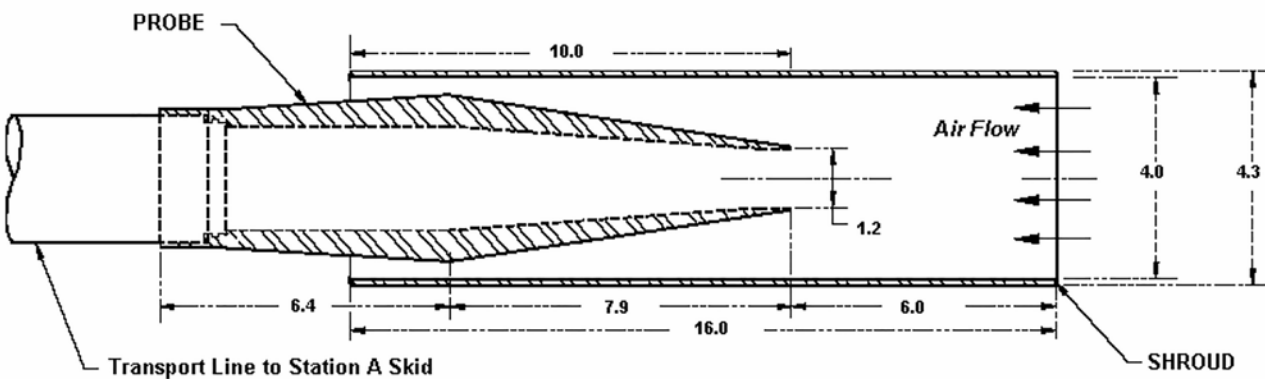
Figure 1: Shrouded probe schematic show from a cross sectional view. [2]

properties such as changing density, heat capacity and obviously aerodynamic radii. Reviews of the intricacies of these dynamic dependencies can be found elsewhere [4, 5].

1.3.1 Radioaerosol physics

Radioaerosols in particular can be extremely erratic in their evolution when they decay through charged particle emission. When a gaseous radionuclide (such as radon or its progeny) decays through charged particle emission, the resulting heavy metal gas has a charge that will induce a polarization in all nearby aerosols. The resultant dipoles in the vicinity of a point charge will result in an attractive potential to pull the radionuclide into a bound state with one or more ambient aerosols.

This additional Coulomb-based potential in radioaerosol physics only further exacerbates the evolutionary growth properties in any given species. The radical electric potential shift which can occur when spontaneous charge generation is placed on the aerosol or gas (from charged particle emission in radioactive decay) allows for rapid growth and is unique to the radioactive decay process (including recoil effects from decay such as dislodging).

A radioactive aerosol can begin as an inert isolated gaseous species such as radon, radon progeny or radioiodines. With radioiodines, these can combine with atmospheric water or other materials to become an aerosol. Radon progeny can remain as a gas through its decay series or combine with ambient aerosols to become part of the bound fraction of the progeny (conversely, that part which does not combine with any aerosols is simply the unbound fraction). These fractions are expected to depend on relative abundances of the radionuclide and ambient aerosols along with temperature, relative humidity etc.

1.3.2 Sampling physics

The action of sampling a gas or aerosol for assay requires either measurement in some in-situ fashion (generally resulting in dismal sensitivity with low concentrations) or concentrating it in some medium for characterization. With an aerosol, this is done by pulling air through a filter such

that the filter concentrates the particulate within its volume. Gaseous species are typically collected by pulling air through zeolite or activated charcoal to later be boiled off in a vacuum and then concentrated for assay.

With the air filter, there are 4 main mechanisms for fixing the analyte in the medium. These are inertial impaction (similar to a projectile into mud), interception (particles too massive to fit through the pores), diffusion (Van der-Waals adhesion) and electrostatic attraction (requiring a net charge, although not seen in Figure 2, see section 1.3.1).
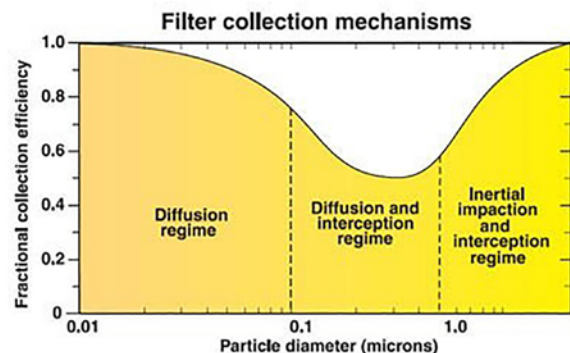

Figure 2: Filter collection mechanisms labelling dominant sampling efficiencies grouped by particle size. Note the abscissa is given in logarithmic scale. [3]

As a result of the variety of physics taking place when sampling an aerosol, the particle size collection efficiency is dependent on a number of factors (including flow rate, filter characteristics etc.). As a generalization, the particle size efficiency shown in Figure 2 can be used as a reasonable approximation to typical behaviours. Here, dominant sampling mechanism regimes are shown as a function of aerosol size.

It is significant to note that in the respirable range (when particulate is able to make it all the way down into the lung alveoli and be retained for a dose intake) is exactly where the filter efficiency is both lowest and has the largest changes (0.1 to 5 µm). This uncertainty in filter efficiency for the respirable range contributes to the reason why dose should not be ascribed to individuals based only on

air monitoring data [6] compared to the far more reliable and standard bioassay in determining actual radionuclide intake. This is one important contribution to dispersion in aerosol monitoring which is independent of the final filter assay but there are others.

2. Plume monitoring

With the advent of any nuclear detonation, leakage of the gaseous constituents from the event will then pour into the environment creating a plume. The simplest propagation model for plume evolution is probably Gaussian diffusion with advective transport. This means that as the material follows airflow, it will diffuse in all directions driven by simple Fickian mechanics. Atmospheric stratification along with ground boundaries complicate the transport along with any convective or turbulent flows.

To the extent that the plume propagation can be accurately predicted, multiple sample points would then enable characterization of the same. Two or three points are likely inadequate to fully characterize any plume unless the source term itself was already well known in time and space. Backtracking a potential plume around the globe can quickly become intractable without source term knowledge or real time monitoring of the plume itself [6].

2.1 Footprint characterization

If a known release had occurred, sampling teams would generally prefer to stay on the penumbra of the fallout footprint caused by the plume passage and deposition. This prevents the sampling teams from being required to don personal protective equipment (PPE) and so prevent skin contamination. Further, vehicle contamination would also occur if sampling missions were not constrained to the outskirts of the fallout. Any vehicle and personnel radioactivity accumulation would create the need for decontamination and so full hotline support to eventually doff the PPE and reuse of the vehicle. These activities would necessitate additional manpower and resources for decontamination rather than sampling, assessment and control.

2.1.1 Low concentration sample drivers

Due to these inhibitions from sampling in contaminated areas, only those areas that have barely detectable levels of the radionuclides of interest may be measured so that PPE is not required. Higher levels of the plume footprint are then characterized from the air using large arrays of NaI logs for gamma detection [7]. This means that air and soil samples taken from ground teams are invariably acquired from those regions of low or very low contamination.

The same result (expected low activity) is generally realized for routine air samples, even those taken from an effluent stack. This is because facility release limits are generally sufficiently low that the maximum possible public or environmental dose consequence is a small fraction of normal background dose. In order to comply with facility limits, effluent content of any controlled radionuclides have to be low. In many cases, the dominant transuranic (TRU) release content is from resuspended fallout created by atmospheric weapons testing in the past century [8]. The purpose for most air samples is to prove that no release did occur so again, overwhelmingly, air samples for controlled radionuclides have low to very low anthropogenic radionuclide content.

2.2 WIPP event

On February 14 of 2014, a deflagration took place in a TRU drum sent to the WIPP for permanent disposal by the Los Alamos National Laboratory. The WIPP facility itself is a deep salt mine and the radiation monitoring system detected the breach shifting the effluent airflow to a suite of high efficiency particulate air (HEPA) filters preventing a large environmental release. The system had a small leak due to industrial bypass filters designed for mining operations to divert the airflow which were not rated for nuclear operations (they were designed and built in the 1980's prior to modern nuclear standards for geological repository ventilation systems). The event took place while the regulatory compliant radiation monitoring system was functioning including on and offsite air sampling stations.

The resultant plume (along with offsite sampling stations labelled as pink flags) is shown in Figure 3. Here, the effluent stack was measured via representative sampling and so the plume was predicted using the national atmospheric release advisory center (NARAC) modelling code allowing comparison with offsite sampling stations [9].

2.2.1 Source of the WIPP release

The release itself was comprised of a nitric salt with around 7 curies of ^{241}Am contained therein. The cause of the deflagration was eventually traced back to the use of organic kitty litter with the nitric salt based on a miscommunication of the words, "inorganic" with "an organic". Detailed descriptions of the sequence of events culminating in the release can be found elsewhere [10].

2.2.2 Air monitoring results

A graph of the predicted versus measured air concentration values from the WIPP event is provided in Figure 4 [1, 6]. Here it is clear that at high airborne concentrations, excellent linear correlation is realized resulting in an almost unity correspondence. At lower concentrations however, a drastically larger relative deviation is clearly seen in Figure 4.
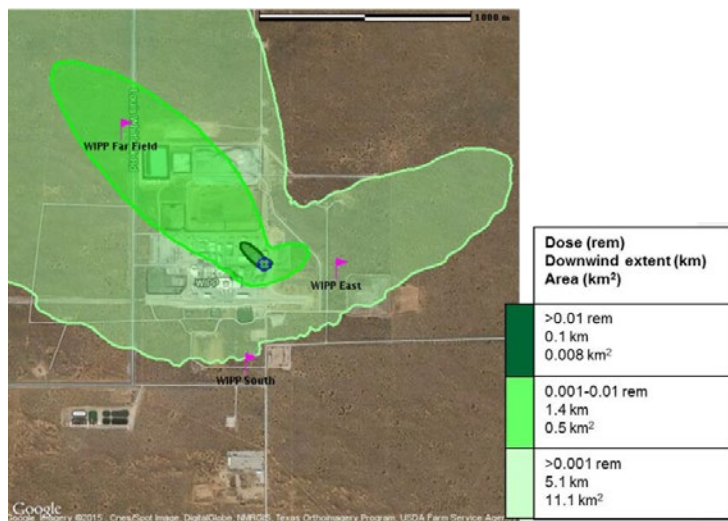
Figure 3: Dose contours determined via NARAC from the WIPP release based on effluent assays which could then be correlated with field air sampling results. Inner locations for air sampling are represented by maroon flags labelled WIPP Far Field, WIPP East and WIPP South.
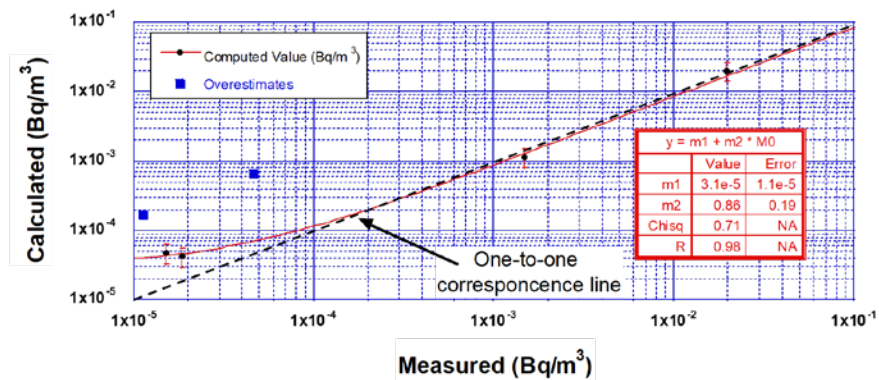
Figure 4: Plume projection predicted concentration as a function of empirical field assay values of the passing plume based on regulatory compliance air sampling infrastructure. Overestimates are also shown.

The linear correlation shown in Figure 4 does not include the pair of noted overestimates (blue squares). The agreement seen at high concentrations largely forces the high correlation. The scatter at low concentrations is noted to vary by an order of magnitude relative to the expected value with apparent presence of positive bias in overpredicting. Overpredictions will be shown later to be an expected event from small probability, large particle size radioaerosols being sampled.

3. Aerosol statistics

The shape parameter for an aerosol is based on its settling velocity in ambient air when compared to a spherical droplet of water. The equivalent water droplet with the same settling velocity as the aerosol then fixes the mass median aerodynamic diameter (MMAD). Similarly, the activity median aerodynamic diameter (AMAD) is used for defining respirable particle sizes which when inhaled can be incorporated into bodily fluids through the lung membrane of the alveoli.

An equivalence between the MMAD and AMAD can be found only when a radioaerosol has a constant specific activity. If the entire particle has uniform radioactivity present, then the activity will be directly proportional to the mass and so the reference diameter which gravitationally falls at the same rate as the standard droplets normalize them to have the same size distribution values of mode, median and mean as shown in Figure 5.

3.1 Lognormal

The functional relationship describing the shape distribution of aerosols (Fig. 5) is given by Equation 1. Here, the argument of the exponential is a logarithmic abscissa and so a typical shape for a 5 μm MMAD aerosol is shown in Figure 5. Here, the skew is evident in that the parameter describing the shape equivalent of a standard aerosol (MMAD or equivalently the AMAD) is far up into the tail and very different than the mode or median.

$$f\left(x;\mu,\sigma^2\right) = \frac{1}{\sqrt{2\pi}\sigma x} e^{-\left[\ln(x)-\mu\right]^2/\left(2\sigma^2\right)} \tag{1}$$
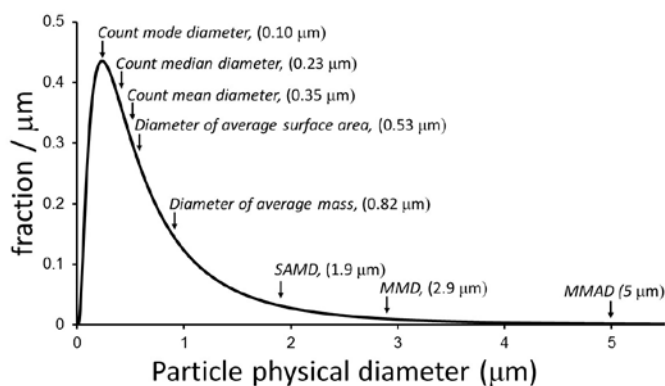
Figure 5: Probability distribution of 5 μm AMAD particles as a function of their particle physical diameter [11]. Marked in the figure are many properties of potential significance in evaluating statistical properties of a distribution from an aerosol with an AMAD of 5 μm. Other metrics shown in the figure for aerosol shape characterization are the surface aerodynamic mean diameter (SAMD) and the mass mean diameter (MMD, not the median) which use different properties of the aerosol as the weights in obtaining the average for a distribution.

The basic probability density function is approximated here by Equation 1 where more detailed physical interpretations can be obtained elsewhere [12]. An example of such a distribution is shown in Figure 5 where a frequency distribution of various diameter related metrics are provided. Here, the mode (0.1 μm) is recognized to be less than half the median (0.23 μm) which is more than an order of magnitude below the effective mean or the mass median aerodynamic diameter (MMAD at 5 μm). It is the MMAD (effectively equivalent to the activity median aerodynamic diameter or AMAD) which is standardized based on settling velocities compared to a monodisperse material such as water. This is important given the dependency on the effective shape distributions driven by conforming to Equation 1 relative to the total respirable fraction present. This can become much more complicated with multimodal distributions although these are assumed simple superpositions of multiple lognormals.

3.1.1 Health consequences

The drastic skew in particle size distributions of an aerosol (Fig. 5) can significantly affect the inhalation intake from incorporation into bodily fluids through transfer across the tissue interface of the lung alveoli. The respirable range is generally in the 0.1 to 5 μm range where most planar disc air sample filters have the largest variation in collection efficiency as seen in Figure 2.

If the shape distribution peaks (has a mode) in the respirable range where sampling efficiency demonstrates the largest variability (Figure 2), evolution in the peak location will only exacerbate the resultant health effect dispersion. This contributes to overall error but the true uncertainty has to also account for sampling statistics driven by the distributions following the form of Equation 1.

3.1.2 Sampling statistics

By definition, a small number of aerosols sampled from the diameter distribution shown in Figure 5 will likely come from the mode. On average, half of these should be above the median which itself is just over double the mode. The dispersion in diameters sampled for a small sample number would then be expected to look like a Gaussian, centered between the mode and median in this sense.

The population however has members with sufficiently large diameters which cause the aerodynamic average to be more than an order of magnitude larger than either of the erroneous Gaussian approximations to the mode or median. Based on the frequency distribution seen in Figure 5, the probability of sampling a very large diameter particle is vanishingly small. If the activity of each aerosol particle is uniform throughout its volume, then the true sampling dispersion can become egregious at best considering the effects of these very large particulates in the assay.

3.1.3 Shape parameter dependencies

The shape of the distribution seen in Figure 5 is strongly dependent on the geometrical standard deviation of the lognormal. A family of curves for the lognormal having different shape parameters are shown in Figure 6 where each curve shown has the same integrated area (note both base axes are not linear in the traditional sense as log(x) is plotted as an axis).

Here the family of curves is normalized to have the same integral to highlight the large variation possible from a lognormal distribution, specifically when they all have equivalent probability interpretations. This results in each curve having a different mode, median and mean. The curves are graphed together along the sigma scale for display only and not intended to describe the expected distribution of any specific sample as real world distributions can be multimodal and dynamic.

3.1.4 Monte Carlo modelling

A normal random variable of mean $\bar{x}$ and variance σ^2 is represented by $N\left(\bar{x}, \sigma^2\right)$. A normal random variable with zero mean and unity variance is represented by the symbol $N(0,1)$. This was used to create a lognormal distribution in the form of $e^{N(0,1)}$ such that it would have a mode of $e^{-1}=0.37$ μm, a median of $e^0=1$ μm, and a mean of $e^{1/2}=1.65$ μm. With this mean radius, the average diameter then becomes 3.3 μm which places it in the range of the most penetrating size for biological intake and so makes for a simplified mathematical example for consideration.

A random sampling from the $e^{N(0,1)}$ distribution was done using a generated normal random variable in Microsoft Excel to allow for simulating these effects. Doing this 1E6 times resulted in the overall distribution shown in Figure 7 where the insets show the distribution's appearance when displayed with differing logarithmic axes. The upper center inset has
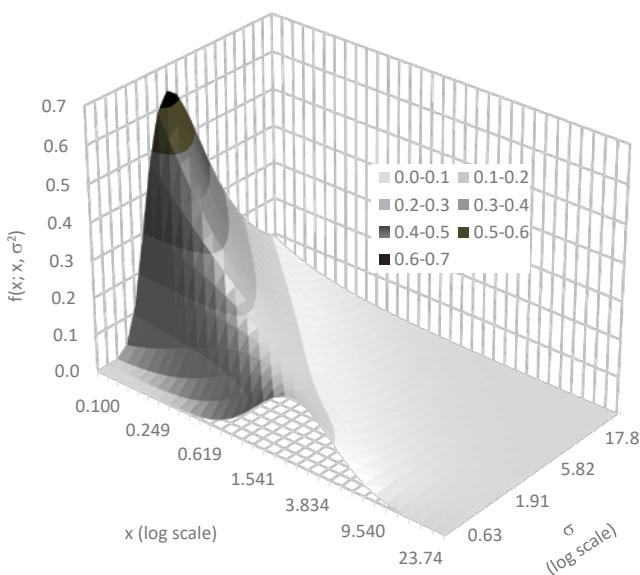
Figure 6: Family of lognormal distributions having a mean μ=1.5 µm based on a progressive increase in shape parameters as listed in the legend. Note the shape parameter is the σ value in Equation 1.

a logarithmic abscissa resulting in an apparent normal distribution. The upper right inset has a logarithmic ordinate axis showing the effect of the unique tail approximated by the Monte Carlo calculation.

Taking a random sample from a lognormal population distribution will then result in a dispersion strongly dependent on sample number. As the sample number becomes large, the true lognormal distribution will by definition be observed. Smaller sets will appear normal demonstrating skew with increasing sample size. Estimating this effect by simple Monte Carlo sampling from the population probability density function can provide a good estimate on these effects.

3.1.4.1   Normal variance as a function of sample size

Due to the choice of a simplified distribution parameter set, the normal standard deviation as a function of sample size is $\sigma(n)$ then given by the expectation function $\sigma(n) = \sqrt{\left(E(\bar{x} - x)\right)^2}$ such that when $\sigma(n) = 2/\sqrt{n}$ for the

particle radii distribution. This means that at the upper 95% confidence level (CL), the limit becomes $3.29/\sqrt{n}$ which relative to the defined mean (e.g. AMAD) value of $\bar{x}$ =1.65 shows that there must be at least 4 randomly sampled aerosol particulates to have a normal standard deviation of 2. This may not seem terrible at first glance but note that the activity of a transuranic or similar radioaerosol will not scale with the radii but rather the radii cubed. With low particle numbers, this activity value becomes large, effectively an order of magnitude.

A very relevant question then becomes the effect of those instances when a low probability aerosol of a large diameter is sampled from the distribution given that very large radii are possible from this very simple distribution (>20 µm, Figure 7, $e^{N(0,1)}$). Here, the activity (or mass) scales with the effective radius cubed. A singe 2.2 µm radius particle will have 10 times the activity of a single 1 µm radii particle. Likewise, a 1 µm radius particle will have 1000 times the activity of a 0.1 µm particle. More egregious cases could be considered (e.g. multimodal distributions etc.) but the salient point is that this is truly an independent dispersion source in the overall assay results.

4.   Discussion

Applications of this work in treaty verification and plume monitoring demonstrate how plume density or activity measurements will have large dispersion from penumbra samples where particulate density is low or very low. Unless the aerosol itself is not homogenous in composition, this will only effect integrated activity or centerline projection estimates. The key facet in aerosol physics directs that the dispersion mechanisms do not change the average as a whole but only the variance of that mean if more common statistics (normal or Poisson) are assumed. Correspondingly, a small sample number from low concentration air will be expected to have very high dispersion as seen empirically from historical air monitoring assays when the sampled particulate number is small [13].
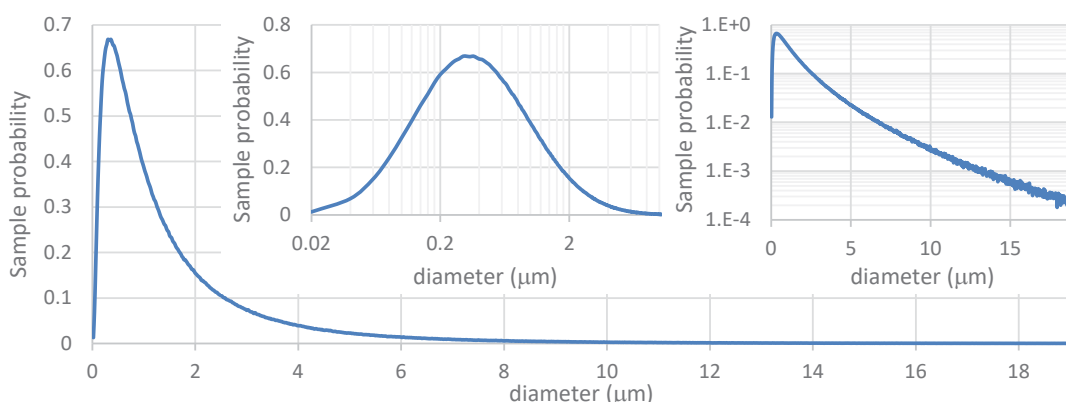
Figure 7: Monte Carlo calculated standard lognormal probability distribution from 1E6 values generated from exp(N(0,1)). This distribution has a mode at 0.34 µm, a median at 1.0 µm and a mean at 1.65 µm.

The key finding here considers that the Poisson dispersion in air filter assays may actually prove to be an insignificant contribution to the overall uncertainty in the characterization effort of any airborne contamination events. The extent to which this dispersion plays a role will be dependent on a product of the sample volume and actual airborne contamination concentration as this will scale the number of particles acquired on the filter media. Assays of high activity samples will not be subject to this additional dispersion effect to the same extent as the low activity samples and so can be considered accordingly.

The functional dependence of particle size distributions was demonstrated using a mathematically simplified distribution scaled to have relevance to radiological risk scenarios for aerosol assay. More egregious cases could be constructed as done elsewhere [6] although clearly, less egregious cases could also be constructed and considered realistic for potential real world applications in operational health physics scenarios. The moderate approach utilized here was offered as an insightful perspective into the effects from particle size distributions in final assay results and their interpretations.

5. Conclusions

This work has shown that the true dispersion in most radioaerosol samples can potentially be orders of magnitude larger than the uncertainty ascribed only from Poisson counting errors in the sample assay. Interpretations which require quantitative estimates of the radiological concentration then are subject to additional uncertainty terms which have not historically been considered when characterizing radiological air sample assay results.

6. Acknowledgements

7. References

[1] Hayes RB; (2016) Consequence assessment of the WIPP radiological release from February 2014. *Health Phys.* **110**(4), 342-360.

[2] Frank-Supka L, Harward DJ, Casey SC; *Overview of the WIPP Effluent Monitoring Program, Compliance with Title 40 CFR Part 191, Subpart A, Environmental Standards for Management and Storage* US Department of Energy, Carlsbad New Mexico, May 2005. Last accessed 4/19/2019 https://wipp.energy.gov/library/Overview_WIPPEffluentMonitoring.pdf

[3] Maiello ML, Hoover MD Editors; *Radioactive Air Sampling Methods*, CRC Press, Boca Raton, FL, 2011.

[4] Kleinstreuer C, Feng Y. Computational Analysis of Non-Spherical Particle Transport and Deposition in Shear Flow With Application to Lung Aerosol Dynamics—A Review. *ASME. J Biomech Eng.* 2013;**135**(2):021008-021008-19. doi:10.1115/1.4023236

[5] Vehkamäki H, Riipinen I, Stockholms universitet, Naturvetenskapliga fakulteten, Institutionen för tillämpad miljövetenskap (ITM). Thermodynamics and kinetics of atmospheric aerosol particle formation and growth. *Chemical Society reviews*. 2012;**41**:516-5173.

[6] Hayes RB. (2017) Reconstruction of a radiological release using aerosol sampling *Health Phys*. **112**(4), 326-337.

[7] Hendricks T, Hayes R. Enhancement of aerial gamma surveillance utilizing complementary characteristics of NaI and HPGe detection. *1st Joint Emergency Preparedness and Response/Robotic and Remote Systems Topical Meeting*. Salt Lake City, UT, February 11-16, 2006. ISBN: 978-0-89448-692-0 CD-ROM.

[8] Hayes RB, Akbarzadeh M. (2014) Using isotopic ratios for discrimination of environmental anthropogenic radioactivity. *Health Phys*. **107**, 277-291.

[9] Hayes RB. (2016) Consequence assessment of the WIPP radiological release from February 2014. *Health Phys*. **110**(4), 342-360.

[10] Accident Investigation Board. *Radiological Release Event at the Waste Isolation Pilot Plant, February 14, 2014*. US Department of Energy, Carlsbad, New Mexico. April 2015. Accessed 4/20/19 https://www.wipp.energy.gov/Special/AIB_WIPP%20Rad_Event%20Report_Phase%20II.pdf

[11] Hoover MD. SC 2.6: *Radiation Safety Aspects of Nanotechnology*. National Council on Radiation Protection and Measurements, Bethesda MD 2016

[12] Crow EL, Kunio Shimizu K, Editors; *Lognormal distributions: theory and applications.* Taylor and Francis, London, 2017

[13] Alvarez JL, Bennett WS, Davidson TL; Design of an Airborne Plutonium Survey Program for Personnel Protection. *Health Physics*. **66**(6):634-642, June 1994.

Export control and nuclear safeguards

Filippo Sevini, Guido Renda, Simone Cagno, Xavier Arnes Novau, Christos Charatsis, Willem Janssens

European Commission Joint Research Centre
Directorate Nuclear Safety and Safeguards
Via Enrico Fermi, 2749
21027 Ispra, Italy
E-mail: filippo.sevini@ec.europa.eu

Abstract:

The control of strategic trade has been set up progressively in the past five decades as a barrier against the diffusion of sensitive materials, components and technologies, which could be used for the proliferation of nuclear, biological and chemical weapons of mass destruction and their means of delivery.

The result has been a continuously evolving multi-layered regime which comprises treaties, international agreements, UN Security Council Resolutions, embargo measures and national laws. In particular, nuclear export controls and international safeguards have developed in parallel in phases triggered by major international events, which showed that the insufficient scope of the controls existing at that time, as well as the legal framework's loopholes could be exploited to acquire sensitive goods. Although not implementing export controls, the IAEA benefits from their existence and from the inclusion of Model Additional Protocol's requirements related to its Annexes I and II that also provide background information for IAEA's verification activities.

The paper reviews the background and key aspects of strategic export controls, discussing their contents and relevance to countering the proliferation of weapons of mass destruction as well as the synergies with nuclear safeguards, describing challenges and open issues.

Keywords: export control; nuclear safeguards; non-proliferation; dual-use; strategic trade

1. Strategic export control and nuclear safeguards

Strategic export control is a barrier against proliferation called for by United Nations Security Council Resolution 1540 [1], aiming to limit the unauthorized access to strategic technology and goods.

Export control and nuclear safeguards developed in parallel, as two intimately linked elements of the non-proliferation framework. This link is evident in both the Non Proliferation Treaty [2] and the Nuclear Suppliers Group (NSG) Trigger List guidelines [4]:

- The Non Proliferation Treaty's Art. III.2. subjects the export of nuclear items to international safeguards

- Safeguards are a condition of supply for nuclear goods also clearly stated by the Nuclear Suppliers Group's Trigger List guidelines [4, Art. 4].

1.1 The Non-Proliferation Treaty (NPT)

The close relationship between export control and nuclear safeguards is clearly visible in the NPT Article III.2's requirement for safeguards as a principal condition of the supply of nuclear items:

> *Each State Party to the Treaty undertakes not to provide: (a) source or special fissionable material, or (b) equipment or material especially designed or prepared for the processing, use or production of special fissionable material, to any non-nuclear-weapon State for peaceful purposes, unless the source or special fissionable material shall be subject to the safeguards required by this Article.*

The need to interpret the term "especially designed or prepared for" components led to the formation of the NPT Exporters' (or Zangger) Committee, which could not come up with a definition but instead identified a list of key nuclear fuel cycle items. The resulting "Trigger List" (i.e. a list of equipment and facilities "triggering" the need for safeguards) and guidelines for the supply were communicated to Member States by the IAEA in INFCIRC/209 latest revision is reported in [6].

1.2 The Nuclear Suppliers Group (NSG)

In line with the NPT provisions, many steps were undertaken for the development of international nuclear safeguards, with the objective of "*preventing diversion of nuclear energy from peaceful uses to nuclear weapons or other nuclear explosive devices. [...] The safeguards [...] shall be applied on all source or special fissionable material in all peaceful nuclear activities within the territory of such State, under its jurisdiction, or carried out under its control anywhere.*" (NPT, art. III.1).

The effort led to the definition of a Comprehensive Safeguards Agreement (CSA – INFCIRC/153) defining how IAEA safeguards would be implemented in NPT States in compliance with the NPT Article III.1

The Indian "peaceful nuclear explosion", in 1974 showed that, notwithstanding the entry into force of the Non

Proliferation Treaty, various countries had anyway exported nuclear technology to India, a non-signatory to the Treaty.

To address this gap, a group of nuclear supplier states decided to form the "Nuclear Suppliers Group (NSG)" [3] which, like the Zangger Committee, also issued additional Guidelines in 1978, published as INFCIRC/254/Part 1 and including an extended Trigger List [4].

The NSG has been quite active since its establishment, growing its membership to the current 48 Participating Governments, plus the European Commission as observer.

The results of its work are two distinct NSG guidelines, respectively the:

- "Guidelines for nuclear transfers" setting the conditions for transfers of nuclear items (i.a. nuclear safeguards and physical protection requirements) and containing two annexes, where Annex B contains the Trigger List (TL)
- "Guidelines for transfers of nuclear-related dual-use equipment, materials, software and related technology", containing in annex the Dual-Use List (DUL) [5]

The creation of the second set of guidelines covering dual-use equipment was decided in 1992, after the discovery of the covert Iraqi nuclear programme, supported also by the illicit import of non-Trigger List goods and technology.

2. International Safeguards framework

The discovery of undeclared proliferation activities in Iraq in 1991 was also a turning point for what concerns the international safeguards framework.

After having implemented Comprehensive Safeguards Agreements (CSA) with a focus on declared nuclear material at declared facilities for decades, the discovery of the Iraqi military nuclear programme in the 1990s led the IAEA and its Member States to start a paradigm shift for the implementation of NPT safeguards, from both a legal and practical point of view. From a legal point of view, the introduction in 1997 of the "Model Protocol Additional to the Agreement(s) between State(s) and the International Atomic Energy Agency for the Application of Safeguards" (AP - INFCIRC/540) [7] expanded the set of information the State transmits to the Agency under their reporting obligations and expanded the verification toolkit at the IAEA disposal to exclude the presence of possible undeclared nuclear material and activities in a State.

2.1 Model Additional Protocol

The Additional Protocol's Article 2.a. requires that States:

.... shall provide the Agency with a declaration containing:

(i) A general description of and information specifying the location

of nuclear fuel cycle-related research and development activities

not involving nuclear material...

and

...

(iv) A description of the scale of operations for each location engaged

in the activities specified in Annex I to this Protocol.

Annex I lists fifteen key nuclear fuel cycle related activities:

i. The manufacture of *centrifuge rotor tubes* or the assembly of *gas centrifuges*.
ii. The manufacture of *diffusion barriers*.
iii. The manufacture or assembly of *laser-based systems*.
iv. The manufacture or assembly of electromagnetic isotope separators.
v. The manufacture or assembly of *columns* or *extraction equipment*.
vi. The manufacture of aerodynamic separation nozzles or vortex tubes.
vii. The manufacture or assembly of uranium plasma generation systems.
viii. The manufacture of *zirconium tubes*.
ix. The manufacture or upgrading of *heavy water or deuterium*.
x. The manufacture of nuclear grade graphite.
xi. The manufacture of flasks for irradiated fuel.
xii. The manufacture of *reactor control rods*.
xiii. The manufacture of criticality safe tanks and vessels.
xiv. The manufacture of irradiated fuel element chopping machines.
xv. The construction of *hot cells*.

2.a.(i) allows the IAEA to identify those research activities which carry out potentially sensitive and relevant research, which could be transferred "intangibly" violating the export control provisions (Intangible Transfers of Technology). These R&D sites would not appear in the declarations under 2.a.(iv) because not linked to the actual presence of nuclear material and can therefore be captured by the requirement of 2.a.(i).

The AP also requires export declarations of "Trigger list" items (see above NSG) listed in its Annex II, related to nuclear activities listed in Annex I.

Annex B item	Title	Since	Year
1.8	Nuclear reactor internals[1]	Rev. 3	1997
1.9	Heat exchangers	Rev. 3	1997
1.10	Neutron detectors	Rev. 3	1997
1.11	External thermal shields	Rev. 12	2013
3.5	Neutron measurement systems for process control	Rev. 12	2013
5.2.1.c	Solidification or liquefaction stations	Rev. 12	2013
5.2.3	Special shut-off and control valves	Rev. 9	2007
6.8	Complete heavy water upgrade systems or columns therefor	Rev. 3	1997
6.9	NH_3 synthesis converters or synthesis units	Rev. 12	2013
7.1.9	Especially designed or prepared systems for the conversion of UO_2 to UCl_4	Rev. 4	2000

Table 1: Items part of the NSG Trigger List (Annex B of INFCIRC/254 Part 1, as of Revision 14 of 2019), which are not listed as such in Annex II of the Additional Protocol (INFCIRC/540c), with their year and revision of appearance in the Trigger List. The table does not contain items that have only been amended (e.g. code, title, text) in the Trigger List since 1995.

Art. 2.a.(ix) of the AP requires that States:

…shall provide the Agency with a declaration containing the following information regarding specified equipment and non-nuclear material listed in Annex II:

For each export: the identity, quantity, location of intended use in the receiving State and date … of export;

Upon specific request, confirmation as importing State of information provided by another State concerning the export of such equipment and material

Annex II lists the items contained in the NSG Trigger List (INFCIRC 254/Part 1) available in 1995 (Rev. 2). Unfortunately, the AP Annex II list has not been amended thereafter, unlike the NSG TL, amended already several times (the current version being Rev. 14 of 2019). This fact creates discrepancies to exporters and authorities which is addressed in various practical ways as outlined in [8,9].

The States or other organizations depending on the countries' attribution of competences (e.g. EURATOM for some European Union Member States), are responsible for retrieving AP-related information and provide it to the IAEA along with the CSA-related and other required declarations. The experience of some ESARDA members with the activities and export declaration provisions of the AP is summarised in [10].

2.2 State Level [safeguards] Approaches

From a practical point of view, building on both CSAs and the AP, the current IAEA nuclear safeguards framework (the so-called State Level Concept –SLC) foresees the application of "State Level [safeguards] Approaches" (SLA),

uniquely tailored to each State, with the objective to detect any NPT non-compliance, spanning from detection of diversion of declared nuclear material to the detection of undeclared nuclear activities at undeclared sites.

For the design and conception of a SLA (Figure 1), the IAEA evaluates all the possible routes to achieve weapons-useable material in a given State through the application of Acquisition Path Analysis (APA). In order to assess the plausibility of each proliferation path, the Agency evaluates its potential time to completion, which in turn depends, *inter alia*, on the State's technical and industrial capability.
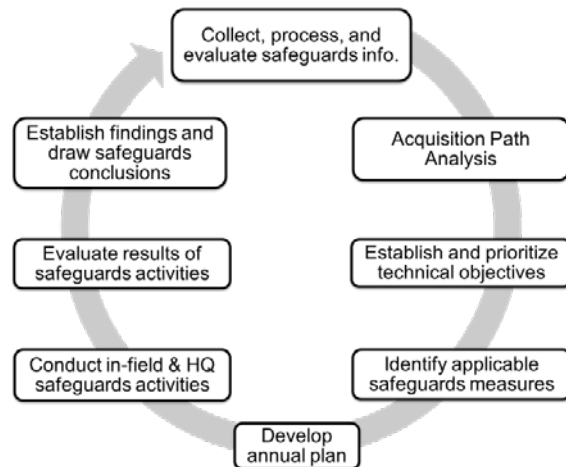
Figure 1: Flow chart of processes supporting State-level safeguards implementation, adapted from [11].

2.3 SLA Acquisition Path Analysis

An acquisition path is defined as a sequence of activities which a State could consider in order to acquire a Significant Quantity of weapons usable material. The APA is a key

---

[1] Only mentioned in the Explanatory Note to item 1.2 (Reactor pressure vessels) in Annex II of the Additional Protocol

element of the SLC. By considering the State's nuclear profile, the APA generates a list of acquisition paths ranked by their attractiveness for the State. The acquisition path analysis (APA) analyses all conceivable acquisition paths, retaining only those that could be completed within a short period, aiming to optimise the design of sets of safeguards measures focusing on the critical (more plausible) paths, while maintaining the desired efficiency and effectiveness standards. Currently, this process is mainly based on expert judgment. However, comprehensive guidance is available, since the IAEA's requirements state that APA must be objective, reproducible, transparent, standardized, documented and as a result non-discriminatory [12].

Within the APA, the information and insights coming from the export control regime and the trade analysis of dual-use and non-dual-use goods and equipment has the potential to play a very important role in understanding the technical and industrial capability of a State and the direction in which it is evolving. Together with all the other information and analyses performed by the IAEA, these insights enable a more effective acquisition pathway analysis and therefore a more efficient design of the SLA.

A central tool at the IAEA's disposal to support the identification and the characterization of acquisition paths in a State's nuclear fuel cycle is the Physical Model [13]. The Physical Model is a full description of the nuclear fuel cycle, internal to the IAEA's Department of Safeguards, subdivided into several volumes. It contains indicators (materials, equipment, technology, observables) of nuclear activities with different degrees of strength. Some material and equipment indicators are linked with explicit references in the text to controlled items and, through e.g. NSG Handbooks, to Harmonised System's customs codes.

Whereas the detection of exports of Trigger List items to a State where the nuclear activity using these items is not declared to the IAEA would clearly indicate covert nuclear activities, the export of dual-use items is more difficult to put in relation to undeclared activities. Nevertheless, the dual-use items contained in the Nuclear Suppliers Group's Guidelines are part of, and referenced in the IAEA's Physical Model. Tracing transactions based on customs commodities is one of the detection activities performed by IAEA as part of their verification process, and dedicated tools have been developed by the JRC to facilitate this [14].

3. Strategic Trade Control related sources of Information

The IAEA does not implement export controls, but benefits from their existence.

Besides the data formally due by States and collected during regular inspection activities, the IAEA makes wide use of various sources of information to detect potential indicators of undeclared nuclear material and activities, and for States with an AP in force, be able to derive broader conclusions on the absence of undeclared nuclear material and activities.

Apart from regular open-source information, these include trade data analysis, based on customs data, together with the analyses of actual and attempted covert procurement for nuclear-related goods (both single and dual-use) – information which is received from States and their companies on a voluntary basis [15]. Cross-matching the declarations with data sources used in verification may provide red flags that require further assessment.
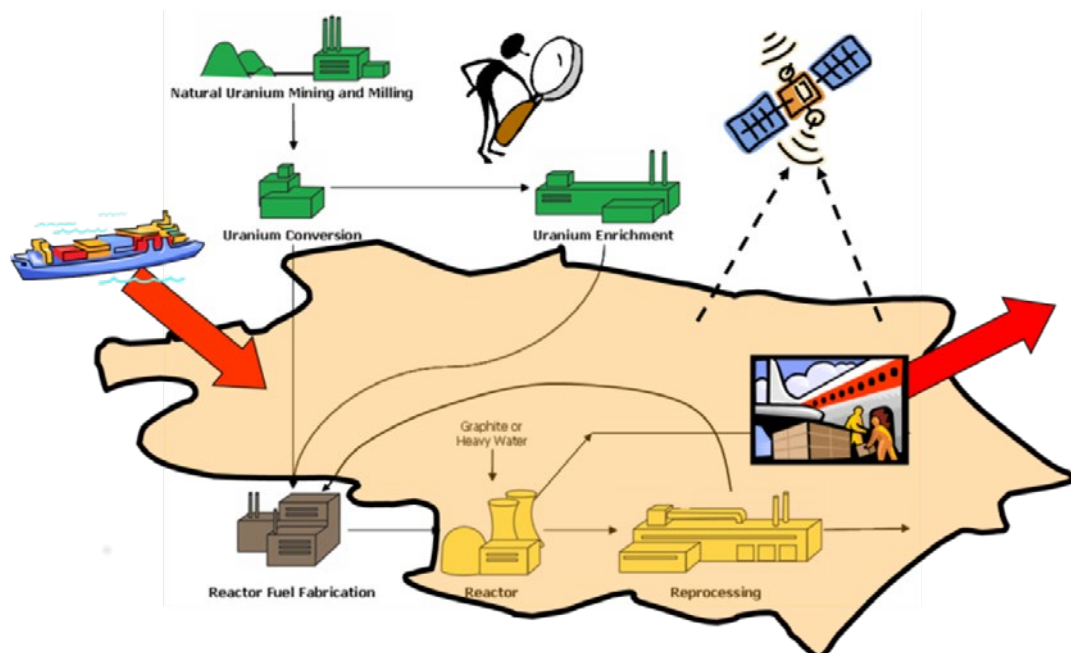

Figure 2: Matching State's declarations and verification activities

The strategic export control framework not only provides an important barrier to proliferation, it also helps generating data instrumental to the verification process. The following paragraphs describe some of the potential sources of information within the strategic export control framework.

3.1 Strategic Trade Data

For the analysis of strategic trade data, analysts can use international trade databases, which are provided by several web services; notably, under WTO rules, almost all States provide data on their imports and exports in thousands of commodities to UN Comtrade. Export-controlled items listed in regulatory documents represent a limited amount of the international trade volume covered by trade databases, which include all commodities.

As previously seen, Trigger List or dual-use items can be associated to specific parts of the nuclear fuel cycle. In order to acquire additional information on a State's nuclear-related trade, the selected items' Harmonized System codes can then be obtained, by which trade data can be retrieved from data providers [14].

The process is complicated by the fact that the commodities' categorisations used by licensing (e.g. the EU dual-use control list [16, 17]) and customs (Harmonized System) differ and the correlation between the two datasets is not one-to-one.

3.2 Denied export authorisations

Although the members of the regimes and the EU member states among them, exchange information about denied export authorisations, these are not directly available to the IAEA. The associated information may be relevant to verification activities, also for dual-use items not directly nuclear-related, including catch-all clauses on non-listed items.

3.3 Intangible Technology Transfers

Technology according to the NSG guidelines is the knowledge needed to perform an activity. Like items, components and materials, also software and technologies are subject to export authorisations and may be a proof of illicit transfers and undeclared activities. However, software and technology's export declarations are not included in AP's Annex II.

Although the availability of technology (and software to model, assist the processes) may be described in association to AP Annex I's list of activities, their transfer to third country's entities is therefore not due to be declared to IAEA. We have therefore an inconsistency and distortion with respect to the national export control systems and NSG guidelines.

In the Additional Protocols of the NWSs, there are however provisions to report to the IAEA nuclear fuel cycle-related research and development in cooperation with NNWSs [Ref: INFCIRC/263/Add.1, INFCIRC/288/Add.1, INFCIRC/290/Add.1, INFCIRC/327/Add.1, INFCIRC/369/Add.1, INFCIRC/754/Add.6] – which to some degree cover intangible technology transfers. Also, the model AP Article 2 a. (i) requires States to report NFC-related R & D, and these declarations often include R& D conducted in cooperation with entities in other States.

Linked to this, also the on-site provision of technical assistance and associated technology transfer is subject to national authorisation, although for the time being the EU export control framework still has it as a Joint action process separate from the dual-use export control requirements.

Technical assistance is also an activity performed by the IAEA itself through its Technical Cooperation programme, and can constitute an additional source of indicators for third countries.

4. Compliance and procurement outreach

The implementation of strategic trade controls and nuclear safeguards can be effective only relying on informed, aware, collaborative and complaint suppliers and exporters. For this reason also, the IAEA encourages suppliers to provide information on procurement attempts for nuclear-related (dual and single use) goods, what constitutes a valuable source of information to enable the early detection of potential undeclared nuclear activities.

Export compliance is a two way process and public authorities should promote an engaging and trusted relationship with the exporters that can be facilitated by an effective outreach strategy and open contacts and communication with the exporters. Industry can apply due diligence procedures and develop Internal Compliance Programmes (ICPs) as one of the most effective ways in addressing proliferation risks and ethical sensitivities, also besides those foreseen in the law.

The supply chain diversity presents threats and complexities. Nuclear exporters are willing to comply but challenges like the illustrative character of the TL may create interpretation issues. Some States interpret it as an indicative list while others consider that TL export controls only apply to the items specifically mentioned on the list.

More broadly, interpretation issues and "catch-all" controls relate not only to dual-use items originating from the Nuclear Suppliers Group, but also from all the international export control regimes [18,19,20,21], included for the EU in the dual-use control list published every year as Delegated Act [16], amendment to the EU Dual-use Regulation's Annex I [17], and adopted also by several non-EU countries.

Governments should strive to apply controls consistently without interfering with legitimate business or distort competition. This needs to take into account complex supply chains involving several actors (suppliers, clients, brokers, shippers, sub-contractors, banks, research, consultancy and others).

Certain emerging technologies may also provide opportunities with regards to export compliance. Modern approaches like Distributed Ledger and Blockchain could facilitate the logistics and document access all along the supply chain thus improving the processes and speeding up shipments across the controls [22].

Increased and smarter awareness is a key to a successful control of possible sensitive transfers, avoiding also to unduly hinder research and development, as well as legitimate trade.

5. Conclusions

The paper revisited the parallel evolution of international nuclear safeguards and export controls, underscoring once more their close and complementary relationship, which should be continuously reinforced in order to more efficiently counter nuclear proliferation in violation of the NPT.

The various components of the safeguards and export control framework all contribute to the prevention and verification of the absence of undeclared nuclear activities potentially aiming at the development of nuclear weapons and means of delivery.

Various declarations are due to IAEA and EURATOM, and sources of independent information can help identifying anomalies and inconsistencies, whenever made available.

In the framework of the Additional Protocol (AP), information is exchanged with the IAEA about real exports of nuclear technology. Additionally the IAEA has arrangements with some States to exchange information about refused export control licenses. This provides the IAEA with the possibility to detect at an earlier stage illicit trafficking networks. However, monitoring technology transfers by intangible means poses its own set of problems.

Countries with an Additional Protocol in force are inherently more safeguarded and thus having an AP in force minimizes proliferation risk, making positive export licensing decisions easier to make. The existence of an AP is also a key instrument for the IAEA to use to derive State Level conclusions.

The reporting requirements to IAEA do not cover supply of Trigger List technology, as there are no physical exports, nor customs declarations to complete. States may anyway report also such transfers, where they are known, on a voluntary basis.

The role of suppliers and exporters is crucial to the success of the system, at the same time safeguarding legitimate trading activities from unnecessary burden and delays. Collaboration and exchanges with suppliers is key to defining complete and workable guidelines and procedures.

The ESARDA Export Control Working Group – bringing together various stakeholders, including representatives of larger nuclear industries, authorities, universities, research institutes and NGOs – provides a multi-disciplinary open forum to exchange views for the potential benefit of safeguards and export controls. Exchanges on this subject are also taking place with INMM, supported by discussions at symposia and joint meetings that could hopefully intensify further in the future.

6. References

[1] United Nations Security Council. Resolution 1540 Adopted by the Security Council at its 4956th Meeting, on 28 April 2004, S/RES/1540, 2004

[2] IAEA INFCIRC/140 - TREATY ON THE NON-PROLIFERATION OF NUCLEAR WEAPONS (1970)

[3] Nuclear Suppliers Group, NSG, www.nuclearsuppliersgroup.org

[4] IAEA INFCIRC/254/Rev.14/Part 1, GUIDELINES FOR NUCLEAR material, equipment and technology, available at www.nuclearsuppliersgroup.org

[5] IAEA INFCIRC/254/Rev.10/Part 2 GUIDELINES FOR TRANSFERS OF NUCLEAR-RELATED DUAL-USE EQUIPMENT, MATERIALS, SOFTWARE, AND RELATED TECHNOLOGY, available at www.nuclearsuppliersgroup.org

[6] Zangger Committee, www.zanggercommittee.org

[7] IAEA INFCIRC/540 (Corrected). Model Protocol Additional to the Agreement(S) Between State(S) and the International Atomic Energy Agency for the Application of Safeguards, (1997).

[8] Filippo Sevini, Renaud Chatelus, Malin Ardhammar, Jacqueline Idinger, Peter Heine, States' reporting of Annex II exports (AP) and the significance for safeguards evaluation, IAEA SG Symposium 2014

[9] F. Sevini, Nuclear export controls update, paper presented at the 55th INMM annual meeting, 2014, Atlanta, USA

[10] F. Sevini et al., Some ESARDA Parties' experience with Additional Protocol export control declarations, paper presented at the 33rd ESARDA Symposium, Budapest 2011, available at https://esarda.jrc.ec.europa.eu/

[11] "The Conceptualization and Development of Safe-guards Implementation at the State Level," International Atomic Energy Agency, Available at: http://www.isisnucleariran.org/assets/pdf/GOV201338.pdf, GOV/2013/38, Aug. 2013; "Supplementary Document to the Report on The Conceptualization and Development of Safeguards Implementation at the State Level," GOV/2014/41, available at: https://armscontrollaw.files.wordpress.com/2014/09/iaea-state-level-safeguards-document-august-2014.pdf

[12] C. Listner et al: "Approaching Acquisition Path Analysis formally – a comparison between AP- and Non-AP States", ESARDA Symposium 2013, 27-30 May, Bruges, Belgium

[13] Z. Liu, S. Morsy, Development of the Physical Model, Proceedings of the IAEA Safeguards Symposium, vol. 29, IAEA, Vienna, 2007.

[14] C. Versino, A. El Gebaly, E. Marinova, C. Pasterczyk, G.G.M. Cojazzi, Integrating IAEA's Physical Model with JRC's The Big Table Document Search Tool, JRC Scientific and Policy Report, 2013, EUR26215 EN.

[15] M. Ardhammar, "Trade and procurement analysis in the context of IAEA safeguards", Presentation at ESARDA Joint meeting on „IAEA State Level Concept",
Nov 12, 2013, Ispra ,12 November 2013; M. Ardhammar, "Responding to Verification Challenges Caused by Increasing Nuclear-Related Trade", Presentation at Symposium on International Safeguards, 5-9 November 2018.

[16] COMMISSION DELEGATED REGULATION (EU) 2018/1922 of 10 October 2018

[17] Council Regulation No 428/2009 of 5 May 2009 setting up a Community regime for the control of exports, transfer, brokering and transit of dual-use items (Recast), (2009).

[18] Missile Technology Control Regime, www.mtcr.info

[19] Australia Group, www.australiagroup.net

[20] Wassenaar Arrangement www.wassenaar.org

[21] Organisation for the Prohibition of Chemical Weapons, OPCW, http://www.opcw.org/

[22] F. Sevini, C. Charatsis, X. Arnes Novau, E. Stringa, J. Barrero, Axx.S. Lequarre, P. Colpo, D. Gilliland, W. Janssens, Emerging Dual-use Technologies and Global Supply Chain Compliance, IAEA Safeguards Symposium 2018